Induction Machine Modeling and Emulation for Asymmetrical Conditions

Yupeng Liu

A Thesis

In the Department

of

Electrical and Computer Engineering

Presented in Partial Fulfilment of the Requirements

For the Degree of

Doctor of Philosophy (Electrical and Computer Engineering) at

Concordia University

Montreal, Quebec, Canada

July 2022

CONCORDIA UNIVERSITY

SCHOOL OF GRADUATE STUDIES

This is to certify that the thesis prepared

By: Yupeng Liu

Entitled: Induction Machine Emulation for Asymmetrical Conditions

and submitted in partial fulfillment of the requirements for the degree of

Doctor of Philosophy (Electrical and Computer Engineering)

complies with the regulations of the University and meets the accepted standards with respect to originality and quality.

Signed by the final examining committee:

_____ Chair
Dr. Yong Zeng

_____ External Examiner
Dr. Geza Joos

_____ External to program
Dr. Jun Yan

_____ Examiner
Dr. Chunyan Lai

_____ Examiner
Dr. Luiz. A.C. Lopes

_____ Thesis Supervisor
Dr. Pragasen Pillay

Approved by: _____

Dr. Wei-Ping Zhu, Graduate Program Director

July 13th, 2022

_____

Dr. Mourad Debbabi, Dean,
Gina Cody School of Engineering and Computer Science

ABSTRACT

Induction Machine Emulation for Asymmetrical Conditions

Yupeng Liu, Ph.D.

Concordia University, 2022

The induction machine can be used as generator or motor, to convert mechanical power to electrical power or via versa. The induction generator is an essential element of many renewable energy systems such as wind power plants, etc. The induction motor is commonly adopted in industry. The advantages of induction machines are well-known compared to other types of machines. Thus, it is important to investigate induction machines with accurate models and replace expensive test benches and equipment by more efficient and economical test procedures.

To describe induction machines, different mathematical models have been devoted over the years to examine different problems. For instance, the *abc* frame model, *dq* frame model, hybrid model of *abc* and *dq*, and multiple coupled circuit (MCC) models. Based on those models, the developed model-based induction machine emulator is able to offer a flexible and easy platform for testing and analyzing characteristics of the induction machine in the laboratory environment. Therefore, accurate mathematical models are essential for further applications of induction machines.

Generally, the induction machine works under balanced conditions, but the unbalanced condition is inevitable in practice. Self-excited induction generator (SEIG) is a good option for standalone wind energy conversion systems and other renewable energy sources. In such SEIG systems, the majority of unbalanced cases occur due to load disconnection. On the other hand, the generator will have to supply nonlinear loads in most scenarios. Thus, the SEIG supplying three-phase unbalanced loads and nonlinear loads is relatively common.

Inside the induction machine, due to the combination of working environment, installation, and manufacturing factors, unbalance caused by internal faults can occur. Stator windings, rotor bars, and end rings are the most common internal faults. Such faults not only reduce the machine

working efficiency and cause excessive heating but also cause potential hazards for continuous work and safety. As a result, it can lead to the failure of the machine.

Continuing to drive the induction machine with asymmetrical conditions can cause consequent failures and even permanent damage to the machine. This thesis proposes a power electronic converter-based machine emulator replacing the actual machine to investigate the performance of the machine under different kinds of asymmetrical conditions. The machine emulator provides a laboratory environment to test and analyze the characteristics of the actual machine, especially under critical operating conditions. Therefore, the risk, time and cost associated with generating real faults can be reduced, helping to overcome safety issues with actual faulted machines. Such techniques can also be applied in fault detection, diagnosis, and fault control areas. In this thesis, the emulation of a SEIG supplying unbalanced and nonlinear loads, an induction motor with stator winding faults and rotor cage faults conditions are researched.

The mathematical model of the SEIG system is established and the emulation results of balanced loads, unbalanced loads, transients during loading and nonlinear load conditions are compared with an actual SEIG system. The mathematical model of an induction machine with stator winding faults is also built. The emulator setup for a faulted induction motor is proposed and established, the experimental results of an actual machine with 5% and 10% faults have been done and then compared with simulation and emulation results. Different loading conditions are investigated. For the rotor cage fault induction motor, a novel machine parameter measurement method is introduced, which is able to measure the machine parameters without opening the machine, making it easier and more convenient to acquire rotor parameters. Usually, the faults inside the machine are hard to distinguish. In this thesis, the rotor cage fault is identified by analyzing the stator current frequency components, then the emulation setup is established. The simulation and emulation are compared with an actual faulted induction motor including loading conditions, which demonstrates the validity of the machine emulator.

ACKNOWLEDGEMENT

Throughout the writing of this dissertation, I have received a great deal of support and assistance.

I would first like to gratefully acknowledge my supervisor ***Dr. Pragasen Pillay*** for his kind support, and professional guidance throughout my study. He offered me the opportunity to pursue the Ph.D. and taught me the attitude toward the world and the universe. I would like to show my gratitude to him that being my mentor and leading me to the path of Yoga, which will benefit me for the rest of my life. The physical and mental release after Yoga supported me to continue the research.

I would also like to thank my committee members, ***Professor Luiz A.C. Lopes, Professor Chunyan Lai, Professor Jun Yan and Professor Geza Joos*** for being as committee members for their valuable time, comments and suggestions.

My sincere thanks also go to ***Professor Paul Barendse*** from the University of Cape Town, South Africa, and his students ***Lebohang Ralikalakala and Chigozie Boniface*** for the faulted machine parameters and experimental measurement they have provided.

I would also like to thank ***Dr. Mohammad Masadeh and Dr. Mathews Boby*** for their help and valuable experience, which benefit me a lot in finishing this thesis. I would also thank my fellow lab mates in the group: ***Sumeet Singh, Mohanraj Muthusamy, Tamanwè Payarou, Bigyan Basnet, Manisha Verma, Dwaipayan Barman, Nazanin Afrasiabi, Dr. Akrem Mohamed Aljehaimi Seyedeh, Dr.Rajendra Thike and Dr. Amitkumar Kortagere Sashidhar*** for the help in the technical and experimental area. I would also like to thank all the other members of the PEER group.

In addition, I would like to thank my family, my mother and sister for their mental and financial support that let me able to focus on the my study, also for the support that always is there for me during the hard time.

Last but not the least, I would like to thank everyone who appeared in my life.

This research work was done as part of NSERC/Hydro Quebec Senior Industrial Research Chair entitled "Design and Performance of Special Electrical Machines" held by Professor Pragasen Pillay at Concordia University from 2009 to 2020. It was also done as part of the InnovÉÉ/NSERC CRD project entitled "Emulation and Design of Electric and Hybrid Electric Vehicle Motor Drive Systems". The industrial partners for this project included OPAL-RT Technologies, Hydro-Quebec and Mentor Infolytica, a Siemens Business. The authors also acknowledge the support of the Natural Sciences & Engineering Research Council of Canada through the Discovery Grants program.

Table of Contents

List of Figures

List of Tables

List of Abbreviations

Symbol	Description
DC	Direct Current
AC	Alternation Current
SEIG	Self excited induction generator
IM	Induction machine
PHIL	Power Hardware-in-the-Loop
d-axis	Direct-Axis
q-axis	Quadrature-Axis
IEEE	Institute of Electrical and Electronics Engineers
EMF	Electromotive force
FEM	Finite element model
PWM	Pulse Width Modulation
PI-Controller	Proportional-integral Controller
PR-Controller	Proportional-Resonant Controller
LC Filter	Induction-capacitive filter
THD	Total harmonic distortion
MCC	Multiple-coupled circuit
AFEC	Active front-end converter
FFT	Fast Fourier transform

List of Symbols

Symbol	Unit	Definition
A	m^2	Area of the flux path
C	F	Excitation capacitance
C_f	F	Shunt capacitor filter
i_{as}	A	Stator current in phase A
i_{bs}	A	Stator current in phase B
i_{cs}	A	Stator current in phase C
i_{ar}	A	Rotor current in phase A
i_{br}	A	Rotor current in phase B
i_{cr}	A	Rotor current in phase C
i_{ds}	A	d-axis stator current
i_{qs}	A	q-axis stator current
i_{dr}	A	d-axis rotor current
i_{qr}	A	q-axis rotor current
i_{dl}	A	d-axis load current
i_{ql}	A	q-axis load current
i_{abc}	A	Three-phase current on the load
i_f	A	Current in fault circuit
i_{i_abc}	A	Inverter output current
i_{o_abc}	A	Inverter load current

i_{abc_L}	A	Three-phase current on the inductors
I_n	A	Stator phase current
I_m	A	Per-phase magnetizing current
I_{BR}	A	Stator current under blocked-rotor condition
J	$Kg.m^2$	Inertia of motor
K_{Ii}	-	Integral controller gain for current control scheme
K_{pi}	-	Proportional controller gain current control scheme
K_{Iv}	-	Integral controller gain for voltage control scheme
K_{pv}	-	Proportional controller gain voltage control scheme
L_{ls}	H	Stator leakage inductance
L_{lr}	H	Rotor leakage inductance
L_s	H	Stator inductance
L_r	H	Rotor inductance
L_m	H	Magnetizing (main) inductance
L_f	H	Inductance of the coupling filter
m_d	-	d-axis modulation index
m_q	-	q-axis modulation index
N	-	Number of turns in each phase stator winding
N_1	-	Number of turns in un-shorted turns
N_1	-	Number of turns in shorted turns
P	-	Number of poles in the machine
P_{BR}	W	Total power under blocked-rotor condition

p	-	Derivative operator
R_s	Ω	Stator resistance
R_r	Ω	Rotor resistance
R_f	Ω	Inductor inner resistance
R_m	-	Reluctance of the mutual path
T_e	N.m	Electromagnetic torque
T_L	N.m	Load torque
v_{abc}	V	Three-phase voltage
v_{as}	V	Stator voltage in phase A
v_{as1}	V	Stator voltage in phase A on un-shorted turns
v_{as2}	V	Stator voltage in phase A on shorted turns
v_{bs}	V	Stator voltage in phase B
v_{cs}	V	Stator voltage in phase C
v_{ar}	V	Rotor voltage in phase A
v_{br}	V	Rotor voltage in phase B
v_{cr}	V	Rotor voltage in phase C
v_{ds}	V	d-axis stator voltage
v_{qs}	V	q-axis stator voltage
v_{dr}	V	d-axis rotor voltage
v_{qr}	V	q-axis rotor voltage
v_{oabc}	V	Inverter output voltage
V_n	V	Stator Phase voltage

X_{ls}	Ω	Stator leakage reactance
X_{lr}	Ω	Rotor leakage reactance
X_m	Ω	Magnetizing reactance
λ	Wn-turn	Flux linkage
λ_{ds}	Wn-turn	d-axis stator flux linkage
λ_{qs}	Wn-turn	q-axis stator flux linkage
λ_{dr}	Wn-turn	d-axis rotor flux linkage
λ_{qr}	Wn-turn	q-axis rotor flux linkage
θ_r	Rad	Angle between stator phase A and rotor phase A
β	-	Fraction of shorted turns
μ_i	H.m	Magnetic permeability of the iron
ω	Rad/s	Electrical-angular speed
ω_s	Rad/s	Electrical-stator angular speed
ω_r	Rad/s	Electrical-rotor angular speed
ω_m	Rad/s	Mechanical angular speed
*	-	Superscript indicates reference signal

Chapter 1.
Introduction

With the development of renewable energy power generation, the three-phase induction machine is widely adopted as the energy converter between mechanical power and electric power. The advantages of the induction machine over synchronous machine are brushless construction with squirrel-cage rotor, smaller size, lower maintenance cost, no DC supply for excitation and better transient performance [1]. The squirrel-cage induction machine working as a self-excited induction generator (SEIG) is widely employed in standalone systems, especially in hydroelectric, tidal, wind power plants and other renewable energy sources, where most of them are located in remote areas or developing countries [2]. Research work have been carried out on SEIG systems, in terms of the algorithm and control of SEIG system supply unbalanced loads, different kinds of induction machine working under asymmetry conditions [3]-[7]. Asymmetry caused by internal faults frequently occurs on rotor bars, end rings and windings. The research work carried out internal to induction machines includes precisely modeling the asymmetry machine model, steady-state analysis of performance under asymmetry conditions and research on different kinds of asymmetry conditions.

This Chapter presents a literature review of the induction machine under asymmetrical operating conditions, a consequence of which can lead to machine failure, Power hardware-in-the-loop emulation is proposed to emulate actual machines at full power. This Chapter presents an overview of the machine emulation method including the three main parts of machine emulation: 1) Proper machine model, 2) Power electronic device, and 3) Control strategy.

1.1 Induction Machine Under Asymmetrical Conditions

The balanced and unbalanced conditions of SEIG system have been discussed [8]-[11]. Generally, the SEIG system will work at balanced condition, but the unbalanced condition is inevitable in practice. In the induction motors, most unbalanced or asymmetrical conditions occur with stator windings, rotor bars, and end rings. In induction generators, the majority of unbalanced cases occur at load disconnection. Therefore, contributions have been devoted to the induction machine performance under unbalanced conditions. A multi-objective genetic algorithm was proposed to investigate steady-state performance characteristics of SEIG supplying an unbalanced load [8]. A control method for the induction generator under unbalanced loads has been proposed and validated by simulation and experiment results in [9]. A winding function method based induction machine balanced and unbalanced model has been investigated on balanced and unbalanced supply conditions in [10]. The performance of a wind turbine driven SEIG system is studied under unbalanced loads in [11].

When an internal fault occur, the induction machine can operate under asymmetrical conditions, such as:

1) inner turn fault of stator phase winding,
2) abnormal connection of the stator winding,
3) broken rotor bar or end ring.

The results of asymmetrical operation of induction machines will be

1) unbalanced air gap voltages,
2) consequently unbalanced line currents,
3) increased losses,
4) increased torque pulsations,
5) decreased average torque.

Such asymmetrical operation of the induction motor will cause poor efficiency and excessive heating, and lead to failure of the machine. Therefore, accurate prediction of the induction machine under such conditions is important. The internal faults of induction machine have been discussed in [12-14]. A multiple coupled circuit model is presented in [12] for simulation of induction machines under variety of fault conditions, such as broken rotor bars and

end rings. A transient model for an induction machine with stator winding turn faults researched in [13] by using reference frame transformation theory, experimental results are provided to validate the model. An induction machine model based on the coupled circuit approach is presented in [14] to simulate both the rotor and stator faults, the simulation results are presented.

1.2 Machine Emulation

An electrical machine emulator is a good option to replace expensive test benches and equipment as well as the risks associated with development and testing of new drive systems. With the emulator, various types of electric machines with different power ratings or the conventional and advanced control strategies can be tested. The implementation of the emulator utilizes the concept of power hardware-in-the-loop, wherein power converters are controlled to emulate machine characteristics [15]. As shown in Fig. 1-1 (b) a power electronic converter has the same three-phase output as an actual induction machine as shown in Fig. 1-2 (a), if the power converter controlled output in the same or similar to an induction machine from a power of view of the grid the controlled power converter behaves as an induction machine. The emulator is typically a bidirectional power electronic interface, which is capable of running either as an energy sink drawing electrical power from the grid or as an energy source feeding energy into the grid [16-18]. The induction machine emulator offers a flexible and easy platform for testing and analyzing the characteristics of the emulated machine at particular operating conditions in the laboratory environment. With proper controller design, converters can behave in a similar manner to the actual machine. An induction machine emulation test platform was implemented in [11]. A three-phase induction motor emulator based on a power converter in rectifier mode was introduced in [19]. The benefit of a machine emulator system compared to conventional electrical machine testing has been investigated in [20-27] and listed below:

- The machine emulation allows the testing of a drive inverter and novel control strategies before the actual machine is prototyped, which can take several months, thus significantly reducing the time to market an electrical machine dive.
- Compare to the FEA simulation (Ansys, JMAG, Motorslove), real-time emulation saves a lot of simulation time, also the test is using actual powers and currents, which is closer to the actual condition.

- With a machine emulator, there is no requirement for a dynamometer test bench to load the machine. The loading of the machine can be achieved by using the machine emulator system. Thus during loading conditions, the drive inverter will supply power to the emulator, which replicates the actual machine coupled for a load on a dyno bench. In such conditions, the experiment environmental is safer due to there being no rotating parts during testing.
- With a machine emulator, the testing of the drive inverter and controller can be done for severe operating conditions, such as overloads and faulted machines. If the machine is faulted and still driven as usual, the damage to the machine will be a consequence which can lead to machine failure and cause safety issues. With the machine emulator, the control method for a faulted machine can be tested, to prevent damage to the real machine.

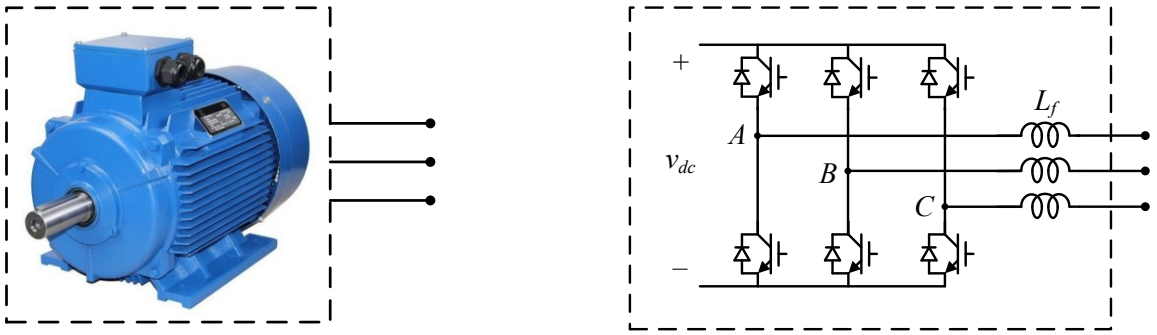

(a) (b)

Fig. 1-1 The emualtion concept (a)Actual machine (b) Emulation machine

There are three major parts in the emulation system, which ensures the emulation has quick response and accurate tracking, including: I) a proper machine mathematical machine model, II) a power electronic device, III) the control strategy in the emulation system.

1.2.1 Machine Model in Emulation System

The emulator is used to emulate an actual machine, such that an accurate mathematical model is mandatory, which is able to represent the actual machine. Also, the emulation is working in real-time, which requires calculating the reference value and controlling the power device output as a real machine. Significant computation is required in such conditions, thus the machine model needs to be simple enough for speed responses. A lot of work has been done in applying a

simplified machine model to achieve real-time and accurate emulation [20-23]. However, such simplified machine model are only verified in steady-state emulation, the machine emulation performance under various machine transients, such as loading, faults, and saturation conditions need to be investigated. The research work in [24][25] used FEM in the machine emulation, the FEM model can be more accurate compared to an analytical mathematical model, due to consideration of more complex elements in the machine, such as flux path in the machine. However, such machine models increase the calculation requirements, especially during fault conditions.

Thus, a proper mathematical machine model is a key component to investigate such unbalanced or asymmetrical conditions. A multiple-coupled circuit (MCC) model was first proposed in [28], to model stator and rotor faults including; stator open and short circuits, cracks in rotor bar and end ring. The topology of the MCC model is shown in Fig.1-1, which illustrates each part of the machine. The application of the MCC model in the broken rotor bar is investigated in [29-33], and faulted machine in [34-36]. It is shown that the MCC is able to simulate the machine with very accurate results. The details of the machine are hard to measure, and the resistance of each rotor bar is very small, which can induce large measurement errors. The measurement of inductance is done by using the winding function method, which accounts for the space harmonics in the machine, neglects saturation effect and eddy currents, and assumes symmetry of the machine. The high calculation requirement is also hard to apply in real-time.

The d-q frame model is one of the most common ways to analyze the induction machine. It has been demonstrated in the early research stage [37], [38], where the three-phase system was converted to a two-phase system. The rotating speed of d and q axis has three reference frames: 1) the stationary reference frame, in which the d and q axis are fixed without rotating; 2) the synchronously reference frame, where the d and q axis rotate at synchronous speed; 3) the rotor reference frame, where the d and q axis rotate at rotor speed. When an induction machine works in the generation mode the stator frequency is unknown, so the rotor reference frame is the only option in that case. Further research demonstrated that in a 3-wire system, zero sequence quantities are nonexistent in d-q systems even under different types of unbalanced conditions [39]. Therefore, the zero sequence quantities are excluded from the induction machine equivalent circuit under such conditions.

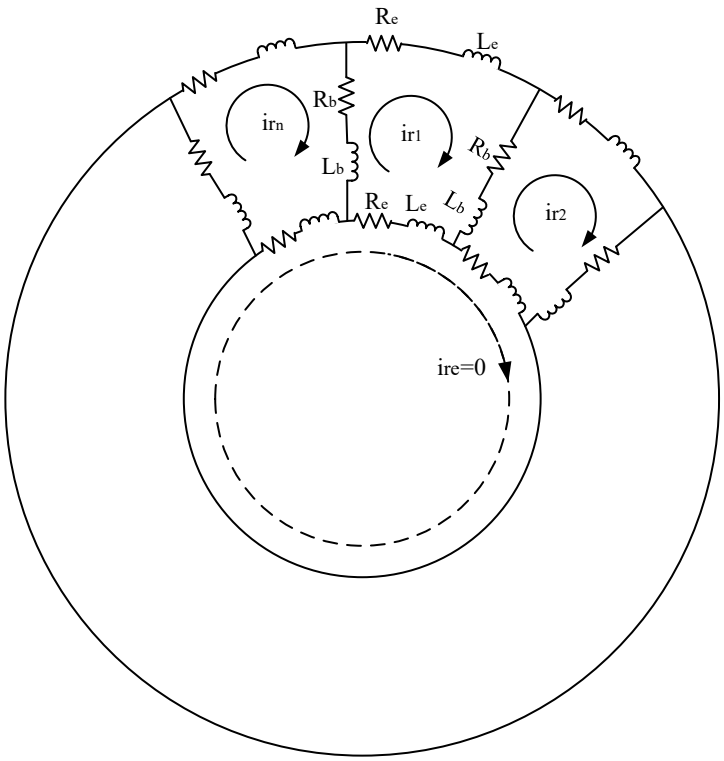

Fig. 1-2 Multiple coupled circuit topology

1.2.2 Power Electronic Converter for Emulation

The power electronic converter in the emulation system is able to generate the desired power, which is the same as an actual machine. It could be either a power electronic converter or a linear amplifier or a combination. Research work has been conducted on emulation by a linear amplifier in [38], [39], the linear amplifier is controlled to mimic an actual machine and grid faults conditions are studied. The research work in [32-37], [41] uses a power electronic converter to emulate an actual machine. The power electronic device in the emulation system is able to generate or draw the same power as an actual machine.

1.2.3 Control Strategy in Emulation System

The control methodology applied in machine emulation is important, affects the accuracy of the emulation and also the transient performance. The most common way is to control the power electronic converter in the current control mode to mimic machine currents. However, if the drive inverter is also working in the current control mode, it will cause a control conflict [34], [35]. The control method in [39] applies a PI controller in the *dq* reference frame. The results are accurate

and fast-tracking, however, the control method may not work under fault conditions due to the unbalance. Three-phase PI controllers have been used in [40], which controls the *abc* three phases separately, it will be an advantage while emulating faulty conditions, however, the steady-state error due to the PI controller needs to be considered.

1.3 Motivation

The motivation of this work is to investigate accurate emulation of electrical machine under different asymmetrical conditions.

In the case of isolated systems, the induction generator, and more precisely the three-phase squirrel induction generator is widely adopted, in remote and isolated areas. Due to the reasons of the structure has high stability, needs little maintenance, and is cost-efficient. Therefore, the study of SEIGs has been the subject of many research works. Generally, the SEIG system will work at the balanced condition, but the unbalanced condition is inevitable in practice. Majority of unbalanced cases occur at loads disconnection. Therefore, it is important to investigate the SEIG under unbalanced condition.

When looking in inside the induction machines, due to the combined factors of thermal, environmental stress, installation, and manufacturing, asymmetry caused by internal faults occur frequently. Broken rotor bars and winding faults are the most common asymmetrical conditions. These kinds of faults not only reduce the machine working efficiency and cause potential hazards for continuous work, but also cause serious secondary effects. The broken part of the bar has high chance of hitting stator windings at high velocity. The majority of stator winding faults are caused by the short circuit of a few turns of a stator winding and are difficult to locate within the winding.

Since many of the induction motors are supplied by inverters to achieve adjustable speed drives systems, thus continuing to drive faulted machines can lead to machine failure and even the damage of entire system. This thesis proposes a power electronic converter-based machine emulator replacing the actual machine to investigate the performance of the machine under kinds of asymmetrical conditions. The built machine emulator provides a laboratory environment to test and analyze the characteristics of the actual machine, especially under critical operating conditions. Therefore, the risk, time and cost associated with generating real faults can be reduced, helping to overcome safety issues with actual faulted machines. Such techniques could also be applied in

fault detection, diagnosis, and fault control areas. Thus, for the drive inverter, it is able to accurately predict the transient performance of the machine. It will also be useful for investigating the operational characteristics of faulty motors without destructive testing.

1.4 Objectives

The main objective of this work is to design and develop a three-phase bidirectional power electronic converter emulator to be applied in the emulation of several asymmetrical operating conditions of induction machine. The specific objectives of the research include:

1. Building the mathematical model of the electrical machine under healthy conditions, which will be the foundation of further research on electrical machine emulation and a variety of asymmetrical operating conditions.
2. Building the three-phase bidirectional power electronic converter emulator for electrical machines, through which various electric machines with different power ratings or the conventional and advanced control strategies can be tested.
3. Building the mathematical model of an induction machine under certain kinds of internal faults. Asymmetrical operation conditions in induction motors are usually caused by internal faults. The internal faults have serious consequences, which may break down the machines and even damage the entire system. Therefore, a proper model will help to study the machine performance under unbalanced conditions. The machine model is also a key component for accurate emulation, due to the fact that emulation is working in real-time, which requires calculating the reference value and controlling the power electronic system as a real machine. Significant computation is required in such conditions, thus the machine model needs to be simple enough to achieve fast responses.
4. In induction generator systems, nonlinear loads and loads disconnection occur frequently, such unbalanced conditions are inevitable in practice. In an induction motor, the extreme working environment due to the overload or overheating will cause inner faults such as stator winding faults, and broken rotor bars.

1.5 Contributions

The contributions of this Ph.D. research work are summarized below.

- Development of a power hardware-in-the-loop based machine emulator system.

- Development of a SEIG emulator with unbalanced operating conditions.

- Development of emulator of an induction machine with stator winding fault.

- Development an induction machine emulator with rotor cage fault.

- Investigation of machine emulator control strategies.

Journal papers:

- **Yupeng Liu**, M. A. Masadeh and Pragasen Pillay, "Power Hardware-in-the-Loop Based Emulation of a Self-Excited Induction Generator Under Unbalanced Conditions," in *IEEE Transactions on Industry Applications*, doi: 10.1109/TIA.2021.3118985.

- **Yupeng Liu**, Lebohang Ralikalakala, Paul Barendse and Pragasen Pillay, "Power Electronic Converter-Based Induction Motor Emulator with Stator Winding Faults", *IEEE Transactions on Industry Electronics* (under review).

Conference papers:

- **Yupeng Liu**, Chigozie Boniface, Paul Barendse and Pragasen Pillay, "Power Electronic Converter-Based Induction Motor Emulator with Rotor Cage Faults", *2022 IEEE Energy Conversion Congress and Exposition (ECCE).*

- **Yupeng Liu** and Pragasen Pillay, "Emulation of A Self-Excited Induction Generator Feeding Nonlinear Loads," *IECON 2021 – 47th Annual Conference of the IEEE Industrial Electronics Society*, Toronto, ON, Canada, 2021, pp. 1-6.

- **Yupeng Liu**, Lebohang Ralikalakala, Paul Barendse and Pragasen Pillay, "Power Hardware-in-the-Loop based Emulation of An Induction *Machine* with Stator Winding Faults," *IECON 2021 – 47th Annual Conference of the IEEE Industrial Electronics Society*, Toronto, ON, Canada, 2021, pp. 1-6.

- **Yupeng Liu**, Mohammad Masadeh and Pragasen Pillay, "Emulation of an Isolated Induction Generator Under Unbalanced Conditions," *2020 IEEE Energy Conversion Congress and Exposition (ECCE)*, Detroit, MI, USA, 2020, pp. 1794-1799.

1.6 Organization of This Thesis

Chapter 2 presents the healthy induction machine mathematical model in both *abc* and *dq* reference frames, which is fundamental to investigating faulted machine model. The experimental tests to measure machine parameters is presented.

Chapter 3 presents a power electronic converter-based SEIG emulator system. The objective is to investigate the performance of the SEIG emulator with different types of loads. The unbalanced loads are firstly implemented in this chapter, then the transient performance and nonlinear loads are investigated. Experimental results are presented for the emulation of the SEIG system.

Chapter 4 presents the emulation of stator winding faults of induction machines. The mathematical model of the stator winding fault is firstly established for the induction machine in both *abc* and *dq* reference frames. The experimental setup for emulation is established and the emulator control structure is introduced and designed. Experimental results are presented for the emulation of stator winding faults and compared with actual faulted induction machine results.

Chapter 5 presents the emulation of the rotor cage fault induction machine. The rotor cage fault condition is firstly identified by FFT analysis. Then the method to measure the faulted machine parameters is introduced. Experimental results are presented for the emulation of the rotor cage fault induction machine and compared with an actual faulted induction machine results.

Chapter 6 presents the conclusion of this thesis and possible future work.

Chapter 2.
Mathematical Models of Induction Machines

The induction machine is a high-order, nonlinear, strongly coupled multivariable system. The stator and rotor system are connected through the flux generated by each system, also known as mutual inductance. In order to investigate the performance of the induction machine under various conditions, it is important to find a simple and convenient mathematical model, which is also accurate enough to account for anomalous conditions. Here, the *abc* and *dq* models of a healthy induction machine are firstly presented. Then, the parameter measurements method of induction machine is introduced to measure the stator resistance, rotor resistance, stator leakage reactance and rotor leakage reactance. This Chapter will be the fundamentals for the further research of asymmetrical conditions.

2.1 Induction Machine Model in the abc Reference Frame

The mathematical model of a healthy IM's stator voltages in *abc* reference frame can be presented in terms of first-order differential equations as [41]

$$v_{as} = R_s i_{as} + p\lambda_{as} \tag{2-1}$$

$$v_{bs} = R_s i_{bs} + p\lambda_{bs} \tag{2-2}$$

$$v_{cs} = R_s i_{cs} + p\lambda_{cs} \tag{2-3}$$

And that of the rotor voltages are

$$v_{ar} = R_r i_{ar} + p\lambda_{ar} \tag{2-4}$$

$$v_{br} = R_r i_{br} + p\lambda_{br} \tag{2-5}$$

$$v_{cr} = R_r i_{cr} + p\lambda_{cr} \tag{2-6}$$

For $\lambda_s^{abc}$and λ_r^{abc}there are equations as

$$\lambda_s^{abc} = \boldsymbol{L}_{ss}^{abc}\boldsymbol{i}_s^{abc} + \boldsymbol{L}_{sr}^{abc}\boldsymbol{i}_r^{abc} \tag{2-7}$$

$$\lambda_r^{abc} = \boldsymbol{L}_{rr}^{abc}\boldsymbol{i}_r^{abc} + \boldsymbol{L}_{rs}^{abc}\boldsymbol{i}_s^{abc} \tag{2-8}$$

Which are expended as

$$\begin{bmatrix}\lambda_{as}\\ \lambda_{bs}\\ \lambda_{cs}\end{bmatrix} = \begin{bmatrix} L_{ls}+L_{ms} & -\frac{1}{2}L_{ms} & -\frac{1}{2}L_{ms} \\ -\frac{1}{2}L_{ms} & L_{ls}+L_{ms} & -\frac{1}{2}L_{ms} \\ -\frac{1}{2}L_{ms} & -\frac{1}{2}L_{ms} & L_{ls}+L_{ms}\end{bmatrix}\begin{bmatrix}i_{as}\\ i_{bs}\\ i_{cs}\end{bmatrix} + L_{sr}\begin{bmatrix} cos\theta_r & cos(\theta_r+\Upsilon) & cos(\theta_r-\Upsilon) \\ cos(\theta_r-\Upsilon) & cos\theta_r & cos(\theta_r+\Upsilon) \\ cos(\theta_r+\Upsilon) & cos(\theta_r-\Upsilon) & cos\theta_r\end{bmatrix}\begin{bmatrix}i_{ar}\\ i_{br}\\ i_{cr}\end{bmatrix} \tag{2-9}$$

$$\begin{bmatrix}\lambda_{ar}\\ \lambda_{br}\\ \lambda_{cr}\end{bmatrix} = \begin{bmatrix} L_{lr}+L_{mr} & -\frac{1}{2}L_{mr} & -\frac{1}{2}L_{mr} \\ -\frac{1}{2}L_{mr} & L_{lr}+L_{mr} & -\frac{1}{2}L_{mr} \\ -\frac{1}{2}L_{mr} & -\frac{1}{2}L_{mr} & L_{lr}+L_{mr}\end{bmatrix}\begin{bmatrix}i_{ar}\\ i_{br}\\ i_{cr}\end{bmatrix} + L_{rs}\begin{bmatrix} cos\theta_r & cos(\theta_r-\Upsilon) & cos(\theta_r+\Upsilon) \\ cos(\theta_r+\Upsilon) & cos\theta_r & cos(\theta_r-\Upsilon) \\ cos(\theta_r-\Upsilon) & cos(\theta_r+\Upsilon) & cos\theta_r\end{bmatrix}\begin{bmatrix}i_{as}\\ i_{bs}\\ i_{cs}\end{bmatrix} \tag{2-10}$$

where, $v_{as},\ v_{bs}, v_{cs}$ are the stator voltage, $i_{as},\ i_{bs}, i_{cs}$ are the stator current, R_s and R_r are the stator and rotor resistances, $v_{ar},\ v_{br}, v_{cr}$ and $i_{ar},\ i_{br}, i_{cr}$ are the rotor voltage and current on each phase, λ represent the flux linkage, p is the derivative operator $\frac{d}{dt}$, $\boldsymbol{L}_{ss}^{abc}$and $\boldsymbol{L}_{rr}^{abc}$are symmetrical matrices of the self-inductance of the stator and rotor windings, L_{sr} and L_{rs} are stator to rotor or rotor to stator mutual inductances, L_{ls} and L_{lr} are the leakage inductances of the stator and rotor, respectively, and L_m is the magnetizing inductance. θ_r is the angle between stator phase A and rotor phase A, and Υ=120°.

2.2 Induction Machine Model in dq Reference Frame

The machine model in *abc* reference frame can be transferred to the *dq* frame model, which is one of the most common methods to analyze induction machines. By apply the Park's transformation equation on the *abc* reference frame model, the *dq* model of an induction machine can be derived.

$$v_{ds} = R_s i_{ds} + p\lambda_{ds} + \lambda_{qs}\omega \tag{2-11}$$

$$v_{qs} = R_s i_{qs} + p\lambda_{qs} - \lambda_{ds}\omega \tag{2-12}$$

$$v_{dr} = R_r i_{dr} + p\lambda_{dr} + \lambda_{qr}(\omega - \omega_r) \tag{2-13}$$

$$v_{qr} = R_r i_{qr} + p\lambda_{qr} - \lambda_{dr}(\omega - \omega_r) \tag{2-14}$$

where v_{ds} and v_{qs} are the stator voltages in *dq* reference frame, v_{dr} and v_{qr} are the rotor voltages in *dq* frame, i_{ds} and i_{qs} are the stator currents in *dq* frame, i_{dr} and i_{qr} are the rotor currents in *dq* frame, λ_{ds} and λ_{qs} are the stator flux linkages in *dq* frame, λ_{dr} and λ_{qr} are the rotor flux linkages in *dq* frame.

Here the ω is chosen as synchronous reference frame in motor mode, which have $\omega = \omega_s$. In addition, in the case of generation mode of induction machine, the stator and rotor frequencies are unknown, so that the machine model has to be chosen in the rotor reference frame [41], which will have $\omega = \omega_r$.

The flux linkage has

$$\lambda_{ds} = L_s i_{ds} + L_m i_{dr} \tag{2-15}$$

$$\lambda_{qs} = L_s i_{qs} + L_m i_{qr} \tag{2-16}$$

$$\lambda_{dr} = L_r i_{dr} + L_m i_{ds} \tag{2-17}$$

$$\lambda_{qr} = L_r i_{qr} + L_m i_{qs} \tag{2-18}$$

where

$$L_s = L_{ls} + L_m \tag{2-19}$$

$$L_r = L_{lr} + L_m \tag{2-20}$$

The generator torque is related with rotor speed as

$$T_e = \mathrm{J}\left(\frac{2}{P}\right) p\omega_r + \mathrm{B}\omega_r + T_L \tag{2-21}$$

where T_e is electromagnetic torque, J is inertia of motor, P is number of poles in the machine, ω_r is rotor speed, B is the friction coefficient, T_L is load torque, p is the differential operator.

2.3 Machine Parameter Measurements

For the induction machine emulation system, various parameters of the machine such as rotor and stator resistance, rotor, and stator leakage reactance as well as magnetizing reactance has to be measured and calculated. To obtain these parameters a DC test, no-load and block-rotor tests are performed.

The magnetic field of the stator is fixed in space by supplying a steady-state direct current to the stator windings during DC test. Therefore, no voltage in the rotor is generated. The resistance of the stator winding is calculated for a Δ-connected machine as shown below

$$R_s = \frac{3}{2}\frac{V_{dc}}{I_{dc}} \tag{2-22}$$

To obtain the rotor resistance, rotor and stator leakage reactance and magnetizing reactance, no-load and blocked-rotor tests are performed. Its equivalent circuits are shown in Fig. 2-1 (a) and (b), respectively.

During the no-load test, the rated voltage is applied and the machine is rotating at its base speed. Therefore, the slip of the machine is close to 0 and the rotor side is considered as an open circuit. The equivalent circuit during no-load test is as shown in Fig. 2-1 (a) where V_n is the phase voltage of the stator, I_n is the stator phase current, I_m is the per-phase magnetizing current. The equivalent circuit is reactive as the power factor of machine is low. Under this circumstance the relationship of stator leakage reactance X_{ls} and magnetizing reactance X_m with phase voltage and current can be written as

$$X_m + X_{ls} = \frac{V_n}{\sqrt{3} * I_n} \tag{2-23}$$

where V_n and I_n are the phase voltages and currents, respectively.

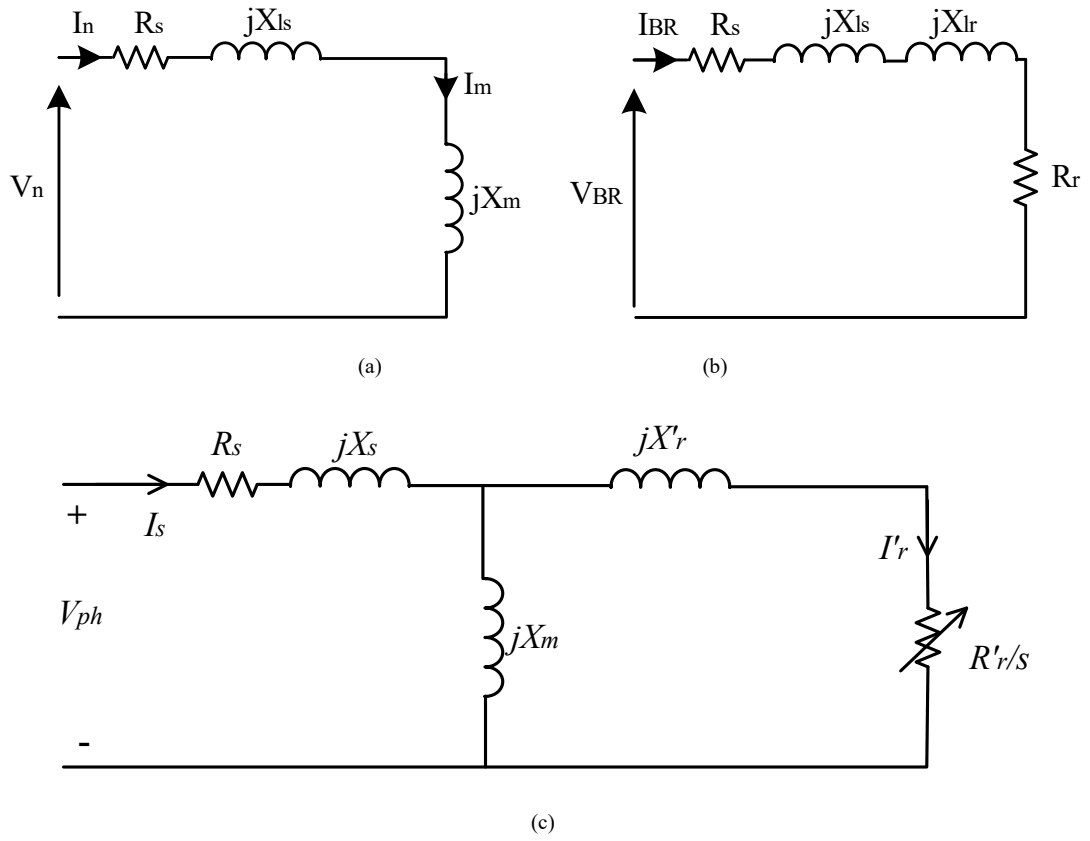

Fig. 2-1 Equivalent circuit of induction machine:

(a) No-load test (b) blocked rotor test (c) equivalent circuit.

The equivalent circuit of the block-rotor test is shown in Fig. 2-1 (b), where the rotor resistance R_r can be obtained by

$$R_r = \frac{P_{BR}}{3I_{BR}^2} - R_s \tag{2-24}$$

where $P_{BR}$is the total power and I_{BR} is the rated stator current under blocked-rotor condition. They are measured using a YOKOGAWA power meter. R_s is calculated from (2-22).

From Fig. 2-1 (b), the equation to calculate the total leakage reactance $X_{ls} + X_{lr}$ can be written as:

$$X_{ls} + X_{lr} = \sqrt{Z_{BR}^2 - R_{BR}^2} = \sqrt{(\frac{V_{BR}}{\sqrt{3}I_{BR}})^2 - (\frac{P_{BR}}{3I_{BR}^2})^2} \tag{2-25}$$

As discussed earlier the total leakage reactance is divided into stator leakage reactance X_{ls} and rotor leakage reactance X_{lr}, which are utilized to define A, B, C, D four types of machines

according to IEEE Std 112™ [42]. The machine used in this paper is design C type machine, so it has the constant split ratio according to [42] as follows:

$$X_{ls} = 0.3(X_{ls} + X_{lr}) \tag{2-26}$$

$$X_{lr} = 0.7(X_{ls} + X_{lr}) \tag{2-27}$$

After X_{ls} is calculated, according to equation (2-23), the magnetizing reactance X_m can be calculated.

Based on the above steps, the induction machine parameters in steady state can be decided, which are shown in Fig. 2-1(c) is the per phase equivalent circuit.

2.3 Summary

This Chapter first established the healthy induction machine mathematical model in the *abc* reference frame and then by applying Park's transformation, the machine model is transferred to the *dq* reference frame so as to simplify the calculation during simulation. A proper mathematical machine model is a key component for further research on asymmetrical conditions so as to achieve accurate emulation results. The machine parameter measurement method is also introduced in this Chapter. By DC test the stator resistance is measured. From the blocked-rotor test and no-load test, the rotor resistance, mutual inductance, stator leakage inductance, and rotor leakage inductance are confirmed. The machine parameter measurement method will also be fundamental to investigating the parameter measurement of an induction machine with rotor cage fault.

Chapter 3.
SEIG Emulation Under Unbalanced Conditions

Extensive research work has been carried out on the characteristics and applications of the induction generator [2], [44-48]. An induction generator scheme is proposed in [2] to eliminate the low-order harmonics from the machine phase voltage throughout the full speed range. The application of a SEIG system in a wind farm is established in [44] and the transient behavior is examined. The operating principle of the SEIG is summarized as: when the mechanical prime mover is connected to a standalone induction machine, an electromotive force (EMF) will be induced in the stator windings as a result of the residual flux present in the rotor. The frequency of generated EMF is in proportion to the rotor speed. Then the capacitors, which are parallel to the stator terminals, produce a flow of reactive current in the stator windings. Hence magnetizing flux is established in the machine. The induced voltage at the stator winding terminals continue rising until reaching the point that the reactive power demanded by the SEIG is balanced with reactive power supplied by the terminal capacitors. In this way, the SEIG is capable of establishing the magnetizing flux and stator voltage, thus operating independently as a generator without a grid power supply in remote areas. Moreover, there are different types of generators that have been discussed in the literature. The research on modeling and application of self-excited reluctance generators in wind generation is carried out in [45]-[47], however, the research focuses only on the mathematical modeling of reluctance machine. The doubly fed induction generator is studied in [48] to improve the dynamic performance during voltage dips.

Contributions have been made to the balanced and unbalanced conditions of the induction generator system in [49]-[55]. A simplified induction generator model is proposed to study the effect on the subsynchronous resonance phenomenon and transient stability [49], [50]. Generally, the generator system is designed for balanced conditions, but unbalanced conditions are inevitable

in practice. The control strategy of induction wind generators under unbalanced grid voltages is presented to eliminate the current distortion and power ripple [51]. The resonant-based back stepping direct power control of an induction generator under both balanced and unbalanced grid conditions is researched for wind power generation, to handle unbalanced grid conditions [52].

Many contributions have been made on unbalance occurring with load disconnection. The unbalanced load conditions in SEIG systems can cause vibration of the machine due to unbalanced magnetic fields. Induction generators running under unbalanced conditions can reduce the machine life cycle significantly. Some severe unbalanced cases may even damage the machine. Unbalanced loads can also increase the power losses in the system. A multi-objective genetic algorithm is proposed in [53] to investigate the steady-state performance characteristics of the SEIG supplying an unbalanced load. The reactive power requirement of SEIG systems under different loading conditions is researched in [54]. A control method for the induction generator under unbalanced loads has been proposed and validated by simulation and experimental results in [21]. An induction machine using winding functions has been investigated on balanced and unbalanced supply conditions in [22]. The performance of a SEIG system driven by a wind turbine is investigated under unbalanced loads in [42]. It is difficult to test unbalanced conditions in the laboratory environment due to the bulky machines required in SEIG systems.

Generally, the SEIG system supplies linear loads. However, nonlinear loads, mainly power electronic devices, are increasingly common, due to the ever-increasing penetration of distributed generation, such as Electric Vehicles (EVs) and energy storage batteries [55]. Therefore, it is important to investigate the characteristics of SEIGs feeding nonlinear loads [56]-[64]. A STATCOM-based SEIG feeding nonlinear loads was studied in [63].

This Chapter proposes a PHIL emulation for flexible testing of SEIG systems including unbalanced load conditions and nonlinear load conditions. The SEIG model is established for the use of emulation, which considers the magnetic saturation effects, variable stator/rotor leakage split ratio and unbalanced conditions. Experiments are carried out on a real SEIG to verify the effectiveness of proposed emulation system.

Fig. 3-1 indicates the actual SEIG system diagram. The wind turbine represents the renewable energy source as a prime-mover, which provides the input power to the induction generator. The induction generator and excitation capacitors are connected in parallel with the

loads. The excitation capacitors are used to build up the voltage of the machine.

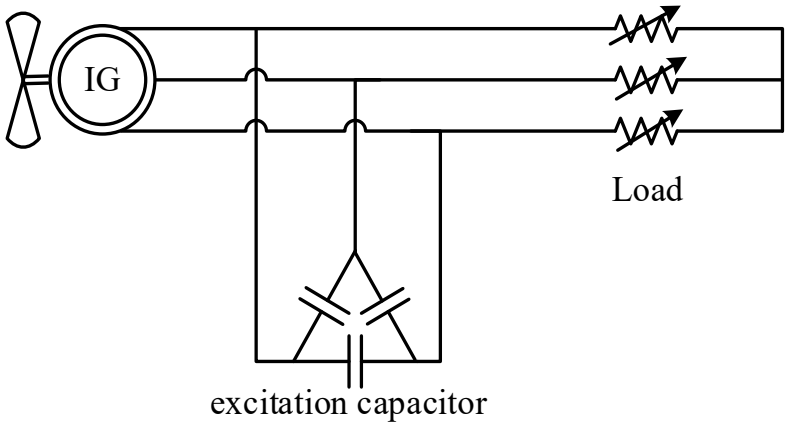

Fig.3-1 Discussed SEIG system.

3.1 Modeling of the SEIG System

3.1.1 Variable Stator/Rotor Leakage Split Ratio Calculation

According to IEEE Std 112™, the split ratio of stator/rotor leakage reactance is constant value based on different types of machines as follows [29]: $\frac{X_{1s}}{X_{1r}} = 1.0$ for Design A, Design D and wound rotor machines, $\frac{X_{1s}}{X_{1r}} = 0.67$ for Design B machines, $\frac{X_{1s}}{X_{1r}} = 0.43$ for Design C machines. However, for severe transient conditions like heavy loading conditions and direct online start-up, such an assumption will not be correct.

For a close prediction of machine's dynamic performance, the leakage reactance calculation, which is current dependent is considered in [65]. Also, the effect of saturation of the machine model is included in the calculation. The high accuracy of machine model is achieved during transients by considering a current dependent variable split ratio.

In the finite element model (FEM), the rotor space of the induction machine is considered as a non-magnetic material to acquire the accurate stator leakage reactance [65]. In this way the magnetic field of the rotor space is eliminated. Then the stator leakage reactance X_{ls} dependent on current is as given in the equation below

$$X_{ls} = k_3 e^{-c_3 I_s} - k_4 e^{-c_4 I_s} \tag{3-1}$$

In the next step, the original material of the rotor is used, and the machine is working in blocked rotor conditions. The rotor leakage reactance X_{lr} and magnetizing reactance X_m according to their respective current are calculated and expressed by

$$X_{lr} = k_5 e^{-c_3 I_r} - k_6 e^{-c_4 I_r} \tag{3-2}$$

$$X_m = k_1 e^{-c_1 I_m} - k_2 e^{-c_2 I_m} \tag{3-3}$$

where k_1, k_2, c_1, c_2 are the coefficients of magnetizing reactance saturation, k_3 to k_6, c_3, c_4 are the coefficients of initial leakage reactance saturation. The coefficients values of k&c are curve fitting parameters, which are acquired through FEM results as discussed in [65]. These values are unique and different from one machine to another.

I_m is magnetizing current, obtained in the d-q frame by

$$I_m = \sqrt{(i_{qs} + i_{qr})^2 + (i_{ds} + i_{dr})^2} \tag{3-4}$$

In equations (22) and (23), $I_s$and I_r are obtained respectively from the d-q frame components as

$$I_s = \sqrt{(i_{qs}^2 + i_{ds}^2)} \tag{3-5}$$

$$I_r = \sqrt{(i_{qr}^2 + i_{dr}^2)} \tag{3-6}$$

3.1.2 Inverter Mathematical Model

To control the inverter to behave as a SEIG, the mathematical model of the inverter is also established. The three-phase inverter output voltage is represented as v_{abc}, three-phase voltage on capacitors is represented as v_{oabc}, the three-phase current on the inductors is represented as i_{abc_L} and the three-phase current on the load side is represented as i_{abc}.

The inverter mathematical model in abc reference frame can be written as:

$$L_f \begin{bmatrix} \frac{di_{a\_L}}{dt} \\ \frac{di_{b\_L}}{dt} \\ \frac{di_{c\_L}}{dt} \end{bmatrix} = \begin{bmatrix} v_a \\ v_b \\ v_c \end{bmatrix} - \begin{bmatrix} v_{oa} \\ v_{ob} \\ v_{oc} \end{bmatrix} \tag{3-7}$$

$$C_f \begin{bmatrix} \frac{dv_{oa}}{dt} \\ \frac{dv_{ob}}{dt} \\ \frac{dv_{oc}}{dt} \end{bmatrix} = \begin{bmatrix} i_{a\_L} \\ i_{b\_L} \\ i_{c\_L} \end{bmatrix} - \begin{bmatrix} i_a \\ i_b \\ i_c \end{bmatrix} \tag{3-8}$$

By applying Park's transformation, the inverter mathematical model in dq reference frame can be written as:

$$L_f \frac{di_{dL}}{dt} - \omega L_f i_{qL} = v_d - v_{od} \tag{3-9}$$

$$L_f \frac{di_{qL}}{dt} + \omega L_f i_{dL} = v_q - v_{oq} \tag{3-10}$$

$$C_f \frac{dv_{od}}{dt} - \omega C_f v_q = i_{dL} - i_d \tag{3-11}$$

$$C_f \frac{dv_{oq}}{dt} + \omega C_f v_d = i_{qL} - i_q \tag{3-12}$$

where ω is the angular speed of dq axis, v_d, v_q are the inverter output voltage in dq frame, v_{od}, v_{oq} are the capacitor voltage in dq frame, i_{dL}, i_{qL} are the inductor current in dq axis, i_d, i_q are the load side current in dq axis. The mathematical model can be plotted in block diagram shown in Fig. 3-2.

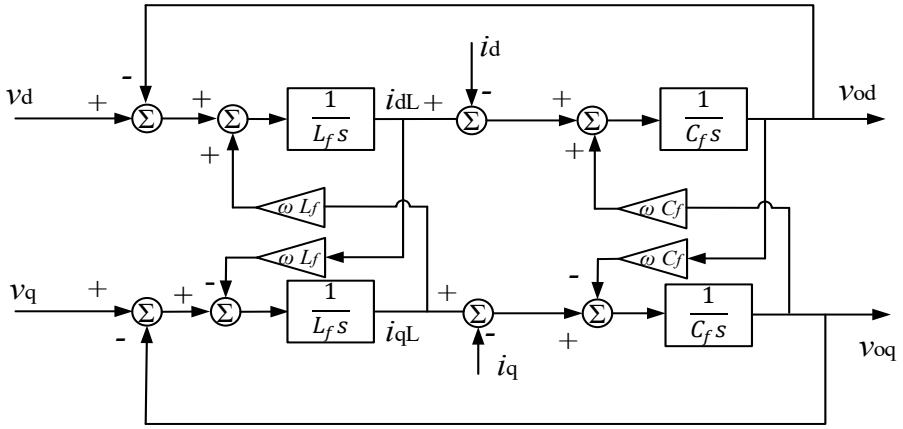

Fig.3-2 Mathematical model of inverter.

3.1.3 Capacitor Bank and Load Model

The mathematical model of excitation capacitor is written in the d-q frame as [8]

$$pv_{dc} = \frac{(i_{dl} - i_{ds})}{C} - v_{qs}\omega_r \tag{3-13}$$

$$pv_{qc} = \frac{(i_{ql} - i_{qs})}{C} + v_{ds}\omega_r \tag{3-14}$$

where i_{dl} and i_{ql} are load currents in d-q frame, v_{dc} and v_{qc} are the excitation capacitor voltages in the d-q frame. Due to parallel connection of excitation capacitors with the induction generator, there are v_{dc}=v_{ds} and v_{qc}=v_{qs}.

In this paper the induction machine is delta connected, the loads are star connected. The mathematical model for the resistive load under this conditions can be written in the *abc* frame as $R_{la} = \frac{V_{sa}}{3i_{la}}$, $R_{lb} = \frac{V_{sb}}{3i_{lb}}$, $R_{lc} = \frac{V_{sc}}{3i_{lc}}$, where V_{sa}, V_{sb}, V_{sc} is the generated three phase line to line voltage and i_{la}, i_{lb}, i_{lc} is the load current.

3.2 Emulation of the SEIG System with Unbalanced Loads

3.2.1 Emulation System

Fig. 3-3 shows the flow chart of the power electronic converter-based SEIG emulation system based on dSPACE 1103. Firstly, the power electronic converter output currents and voltages are detected and sent to the dSPACE analog to digital interface. Then those values are converted into the d-q rotating frame. The measured output current of the power electronic converter functions as the induction generator stator current. Then the reference stator voltages are used to obtain the d-q frame based on the built SEIG model. By comparing the actual voltage and current in the converter with the reference voltage and current signals, the outer voltage loop and inner current loop control and the PWM control signals are generated. Then, the digital output interface of dSPACE is used to deliver the PWM signals to control the power electronic converter. Therefore, the power as an actual generator flows through the power electronic converter, while no physical induction machine is needed in the test.

The established SEIG system model is investigated on the developed emulation setup. A schematic diagram of the SEIG machine emulator is shown in Fig. 3-4, including the power level and the control level. The inverter shown in Fig. 3-4 is a standard two-level converter. By controlling the inverter in the proposed manner to mimic the machine behavior, the performance of the electric machine can be obtained prior to the physical prototype.

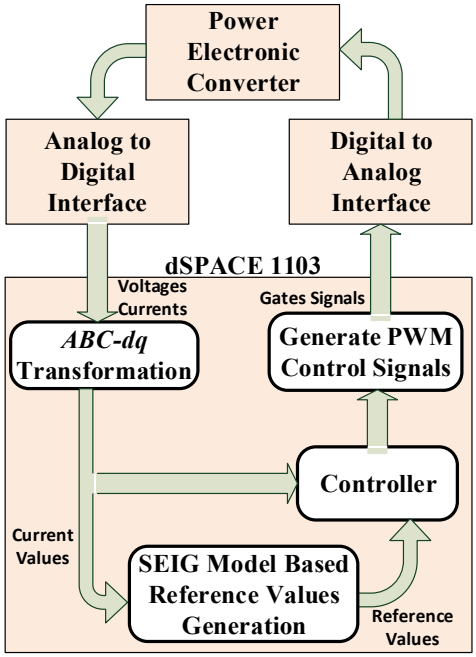

Fig.3-3 Implementation of proposed SEIG emulation system.

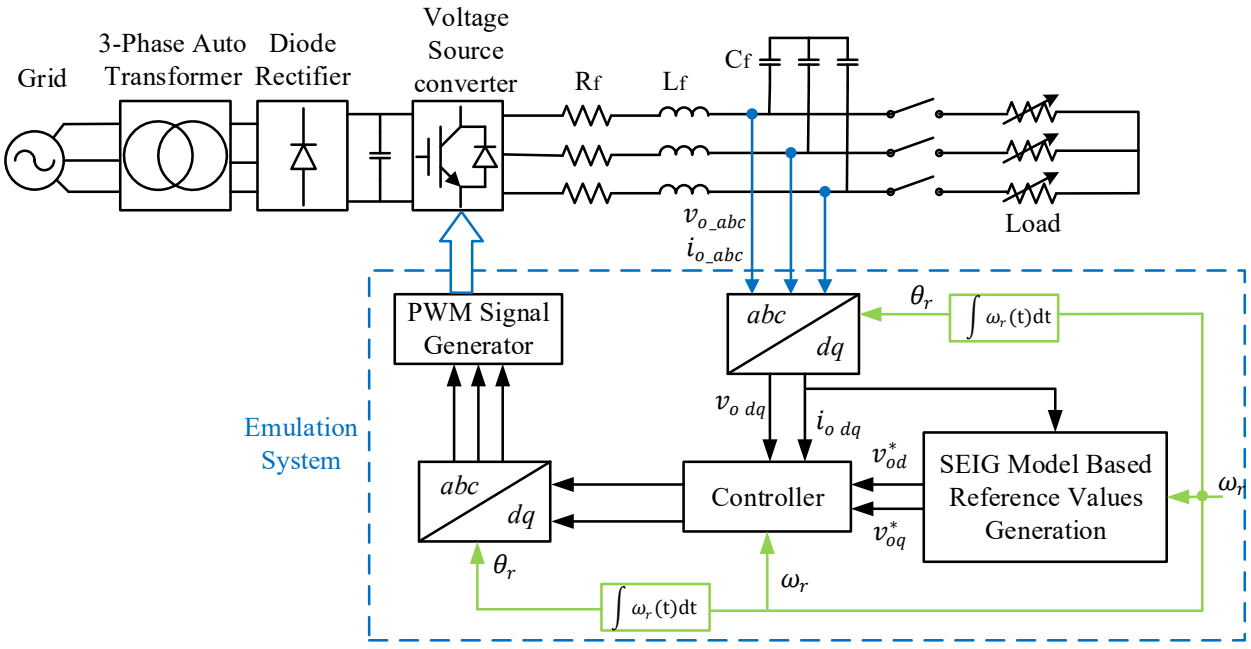

Fig.3-4 Proposed SEIG emulation system.

3.2.2 Control Strategy

To control the SEIG emulation system shown in Fig. 3-4, the induction generator model and control system are run in the d-q frame. The reference frame of control system is fixed in the rotor. Thus the *abc* to *dq* frame and *dq* to *abc* frame are performed with transformation angle $\theta = \theta_r$. This angle is obtained from rotor speed as follows:

$$\theta = \theta_r = \int \omega_r\,(t)dt + \theta_r(0)\ ,\ \omega_r = \frac{P}{2}\omega_m \tag{3-15}$$

where ω_m is the mechanical angular speed of the generator.

Fig. 3-5 shows the block diagram of voltage controller. Firstly, three sets of variables are measured and sent to dSPACE from the hardware. They are the inverter output current i_{i_abc}, the voltage v_{o_abc} of the load, and the current i_{o_abc} of the load. Then, the measured voltages and currents are converted in the dq frame by the Park transform, to perform the control in the two-phase rotating frame.

The three-phase load of the emulator and the induction generator model in the dSPACE platform are connected by load currents i_{o_abc}. The measured load currents together with excitation capacitor current in the SEIG model are used to calculate the stator voltages and currents. Therefore, the command load voltages v_{od}^* and v_{oq}^* in the *dq* frame and the rotor speed ω_r can be obtained from the SEIG model. Then, by comparing v_{od}^* and v_{oq}^* with v_{od} and v_{oq}, the voltage controller gives the command load currents i^*_{id} and i^*_{iq} for the inner-loop current controller. The current controller shown in Fig. 3-6 then obtains the command inverter output voltages v^*_{id} and v^*_{iq}, used as the modulating waveforms of the PWM in the form of m^*_d and m^*_q in Fig. 3-4. In the last step of the control method, m^*_d and m^*_q are reverse transformed to the three-phase stationary frame to obtain the three-phase sinusoidal waveforms for the PWM generator.

The inductor L_f and shunt capacitance C_f filter provide a low impedance path for switching current harmonics resulted from the pulse-width modulated output voltage originated by the converter. The proportional-integral (PI) compensator $G_i(s)$ is given as

$$G_i(\mathrm{s}) = K_{pi} + \frac{K_{Ii}}{s} \tag{3-16}$$

The output voltage control is given as

$$G_v(\mathrm{s}) = K_{pv} + \frac{K_{Iv}}{s} \tag{3-17}$$

where K_{pi} and K_{Ii} are the PI-controller gains for the current control scheme. K_{pv} and K_{Iv} are the PI-controller gains for the voltage control scheme.

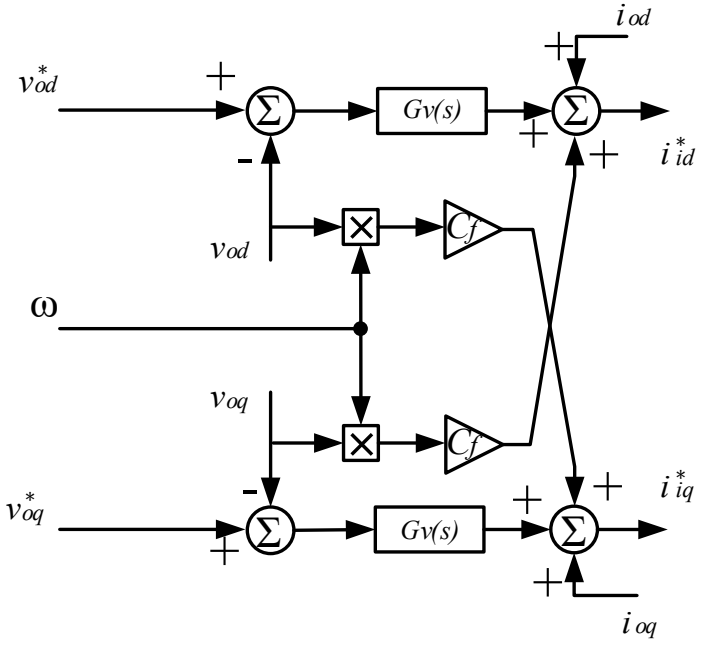

Fig.3-5 Block diagram of voltage controller.

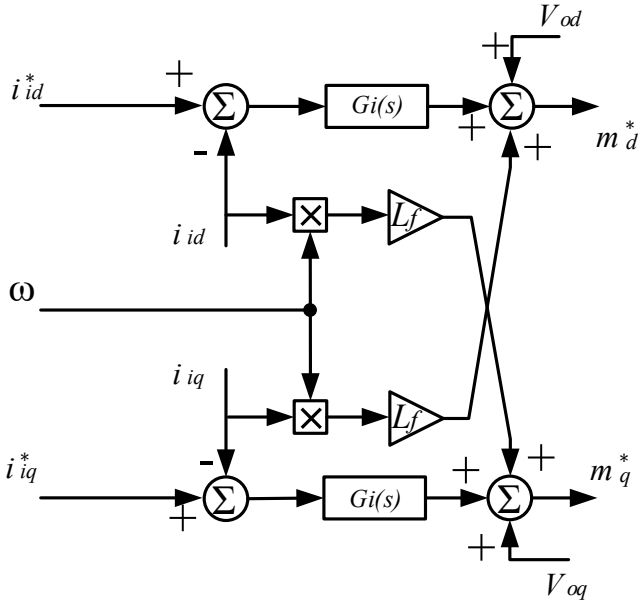

Fig.3-6 Block diagram of current controller.

3.3 Simulation and Experimental Results

First, the parameters of the machine are measured by using the no-load test, direct-current test and blocked-rotor test, to obtain the machine impedances of a 5-hp induction machine. Then the obtained machine parameters are used in the developed SEIG model of the emulator for testing balanced and unbalanced load conditions. To obtain system performances, the developed SEIG system model is simulated in Matlab/Simulink to verify the developed emulation results.

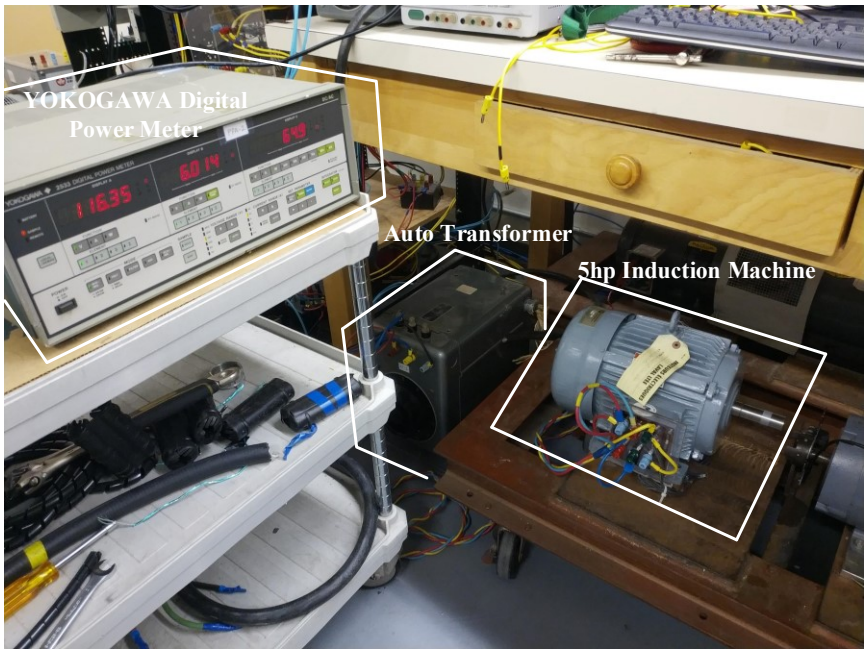

Fig.3-7 Experimental setup for the induction machine parameters measurement.

Fig. 3-7 shows the experimental setup, which is used to obtain the parameters of the machine. During this test, the speed of the induction machine is adjusted from zero to rated speed without load by changing the autotransformer. A YOKOGAWA digital power meter is cascaded with the autotransformer and induction machine for measuring current, voltage and power factor. Table I lists the measured and computed parameters of the machine.

By decreasing the voltage of autotransformer from the maximum voltage to the point that current starts to increase [65], the saturation characteristics are obtained, as shown in Fig. 3-8. It can be seen that when the voltage goes below 40V, there is a significant increase in the drawn current from 0.5 to 1.5 A, which is due to the reduction in the supply voltage leading to an increase in the slip and the current increases accordingly.

TABLE 3-1 Measured Steady State 5-hp Induction Machine Parameters

I. Parameter	Value
Stator resistance R_s	1.01 Ω
Rotor resistance R_r	1.04 Ω
Magnetizing reactance X_m	55.96 Ω
Stator leakage reactance X_{ls}	1.46 Ω
Rotor leakage reactance X_{lr}	3.41 Ω

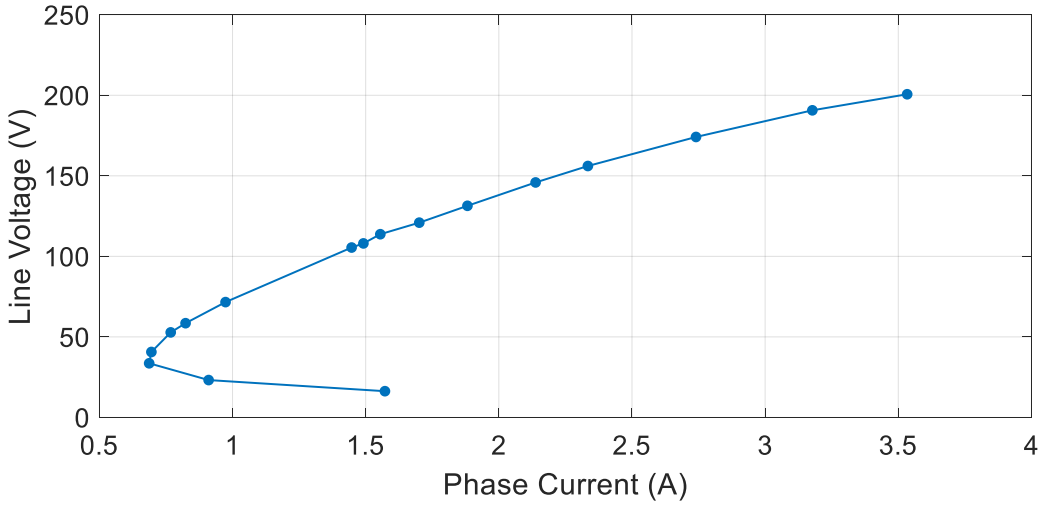

Fig.3-8 Saturation characteristics.

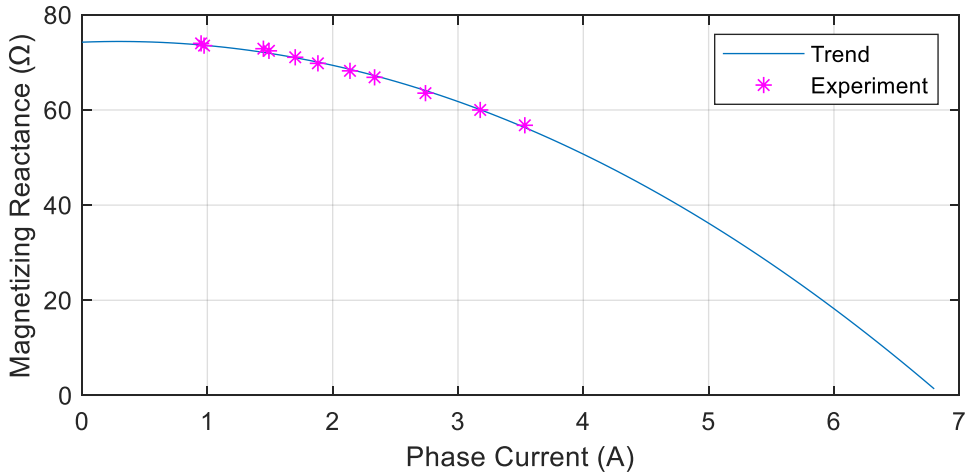

Fig.3-9 Magnetization curve.

Fig. 3-9 shows the magnetizing curve and its saturation characteristics. The relationship between the computation and experiment shows the validity of the parameters extracted from the actual machine for the SEIG model.

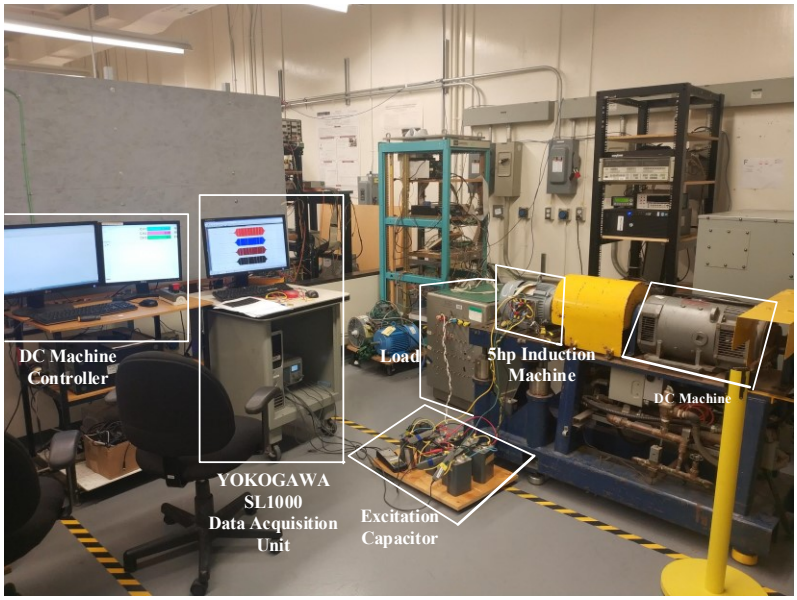

Fig.3-10 Experimental setup for the SEIG system.

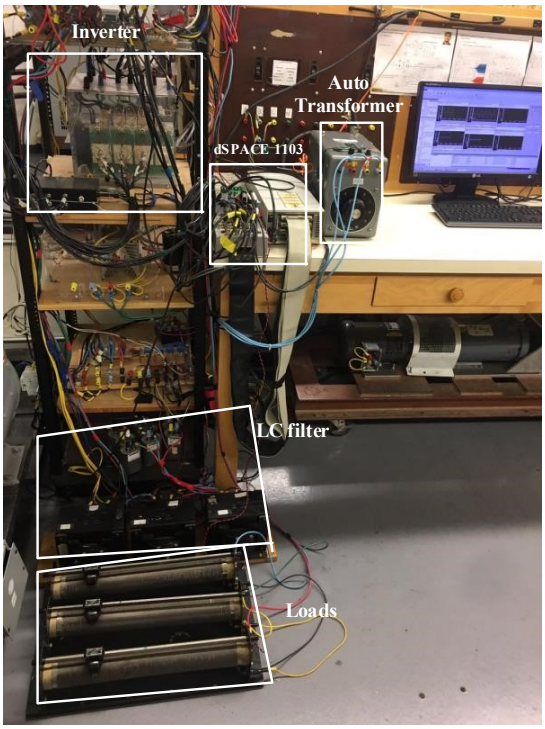

(b)

Fig.3-11 Experimental setup for the SEIG emulator.

Fig. 3-10 indicates the experimental setup for the actual SEIG system. A YOKOGAWA SL1000 PC-based data acquisition unit is used to measure load voltage, stator voltage, load current and excitation capacitor current. The DC machine is coupled to the induction generator as a prime mover, which is controlled to maintain a constant output speed for the induction machine.

The experimental setup of the proposed SEIG emulator system is shown in Fig. 3-11, based on the proposed system schematic diagram shown in Fig. 3-4. It consists of an autotransformer that connects the power electronic converter to the grid. The converter includes a cascaded AC-DC rectifier and two-level voltage source inverter, working as the emulating converter. The real-time controller, dSPACE 1103, receives the current and voltage signals from the loads, runs the SEIG system model, and controls the inverter in real time. The induction-capacitive (LC) coupling filter and resistive load bank are also shown in Fig. 3-11.

3.3.1 Voltage Buildup at No-Load

Fig. 3-12 shows the voltage build up results of the stator voltage occurring within 1 sec. Comparing the results of the actual system, model-based simulation, and emulation, the stator line-to-line voltage V_{LL} reaches around 220 V, verifying the machine model and emulation setup at start up.

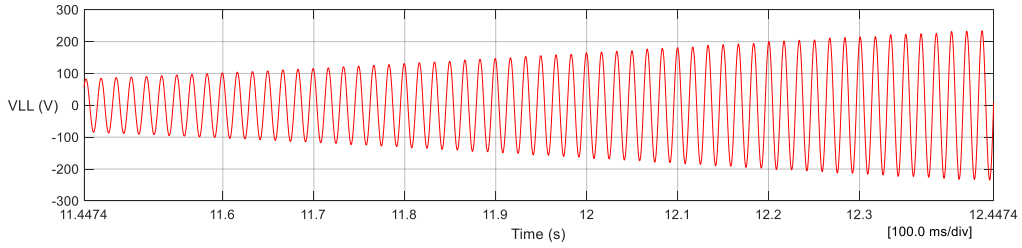

(a)

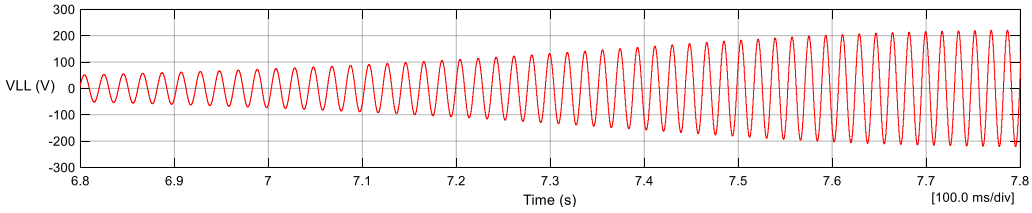

(b)

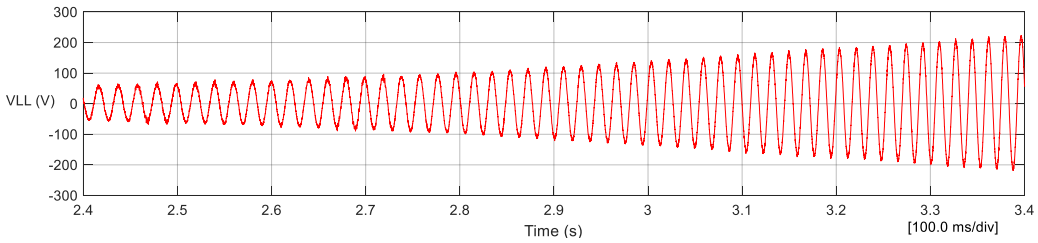

(c)

Fig.3-12 Stator voltage build up under balanced condition: (a) Actual SEIG results, (b) model-based simulation results, (c) emulation results.

3.3.2 Balanced Condition

To verify the accuracy of the built model, the balanced condition is firstly performed, and results from simulation, emulation setup, and the experiment are compared . Figs. 3-13 and 3-14 show the experimental results and simulation results from the developed system model. In this condition loads are chosen as $R_{la} = R_{lb} = R_{lc} = 20\ \Omega$.

Fig. 3-13 has the results of a balanced load stator voltage. Fig. 3-14 shows the corresponding results of load currents. Comparing Figs. 3-13 (a) with (b), 3-14 (a) with (b), from the simulation results of the built system model and the measured results of the actual SEIG it is clear that they match well. This demonstrates that the developed SEIG model is accurate and can be utilized to investigate the SEIG performance in the emulator. Comparing Fig. 3-13 (a) with (c), Fig. 3-14 (a) with (c), the emulation results from the experimental setup and measured actual SEIG results, it can be seen that they match well. This validates the emulation setup and its ability to investigate the SEIG performance under unbalanced conditions. The overlap waveform of each condition is also shown in Fig. (d) for comparison.

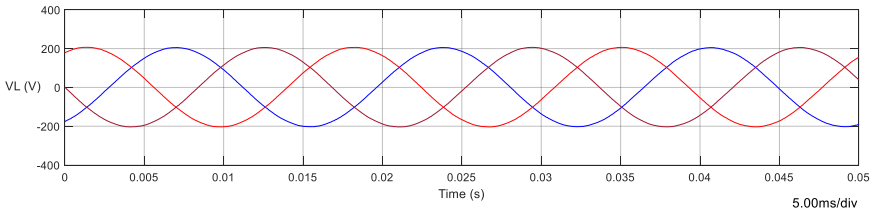

(a)

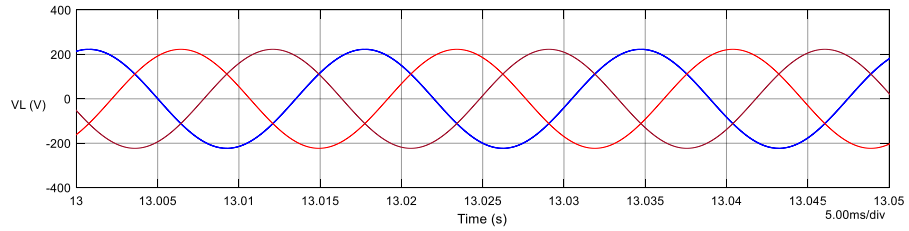

(b)

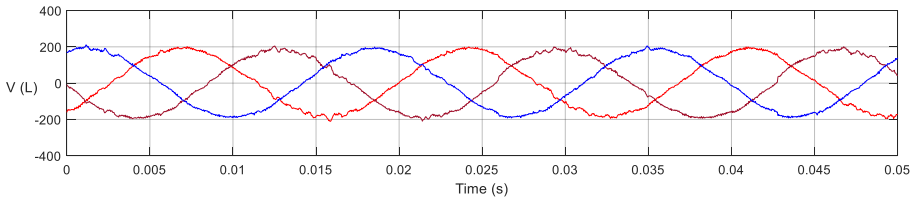

(c)

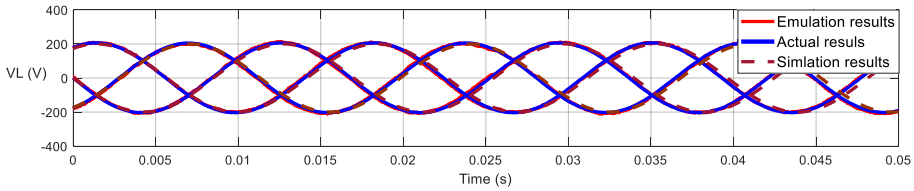

(d)

Fig.3-13 Stator voltages under balanced condition: (a) Actual SEIG results, (b) model-based simulation results, (c) emulation results, (d)overlap results.

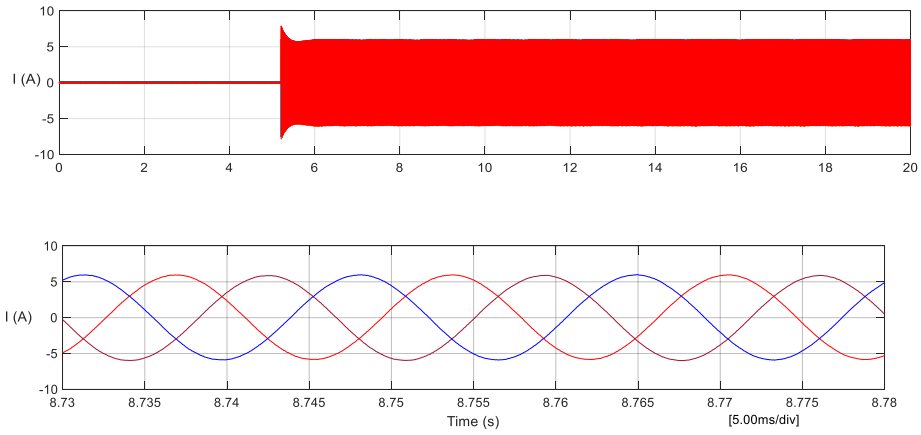

(a)

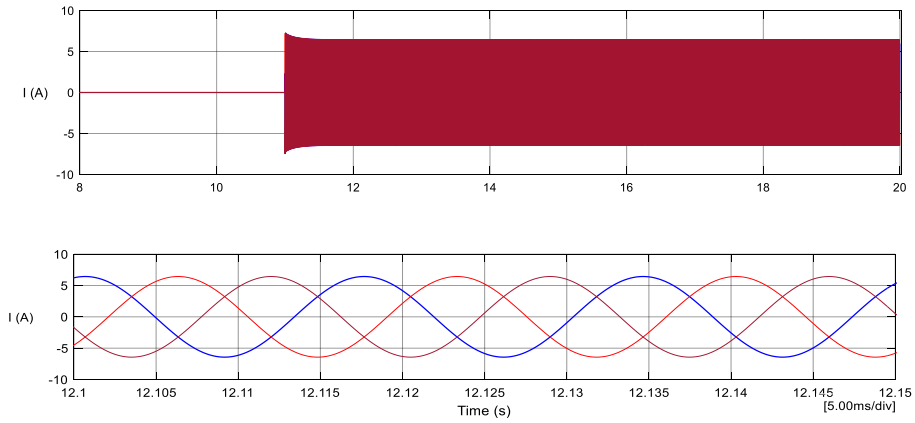

(b)

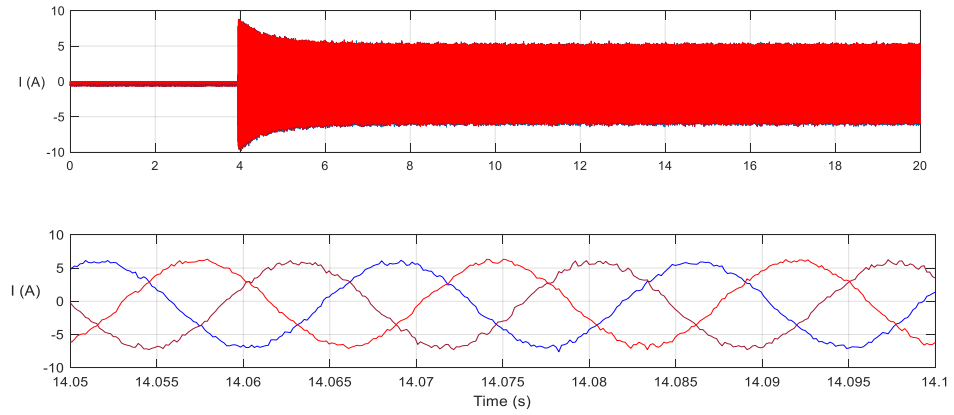

(c)

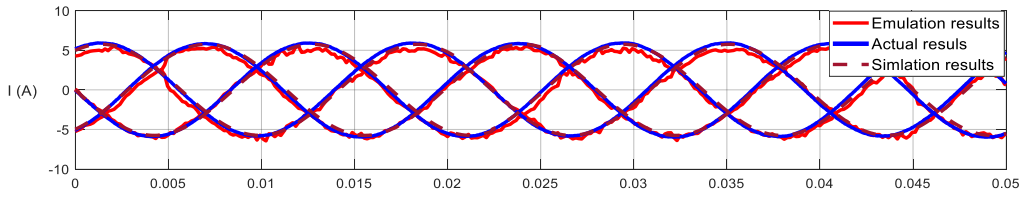

(d)

Fig.3-14 Load currents under balanced condition: (a) Actual SEIG results, (b) model-based simulation results, (c) emulation results, (d) overlap results.

3.3.3 Unbalanced Condition

In order to investigate the unbalanced condition, three sets of unbalanced loads are considered: (I) $R_{la} = 13.44\ \Omega$, $R_{lb} = 20\ \Omega$, $R_{lc} = 40\ \Omega$, (II) $R_{la} = R_{lb} = 20\ \Omega$, $R_{lc} = 40\ \Omega$, (III) $R_{la} = R_{lb} = 20\ \Omega$, R_{lc}

= 13.44 Ω, according to available values of the load bank in the lab and the rated machine's stator current. They are applied to the actual SEIG system, simulation and emulation experiment.

Case I :

Experimental and simulation results of the stator voltages and load currents are shown in Figs. 3-15 and 3-16.

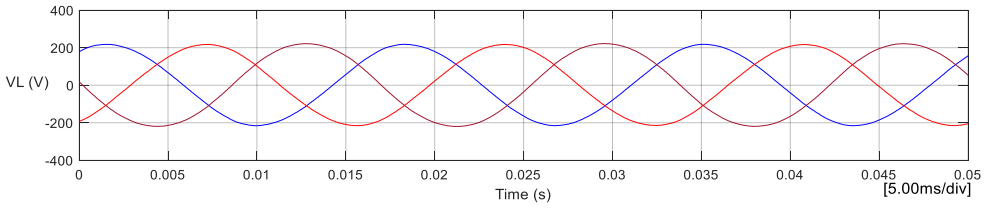

(a)

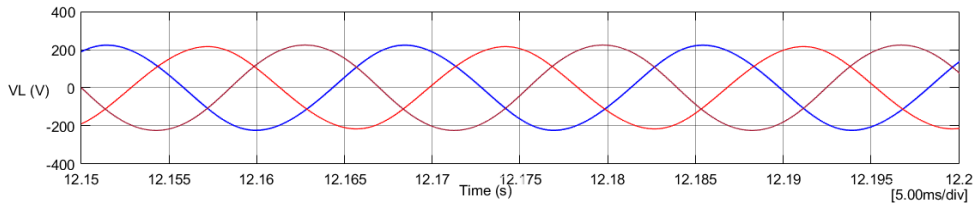

(b)

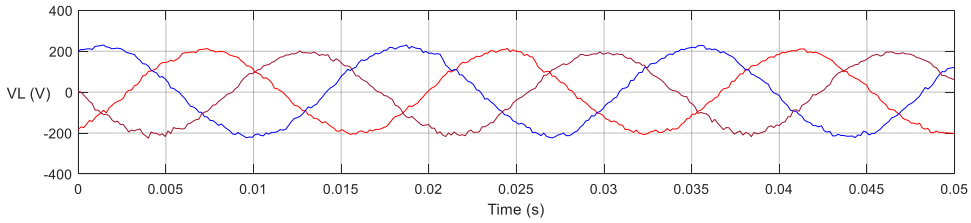

(c)

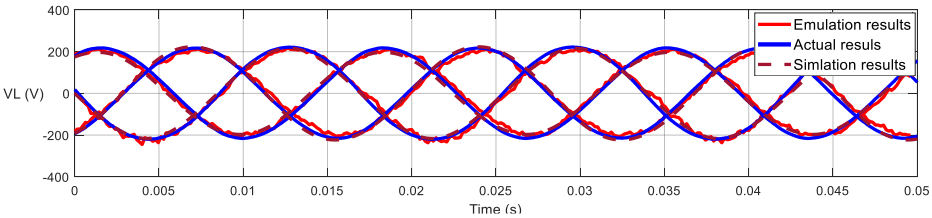

(d)

Fig.3-15 Stator voltages under unbalanced condition I: (a) experimental results, (b) model-based simulation results, (c) emulation results, (d)overlap results.

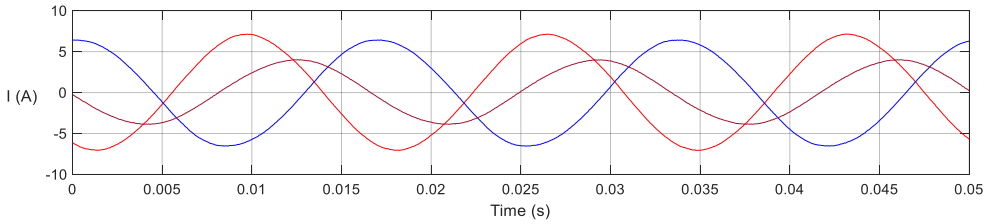

(a)

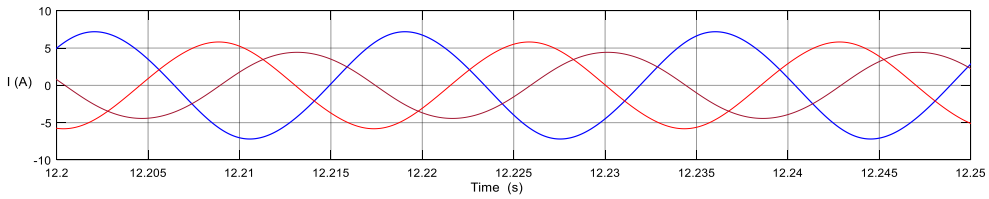

(b)

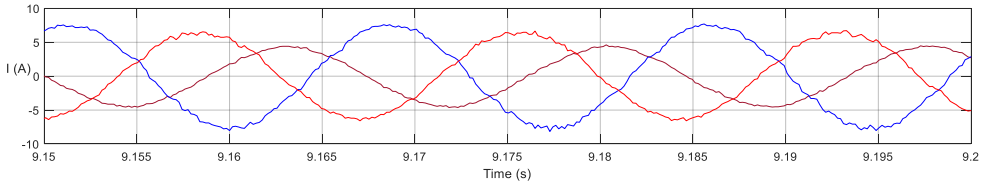

(c)

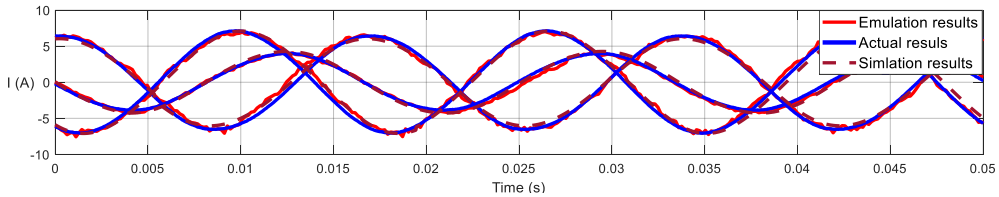

(d)

Fig.3-16 Load currents under unbalanced condition I: (a) experimental results, (b) simulation results, (c) emulation results, (d)overlap results.

By comparison of Figs. 3-15 (a) with (b), 3-16 (a) with (b), it can be seen that the magnitude, phase, and frequency from actual SEIG results match well with the simulation results based on the developed model. Furthermore, by comparing the results shown in Fig. 3-15 (a) with (c), Fig. 3-16 (a) with (c), it can be seen that the magnitude, phase, and frequency from the actual SEIG results matches well with the emulation results based on established emulator system. This validates the developed emulation setup and it can be used to accurately perform the SEIG system running under

unbalanced conditions. The overlap waveform of each condition also shown in Fig. (d) for comparison.

Furthermore, from Figs. 3-13 and 3-15, it can be seen that the magnitude and frequency of stator voltages do not vary, even under unbalanced conditions. Comparing Figs. 3-14 with 3-16 it can be seen that the load currents have different magnitudes due to the unbalanced condition.

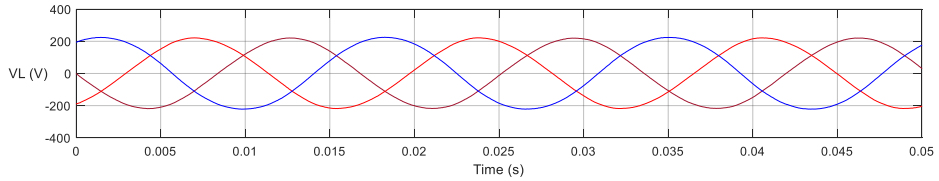

(a)

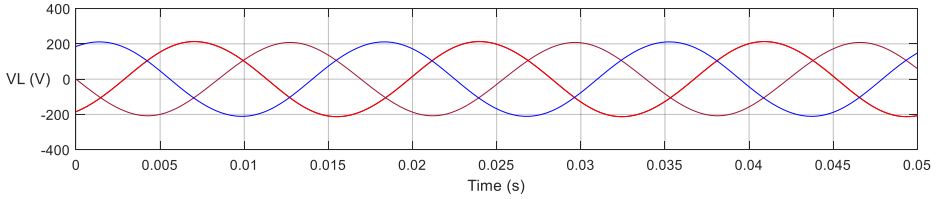

(b)

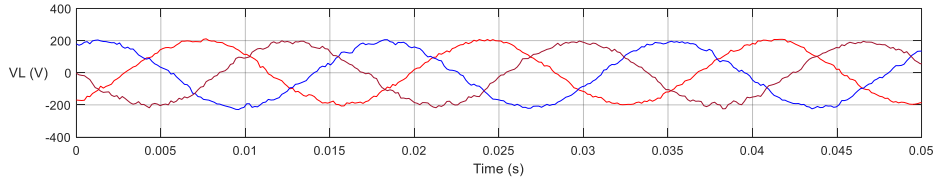

(c)

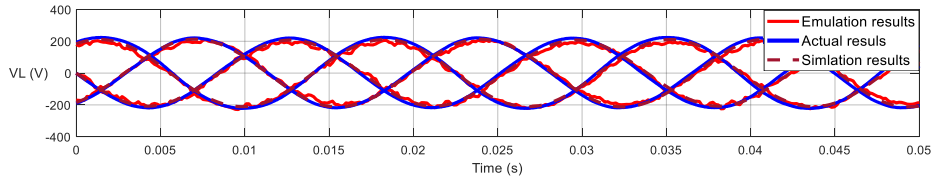

(d)

Fig.3-17 Stator voltages under unbalanced condition II: (a) experimental results, (b) simulation results, (c) emulation results, (d)overlap results.

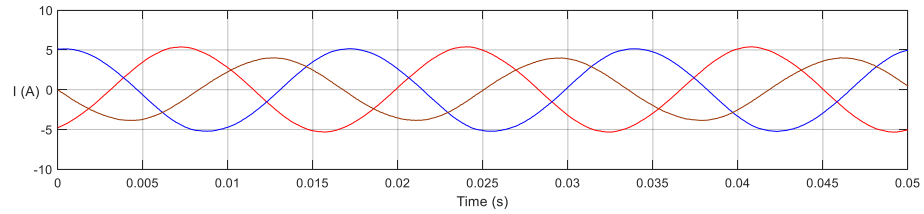

(a)

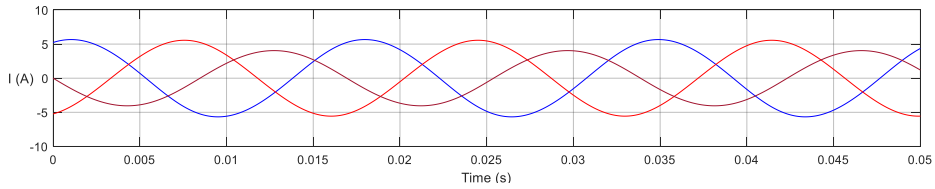

(b)

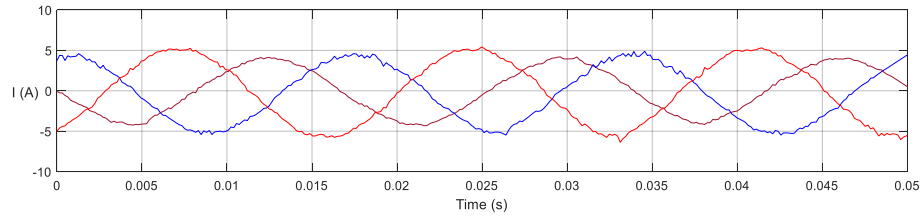

(c)

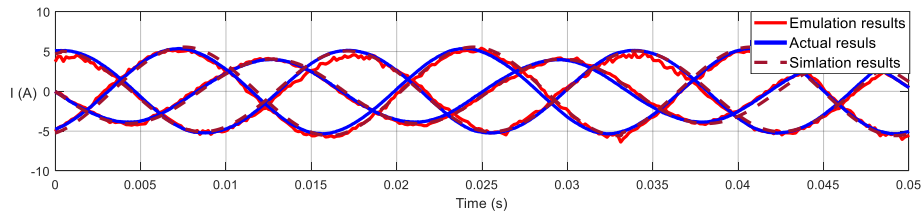

(d)

Fig.3-18 Load currents under unbalanced condition II: (a) experimental results, (b) simulation results, (c) emulation results, (d)overlap results.

Case II:

In this case, unbalanced resistive loads with $R_{la} = 20\ \Omega$, $R_{lb} = 20\ \Omega$, $R_{lc} = 40\ \Omega$ are applied to the SEIG system, and the results are shown in Fig. 3-17 and 18.

Case III:

In this case, unbalanced resistive loads with $R_{la} = 20\ \Omega$, $R_{lb} = 20\ \Omega$, $R_{lc} = 13.44\ \Omega$ are applied to the SEIG system, the results are shown in Fig. 3-19 and 20.

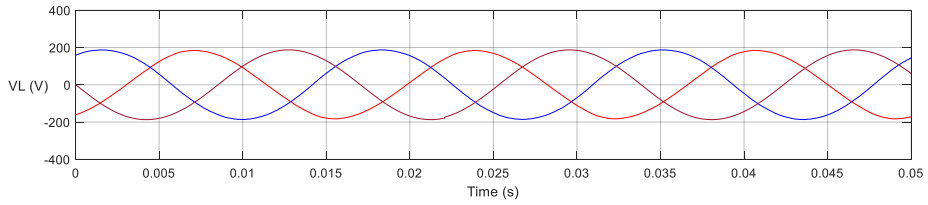

(a)

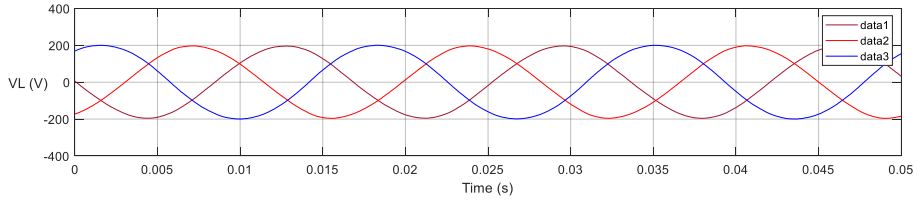

(b)

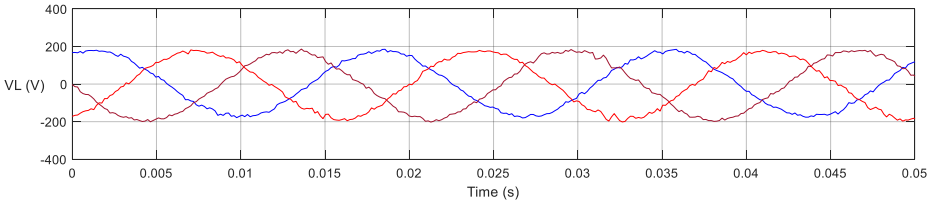

(c)

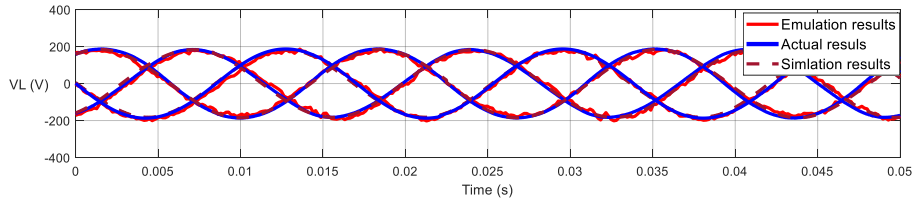

(d)

Fig.3-19 Stator voltages under unbalanced condition II: (a) experimental results, (b) simulation results, (c) emulation results, (d)overlap results.

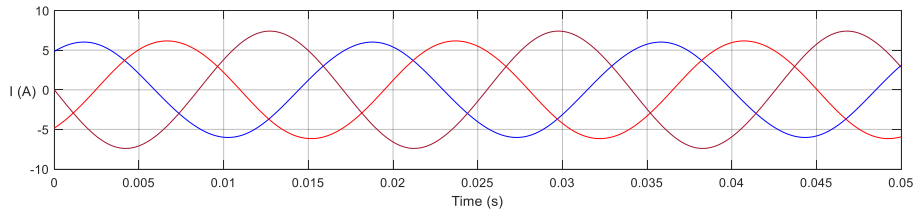

(a)

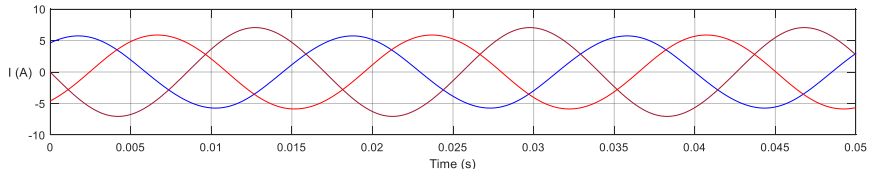

(b)

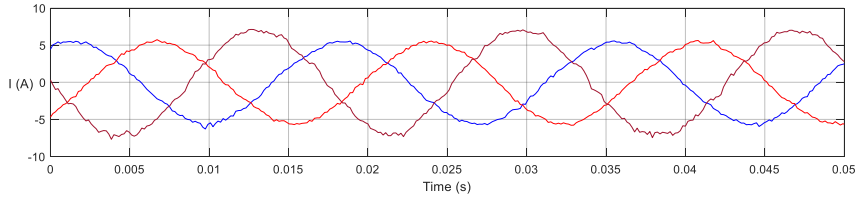

(c)

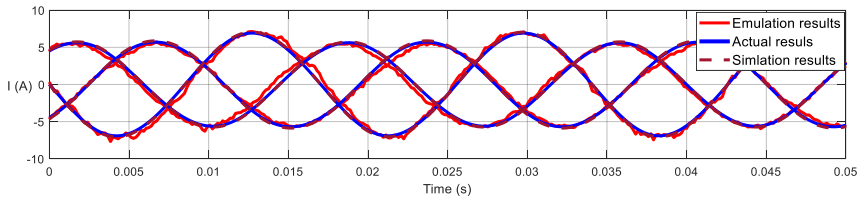

(d)

Fig.3-20 Load currents under unbalanced condition III: (a) experimental results, (b) simulation results, (c) emulation results, (d)overlap results.

Comparing these three different unbalanced cases one can observe that the unbalanced load mostly affects the current amplitude, the voltage phase and amplitude will remain balanced. Moreover the overlap waveform under each figure proved the accuracy of emulation and simulation results.

3.3.4 Transient Performance

To investigate the dynamic performance for the developed emulator, the transient results have been shown below. Fig. 3-21 shows the transient performance of the emulator during switching from the no-load operation to balanced load condition: R_{la} = 20 Ω, R_{lb} = 20 Ω, R_{lc} = 20 Ω. Fig. 3-22 depicts the circumstances of no load to unbalanced loads: R_{la} = 13.44 Ω, R_{lb} = 20 Ω, R_{lc} = 40 Ω. Fig. 3-23 shows the transient from balanced loads to the one phase load changes to R_{lc} = 10 Ω. Fig. 3-24 shows the transient from balanced loads to two phases change to 10 Ω. From the result of transient performance shown below it can be seen that the emulator can responded well

during dynamic scenarios.

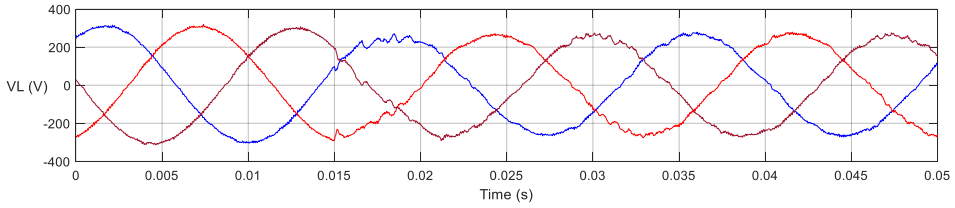

(a)

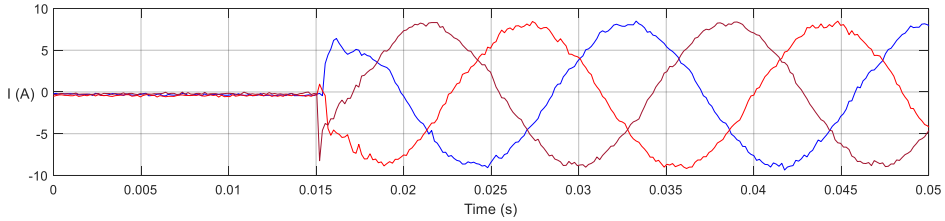

(b)

Fig.3-21 Transient performance of the emulator under balanced condition: (a) voltage, (b) current

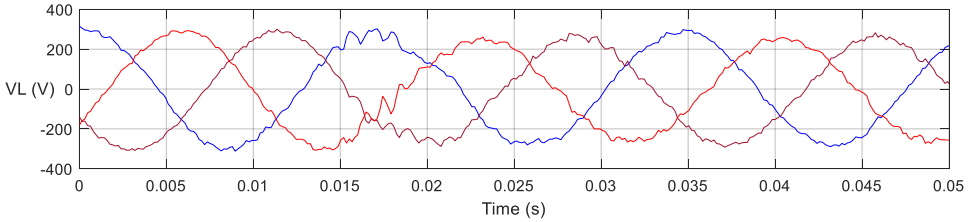

(a)

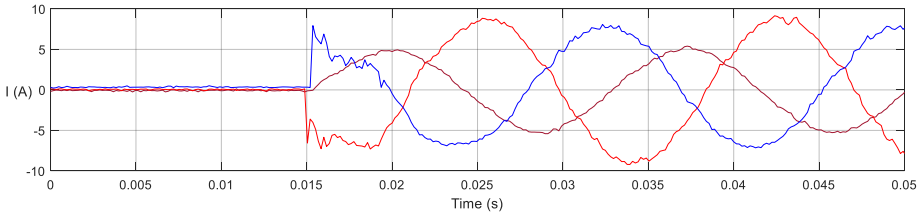

(b)

Fig.3-22 Transient performance of the emulator under unbalanced condition: (a) voltage, (b) current

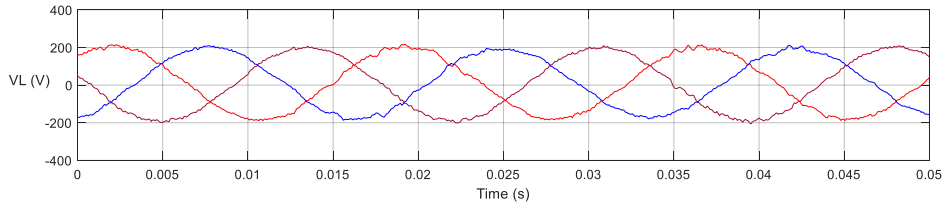

(a)

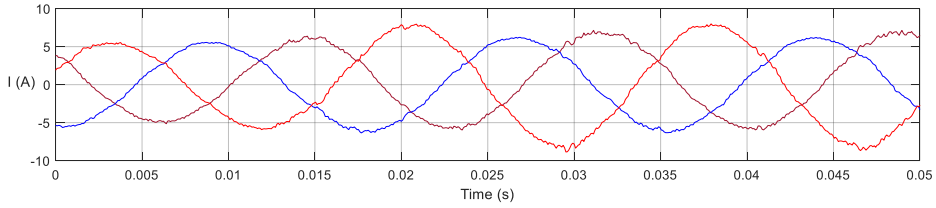

(b)

Fig.3-23 Transient performance with one phase load change: (a) voltage, (b) current.

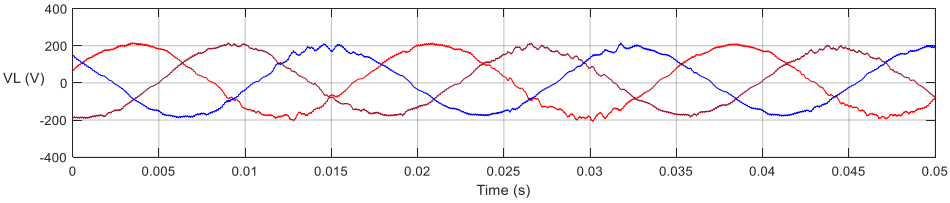

(a)

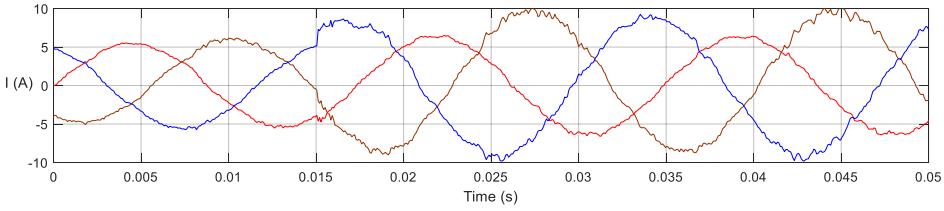

(b)

Fig.3-24 Transient performance with two phase load change: (a) voltage, (b) current.

The THD analysis results are shown in Table II above, it can be observed that for the actual machine and simulation results, there is an acceptable agreement between the results. In general, the THD values are relatively low. However, for the emulation results the THD values show there are some distortions, this is mainly due to the switching frequency of the PWM technique that is used to switch the six power electronic devices, a higher bandwidth converter would produce lower ripples.

TABLE 3-2 THD Analysis

THD	Balanced conditions	Unbalanced conditions
Actual machine voltage	1.70%	2.34%
Actual machine current	1.87%	1.77%
simulation voltage	2.25%	2.27%
simulation current	2.25%	2.27%
Emulation voltage	4.49%	5.6%
Emulation current	6.18%	6.09%

3.3.5 Nonlinear Loads Condition

Fig. 3-25 shows a schematic diagram of the SEIG system suppling a nonlinear loads. Fig. 3-26 (a) shows the experimental setup for the actual SEIG system. A DC machine is coupled with induction machine and working as a mechanical power input, supplying power to the induction machine. The induction machine used in the SEIG system is a 5-hp 4 poles machine. The machine parameters obtained from no-load test, direct-current test, and blocked-rotor test are shown in Table I [66]. The induction machine is then connected with excitation capacitors and the nonlinear load, which is a diode AC-DC converter with resistive R load.

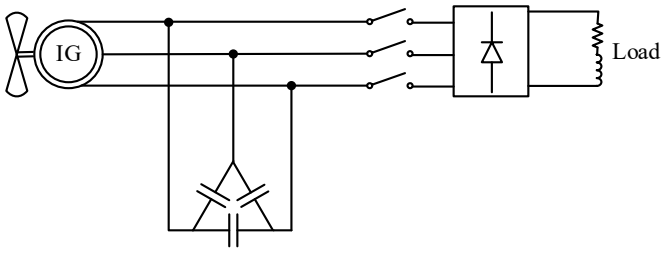

Fig.3-25 Schematic diagram of the SEIG system suppling nonlinear load.

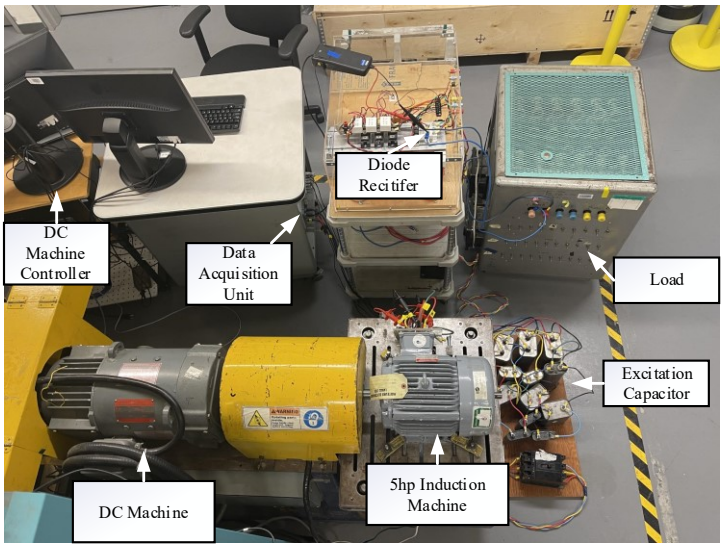

(a)

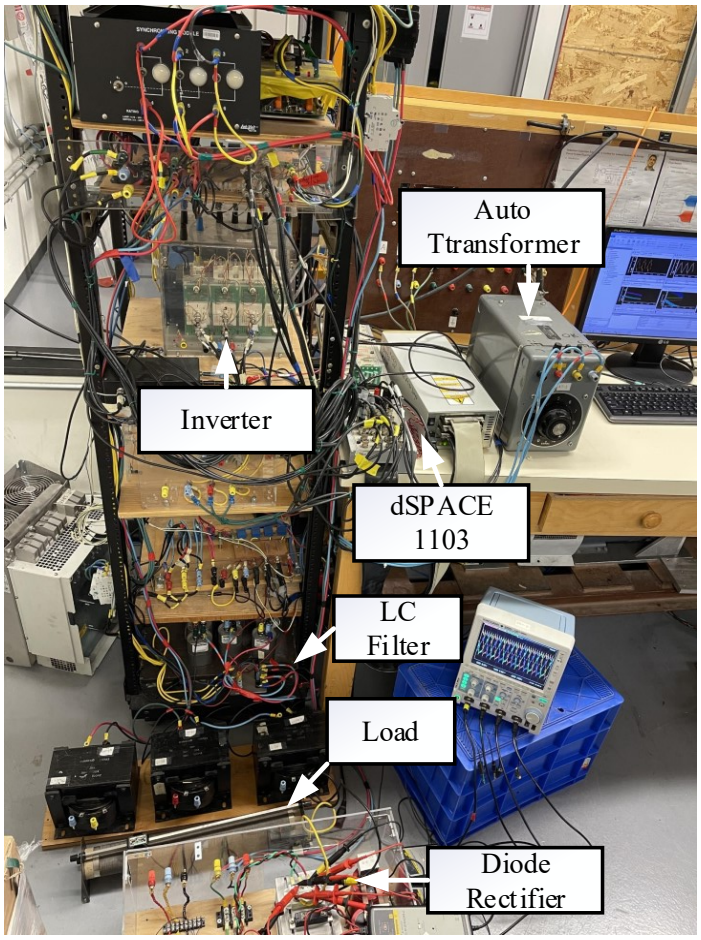

(b)

Fig.3-26 Experiment setup: (a) actual SEIG system, (b) emulation system.

Fig. 3-26 (b) shows the experimental setup for the built SEIG emulator system. As the schematic diagram shown in Fig. 3-4, the system consists of an autotransformer connected to the grid and supplying power to a cascaded AC-DC rectifier and two-level voltage source inverter. dSPACE 1103 is used to receive the measured voltages and currents to generate PWM signals to control inverter switches. The LC filter and nonlinear load are also shown in Fig. 3-26 (b).

The simulation has been done for the nonlinear loading condition, a three-phase diode converter serving a DC load is considered as nonlinear loads. The DC load is a resistance R load. Simulation results of stator voltages and load currents are shown in Fig. 3-27.

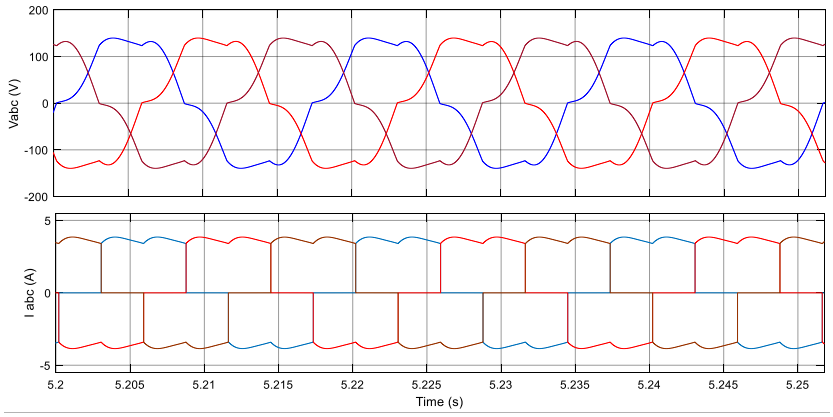

Fig.3-27 Simulation results of SEIG system voltage and current.

Fig. 3-28 shows the experimental results comparison of actual SEIG and emulation stator voltages and currents. The comparison of simulation results in Fig.3-27 with actual results in Fig. 3-28 demonstrate validity of the established mathematical model. By comparing actual results and emulation results in Fig.3-28, it can be see that the voltage and current of emulation results are tracking with actual SEIG results in amplitude and phase. The comparison of emulation results with actual results proved validity of proposed SEIG emulation system.

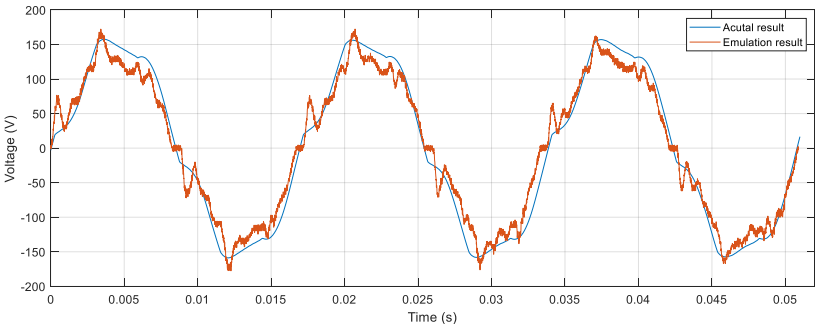

(a)

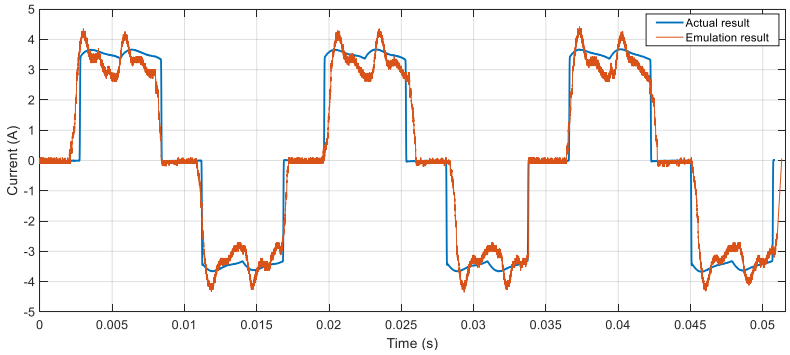

(b)

Fig.3-28 Experiment results comparison (a) voltages (b) currents.

3.4 Summary

This Chapter proposed an SEIG emulation system for unbalanced load conditions. The parameters of a three-phase, 5-hp, squirrel cage induction machine were estimated accurately via experimental procedures. The machine model was run in a real-time simulator and interfaced with a power electronic converter to emulate the performance of the generator. The unbalanced load is connected to the emulator. The emulation results, simulation results, and actual SEIG system results were performed and compared. The results showed that the machine emulator performed well and could be used to study the characteristics of a SEIG system, instead of the real SEIG setup, verifying the validity of proposed PHIL based SEIG emulator. Besides, the results of magnitudes and frequencies of voltages in SEIG system did not vary significantly under unbalanced conditions. Therefore, the SEIG can be an efficient and economical system to supply isolated areas, even when the loads are unbalanced.

Chapter 4.
Induction Machine Emulation with Stator Winding Faults

4.1 Introduction

Similar to Chapter 4, this Chapter is devoted to the development of the mathematical model of an induction machine operating under a condition of winding faults. Stator windings faults may cause the machine shut down, operate at reduced capacity, damage the connected loads, etc. In the most cases, stator inter-turn faults in induction machines are related to the short circuit of a few turns of a stator phase winding. According to [68-69], around 36% induction machine faults are related to the inter-turn short circuits. Moreover, generally induction machine coils are insulated with others in slots, and the end windings region is also insulated. Hence, the highest probability for inter turn faults is between the inter turns in the same coil [70], as shown in Fig. 4-1. Therefore, this chapter will focus on the inter turn short circuit of windings in the same phase group.

The diagram of inter turn short circuit in the same phase group is shown in Fig. 4-2 [71]. In the figure, the inter turn short circuit happened between points *a* and *b*.

It can be seen from the Fig. 4-2, that after short circuit occurs, the turns of phase winding decreases. After short circuit occur, high current will flow in the shorted winding, which will produce excessive heat. Then the temperature in the shorted area will rise. With the temperature growing over the limiting value, complete damage on the winding insulation will occur. Besides, the high circulating current in the shorted turn will cause the coil to oscillate at twice the line

frequency under both radial and tangential directions. The oscillation will make the rotor rub the stator, which will cause further issues.

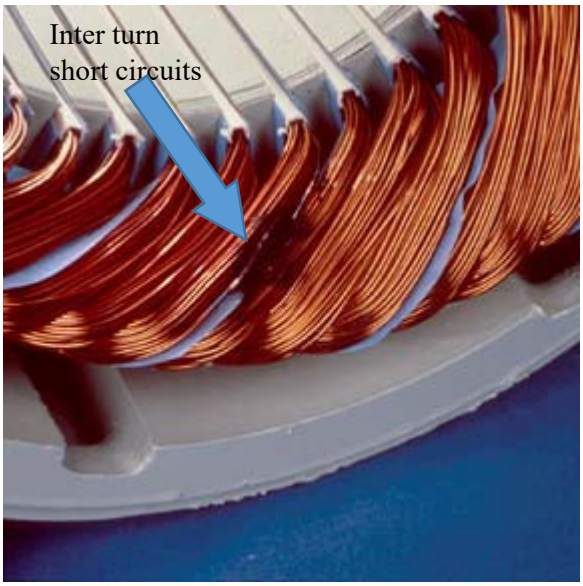

Fig. 4-1 Inter turn short circuit.[69]

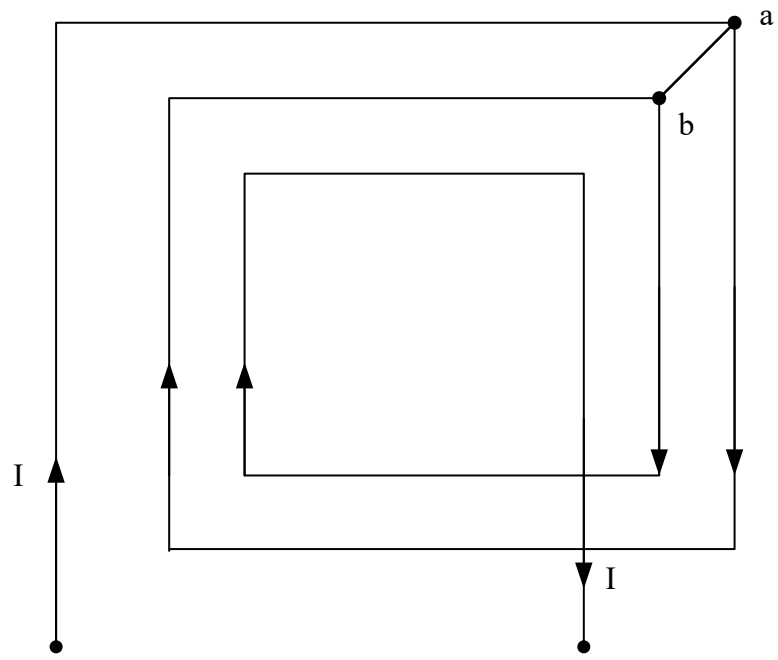

Fig. 4-2 Diagram of inter turn short circuit.[71]

Furthermore, the research regarding the machine fault conditions is widely investigated. [72] and [73] mention that around 40% of faults are caused by inter-turn short circuits and another 40% of faults are caused by bearing failures in IMs. Stator current envelopes are used to identify the

broken rotor bars and stator windings inter-turn short circuits in [72]. Periodograms have applied to diagnose IM stator winding fault in [73]. The Fourier transform is also carried out on the stator current to identify the stator winding faults by current spectra [74-77]. However, even though the stator winding fault is detected, an accurate mathematical model of the corresponding fault condition is still required. The modelling of the IM inter-turn short circuit is investigated in [26] and [16]. Only the mathematical model in the three-phase abc reference frame is discussed and details of the model were not provided. The research in [78] proposed the stator winding fault IM model in the dq frame, whereas, the effect of faults on the machine torque is not considered, which makes it unable to investigate loading conditions. The mathematical model in [79] discussed IM transient performance with stator winding turn faults, with a maximum of 2% shorted turns applied and no experimental current waveforms provided. That model is also used in [80] to establish a mathematical model suitable for computer simulation, where the transformation is referred to a frame rotating at an arbitrary angular velocity. Even though there is extensive research on modelling of IM fault conditions, they still lack implementation verifications.

4.2 Establishment of IM Mathematical Model with Winding Fault

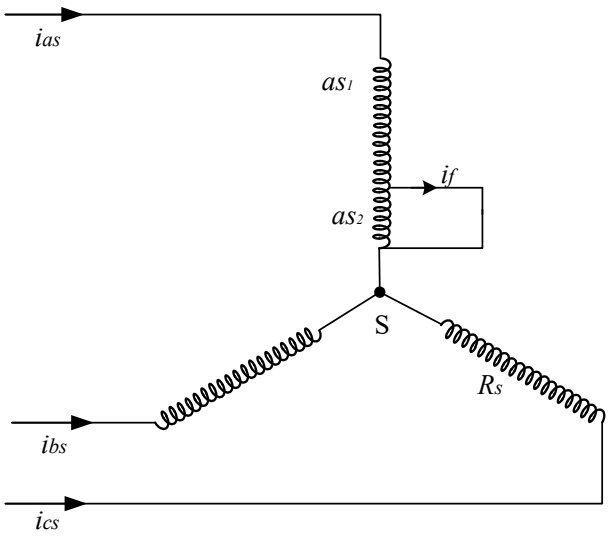

Fig. 4-3 Layout of IM stator winding fault.

An inter-turn short circuit in one phase of the stator winding is shown in Fig. 4-3 [16]. It can be seen that the number of turns in the winding decreases when a short circuit occurs. High currents will then flow in the shorted winding, which will produce excessive heat. The temperature rise in the shorted area can increase over its rated value, causing permanent damage to the winding and

surrounding area. Also, the high circulating current in the shorted turn will cause the coil to vibrate at twice the line frequency in both radial and tangential directions. The vibration might cause the rotor to rub up against the stator, which will cause further damage.

The conventional induction machine model given in the three-phase *abc* reference frame only considers three turns of stator windings in *abc* phases.

4.2.1 Machine Model with Winding Fault in the abc Reference Frame.

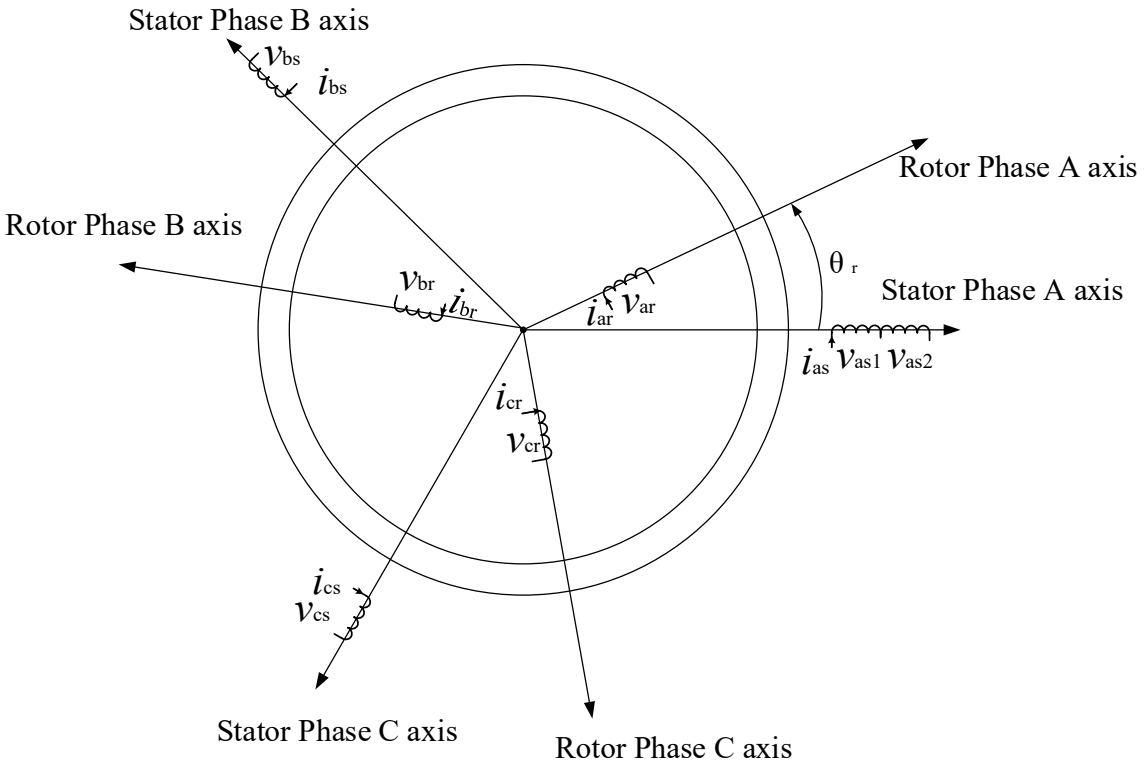

Fig. 4-4 Schematic diagram of three phase induction machine with winding fault

Fig. 4-4 shows the schematic diagram of the induction machine with the winding fault. From Figs. 4-3 and 4-4, the winding of phase A is separated into as_1 and as_2, where as_2 represents the shorted turns and i_f is the short circuit current, thus the current flowing through the un-shorted turns will be $(i_{as} - i_f)$. Using β to denote the fraction of shorted turns, then (1− β) will denote the fraction of remaining turns on the faulted phase. The stator voltage of phase A is also split into v_{as1} and v_{as2}.

Then the stator and rotor voltages for an induction motor with an inter-turn short circuit fault can be expressed as [79]

$$v_s = R_s i_s + \frac{d\lambda_s}{dt} \tag{4-1}$$

$$0 = R_r i_r + \frac{d\lambda_r}{dt} \tag{4-2}$$

where

$v_s = [v_{as1}\ v_{as2}\ v_{bs}\ v_{cs}]^T, i_s = \left[i_{as}\ \left(i_{as} - i_f\right)\ i_{bs}\ i_{cs}\right]^T, \qquad i_r = [i_{ar}\ i_{br}\ i_{cr}]^T$

$\lambda_s = [\lambda_{as1}\ \lambda_{as2}\ \lambda_{bs}\ \lambda_{cs}]^T = \mathrm{L}_{ss} i_s + \mathrm{L}_{sr} i_r, \qquad \lambda_r = [\lambda_{ar}\ \lambda_{br}\ \lambda_{cr}]^T = \mathrm{L}_{rs} i_s + \mathrm{L}_{rr} i_r$

The resistance matrices in (4-1) and (4-2) are given by

$$\mathbf{R}_s = r_s \cdot diag[(1-\beta)\ \beta\ 1\ 1] \tag{4-3}$$

$$\mathbf{R}_r = r_r \cdot I_{3*3} \tag{4-4}$$

The stator leakage inductance of the shorted turns is $\beta \mathrm{L}_{ls}$, where $\beta \mathrm{L}_{ls}$ is the per-phase leakage inductance. Similarly, the stator leakage inductance of the remaining un-shorted turns is $(1\text{-}\beta)\mathrm{L}_{ls}$.

The calculation of inductance between faulted phase A and phase B, C has to be expanded to calculate the mutual inductance in between.

The equation for the magnetizing inductance is

$$\mathrm{L}_{ms} = \frac{N_1 N_2}{\mathrm{R}_m} \tag{4-5}$$

where N_1 and N_2 are the number of turns in each part of the coil, respectively. R_m is the reluctance of the mutual path and can be calculated by $\mathrm{R}_m = \frac{l}{\mu_i A}$, where l is the magnetic path length, A is the cross mutual area of the flux path, μ_i is the permeability of the iron.

For the two different turns as_1 and as_2 on shorted phase, the number of turns will be N_1= (1- β) N and $N_2 = \beta$ N, where N is the number of turns in each phase stator winding. Thus according to (5), the magnetizing inductance for as_1 will be $(1-\beta)^2 \mathrm{L}_{ms}$ and $\beta^2 \mathrm{L}_{ms}$ for as_2. The magnetizing inductance between as_1 and as_2 will be $\beta(1-\beta)\mathrm{L}_{ms}$.

For as_1 and phase B, N_1= (1- β) N and $N_2 =$ N, according to (5), the magnetizing inductance

is (1- β) $L_{ms}\ cos\Upsilon$, which can be written as $-\frac{1-\beta}{2}L_{ms}$. Similarly, for as_2 and phase B, N_1= β N and N_2 = N, the magnetizing inductance can be directly written as $-\frac{\beta}{2}L_{ms}$. The magnetizing inductance between as_1 and as_2 in phase C can be calculated in the same way.

The stator inductance matrices can be written as follows:

$$L_{ss} = L_{ls}.diag\ [(1-\beta)\ \beta\ 1\ 1] + L_{ms}\begin{bmatrix} (1-\beta)^2 & \beta(1-\beta) & -\frac{1-\beta}{2} & -\frac{1-\beta}{2} \\ \beta(1-\beta) & \beta^2 & -\frac{\beta}{2} & -\frac{\beta}{2} \\ -\frac{1-\beta}{2} & -\frac{\beta}{2} & 1 & -\frac{1}{2} \\ -\frac{1-\beta}{2} & -\frac{\beta}{2} & -\frac{1}{2} & 1 \end{bmatrix} \tag{4-6}$$

$$L_{sr} = L_{ms} * \begin{bmatrix} (1-\beta)\cos(\theta_r) & (1-\beta)\cos(\theta_r+\gamma) & (1-\beta)\cos(\theta_r-\gamma) \\ \beta\cos(\theta_r) & \beta\cos(\theta_r+\gamma) & \beta\cos(\theta_r-\gamma) \\ \cos(\theta_r-\gamma) & \cos(\theta_r) & \cos(\theta_r+\gamma) \\ \cos(\theta_r+\gamma) & \cos(\theta_r-\gamma) & \cos(\theta_r) \end{bmatrix} \tag{4-7}$$

$$L_{rs} = L_{sr}^T \tag{4-8}$$

θ_r is the angle between stator phase A and rotor phase A, and ϒ=120°. The rotor leakage reactance L_{rr} is similar to the healthy machine.

For the shorted turns, the voltage and flux linkage equations are written as follows:

$$v_{as2} = r_s\beta\left(i_{as} - i_f\right) + \frac{d\lambda_{as2}}{dt} \tag{4-9}$$

$$\lambda_{as2} = \beta\begin{bmatrix} L_{ls}+L_{ms} \\ -\frac{1}{2}L_{ms} \\ -\frac{1}{2}L_{ms} \end{bmatrix}^T i_s + \begin{bmatrix} \cos(\theta_r) \\ \cos(\theta_r+\gamma) \\ \cos(\theta_r-\gamma) \end{bmatrix}^T i_r - \beta(L_{ls}+\mu L_{ms})i_f \tag{4-10}$$

Comparing with the conventional induction machine model, it can be seen that in the derived

faulted machine equations, the current i_f of the shorted turn is included and the voltage of phase A is separated into v_{as1} and v_{as2}, where v_{as2} is the voltage of the shorted turn.

4.2.3 Machine Model in dq Reference Frame

Applying the *dq* transformation of the above-derived machine model, the stator voltages become

$$v_{qs} = r_s i_{qs} + p\lambda_{qs} + \lambda_{ds}\omega_s - \frac{2}{3}\beta r_s i_f cos\theta \tag{4-11}$$

$$v_{ds} = r_s i_{ds} + p\lambda_{ds} - \lambda_{qs}\omega_s - \frac{2}{3}\beta r_s i_f sin\theta \tag{4-12}$$

For the shorted turns, the voltage equation is

$$0 = r_f i_f - p\lambda_{as2} - \beta r_s\left(i_{ds}cos\theta + i_{qs}sin\theta - i_f\right) \tag{4-13}$$

The stator and rotor currents in the *dq* reference frame can be obtained as:

$$i_{qs} = \lambda_{qs}\mathrm{a}_2 - \lambda_{qr}\mathrm{a}_3 + (\mathrm{L}_r\mathrm{a}_5 - \mathrm{L}_m\mathrm{a}_6)i_f cos\theta \tag{4-14}$$

$$i_{ds} = \lambda_{ds}\mathrm{a}_2 - \lambda_{dr}\mathrm{a}_3 + (\mathrm{L}_r\mathrm{a}_5 - \mathrm{L}_m\mathrm{a}_6)i_f sin\theta \tag{4-15}$$

$$i_{qr} = \lambda_{qr}\mathrm{a}_4 - \lambda_{qs}\mathrm{a}_3 + (\mathrm{L}_s\mathrm{a}_6 - \mathrm{L}_m\mathrm{a}_5)i_f cos\theta \tag{4-16}$$

$$i_{dr} = \lambda_{dr}\mathrm{a}_4 - \lambda_{ds}\mathrm{a}_3 + (\mathrm{L}_s\mathrm{a}_6 - \mathrm{L}_m\mathrm{a}_5)i_f sin\theta \tag{4-17}$$

$$i_f = \frac{-\lambda_{as2} + (\mathrm{a}_7 i_{qs} + \mathrm{a}_8 i_{qr})cos\theta + (\mathrm{a}_7 i_{ds} + \mathrm{a}_8 i_{dr})sin\theta}{\mathrm{a}_6} \tag{4-18}$$

where

$\mathrm{a}_0 = \mathrm{L}_s\mathrm{L}_r - L_m^2$; $\mathrm{a}_1 = 1 - \frac{L_m^2}{\mathrm{L}_s\mathrm{L}_r}$; $\mathrm{a}_2 = \frac{1}{\mathrm{a}_1\mathrm{L}_s}$; $\mathrm{a}_3 = \frac{\mathrm{L}_m\mathrm{a}_7}{\mathrm{L}_r}$; $\mathrm{a}_4 = \frac{1}{\mathrm{a}_1\mathrm{L}_r}$; $\mathrm{a}_5 = \frac{2}{3}\frac{\beta\mathrm{L}_s}{\mathrm{a}_0}$; $\mathrm{a}_6 = \frac{2}{3}\frac{\beta\mathrm{L}_m}{\mathrm{a}_0}$; $\mathrm{a}_7 = \beta\mathrm{L}_s$; $\mathrm{a}_8 = \beta\mathrm{L}_m$.

The electromagnetic torque expressed in the *dq* reference frame is obtained as

$$T = \frac{3}{2}\frac{P}{2}\mathrm{L}_m\left(i_{qs}i_{dr} - i_{ds}i_{qr}\right) + \frac{P}{2}\beta\mathrm{L}_m i_f\left(i_{qr}sin\theta - i_{dr}cos\theta\right) \tag{4-19}$$

4.3 IM Emulation System

Fig. 4-5 shows the schematic diagram of the established IM emulator, two power electronic converters are connected back to back, where one runs as an active front-end converter (AFEC) and another one working as an emulator converter.

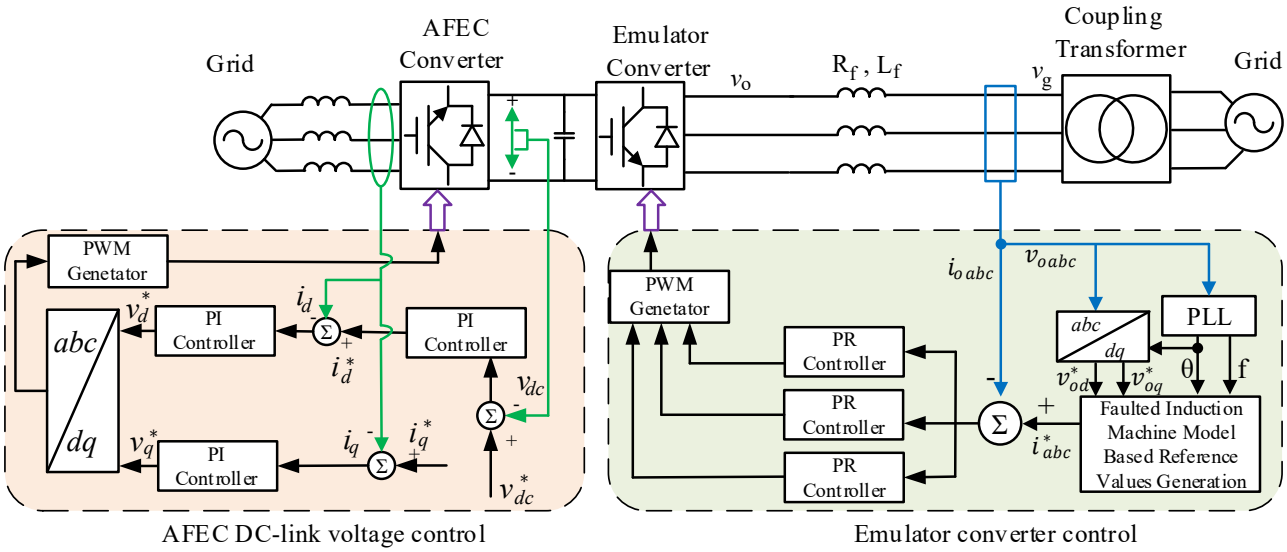

Fig. 4-5 Schematic diagram of faulted IM emulator.

The objective of the AFEC is to maintain a constant DC link voltage and provide a bidirectional power flow of the emulation converter, thus to allow the system to emulate a machine in both generating and motoring modes. The control diagram of the AFEC is included in Fig. 3. The reference signal V_{dc}^* is compared with the measured DC link voltage v_{dc}, which obtains the d-axis reference current i_d^* through a proportional-integral (PI) regulator. The ac side currents are transformed into dq reference frame components as i_d and i_q. The references i_d^* and i_q^* are compared with the measured actual currents i_d and i_q, respectively. Then the PI regulator generates the voltage references, which are transferred from dq to the abc reference frame, and then sent to the modulator to produce gate signals. The AFEC control has been well established in [81].

The control objective of the emulator converter is to draw currents from the grid, according to the stator current from the faulted machine model. To achieve that, the measured emulator side voltages $v_{o\,abc}$ are transformed to the dq frame as v_{od}^* and v_{oq}^*, then the voltage is input to the fault model to generate reference stator currents i_{abc}^*. The output currents $i_{o\,abc}$ of the emulation

converter are measured and compared with reference values generated by the established IM model, which includes stator winding faults. The error between i^*_{abc} and$i_{o\,abc}$ going through the PR regulator-based controller produces modulating waves for generating the pulsed gate signals, which are sent to the emulation converter to ensure the converter currents track the stator currents of the faulted IM. In this way, the emulation converter mimics machine behaviour, and the fault condition of the electric machine can be tested without a physical machine.

From Fig. 4-5, the dynamic relationship of the emulator converter can be written as

$$v_o = L_f \frac{di(t)}{dt} + R_f i(t) + v_g(t) \tag{4-20}$$

where v_o is the emulator converter output voltage, $v_g(t)$ is the grid voltage, L_f is the grid-side inductor and R_f is the inner resistance of the inductor. Then, from (4-20), the transfer function of the emulator converter can be written as:

$$G_{con}(s) = V_{dc} \frac{I(s)}{Vo(s)} = \frac{V_{dc}}{L_f s + R_f} \tag{4-21}$$

The transfer function of the PR controller can be written as:

$$G_{PR}^{abc}(s) = K_p + \frac{K_r s}{s^2 + \omega_0^2} \tag{4-22}$$

where K_p is the proportional gain, K_r is the resonant controller time constant, and ω_0 is the resonant angular frequency, which is set as the supply voltage angular frequency. The *PR* controller is having a very high gain in a narrow band around the resonance frequency, which makes it able to eliminate the steady-state error [82]. The frequency bandwidth of the *PR* controller is dependent on the resonant controller time constant K_r. The lower time constant will lead to a narrower bandwidth, correspondingly, a larger time constant will lead to a wider bandwidth.

Through the compensation of the *PR* regulator, the open-loop transfer function of the current controller becomes

$$G_{icom}(s) = G_{con}(s) G_{PR}^{abc}(s) = \frac{V_{dc}(K_p s^2 + K_r s + K_p \omega_0^2)}{L_f s^3 + R_f s^2 + L_f \omega_0^2 s + R_f \omega_0^2} \tag{4-23}$$

And the closed-loop transfer function is obtained as

$$H(s) = \frac{i(s)}{i^*(s)} = \frac{G_{con}(s)G_{PR}^{abc}(s)}{1+G_{con}(s)G_{PR}^{abc}(s)} \tag{4-24}$$

The PR controller is designed to have a high gain in a narrow band around the resonance frequency, which is 50 Hz in this paper. The controller gains can be obtained as

$$K_p = \frac{\omega_{bw}L_f}{V_{dc}}, K_r = \frac{\omega_{bw}R_f}{V_{dc}} \tag{4-25}$$

where ω_{bw} is the desired bandwidth, the value of ω_{bw} should be chosen higher than the ten times grid frequency and lower than one-fifth of the switching frequency. To eliminate high-order harmonics and achieve fast tracking dynamics, the bandwidth in this paper is set to one-tenth switching frequency, which is 1 kHz. As a result, the *PR* controller gains are $K_p = 0.0539$ and $K_r = 0.5386$, respectively.

The Bode plot of the *PR* controller $G_{PR}^{abc}(s)$ is shown in Fig. 4-6 (a). It can be observed that a high gain appears at the 50Hz resonant frequency, which reduces steady-state error. Fig. 4-6 (b) shows the Bode plot of $G_{con}(s)$ before compensation and the open-loop system after the *PR* controller compensation. It can be seen that after compensation, besides a high gain at the resonant frequency, the system cross-over frequency is improved from 1.17×10^5 rad/s to 6.28×10^3 rad/s, demonstrating the enhanced stability and fast response. Correspondingly, the closed-loop system shows stable magnitude and phase characteristics, as shown in Fig. 4-6 (c).

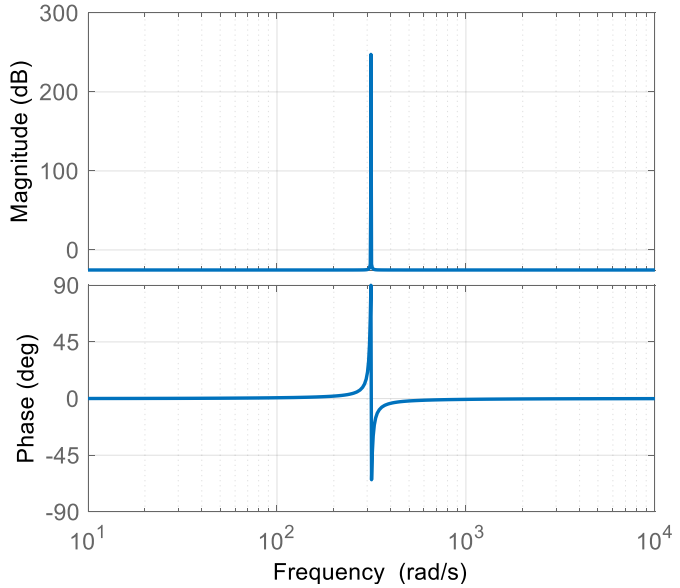

(a)

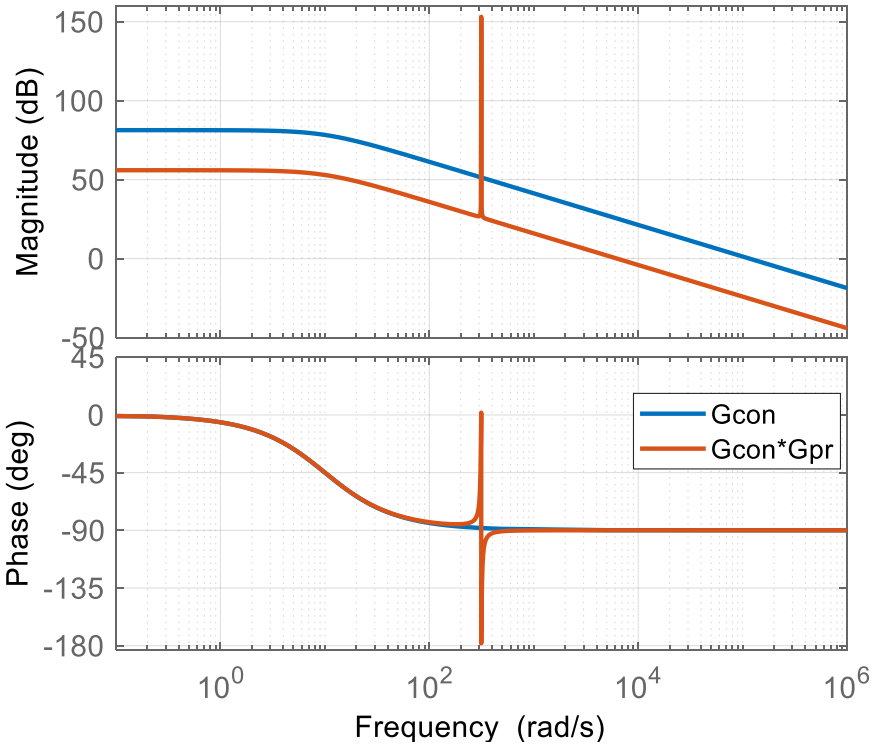

(b)

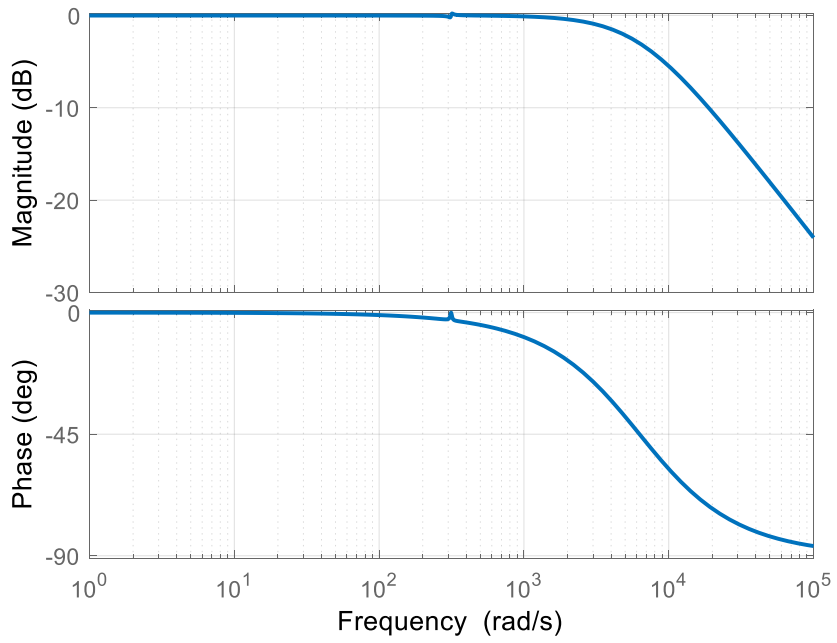

(c)

Fig. 4-6 Bode plot (a) PR controller, (b) open-loop after compensation, (c) closed-loop.

4.4 Simulation and Experimental Results

The experimental setup of the PHIL emulator system is shown in Fig. 4-7 (a). OP4510 HIL real-time simulator from OPAL-RT is used as an emulator controller. The AFEC connects to the grid through a three-phase autotransformer and a 1 *m*H coupling inductor per phase. The AFEC is controlled to maintain the DC link voltage at 350V. The inverter switching frequency is 10 kHz and the sampling time of the emulator controller is 20μs, to achieve an accurate real-time emulation.

The zoomed view of the AFEC and emulator converter is shown in Fig. 4-7 (b). The AC side of the emulator converter shown is connected to an isolation transformer through a coupling inductor in each phase, with the inductance chosen as 3 *m*H. The value of the inductor is chosen as the actual machine mean inductance, thus ensuring that the ripple current in the emulation results are close to the physical machine. An isolation transformer is used to prevent common-mode voltage and circulating currents in the circuit.

Two protection circuits are used in Fig. 4-7 for each converter. The zoomed view of protection circuits is shown in Fig. 4-7 (c). Once the over-current or over-voltage fault occurs in the emulation system, the hardware circuit will block gating pulses from the controller to the converters.

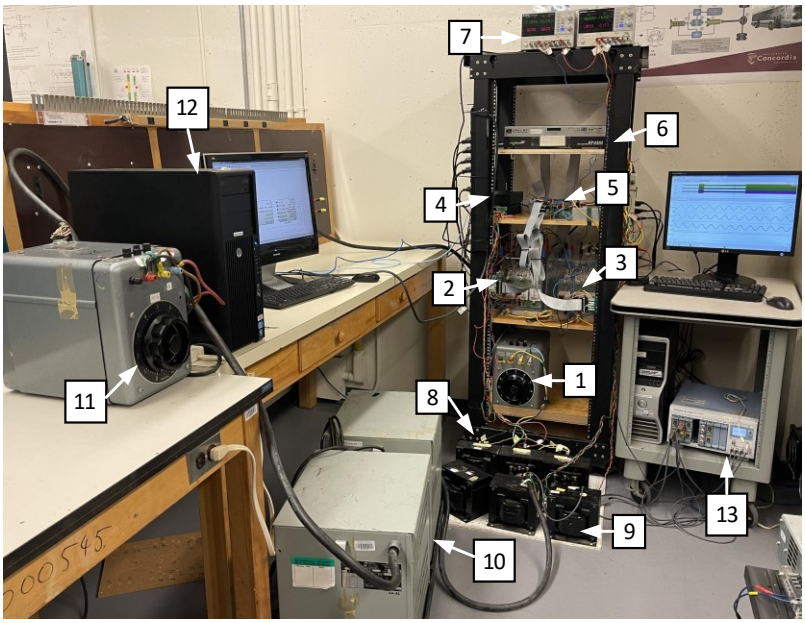

(a)

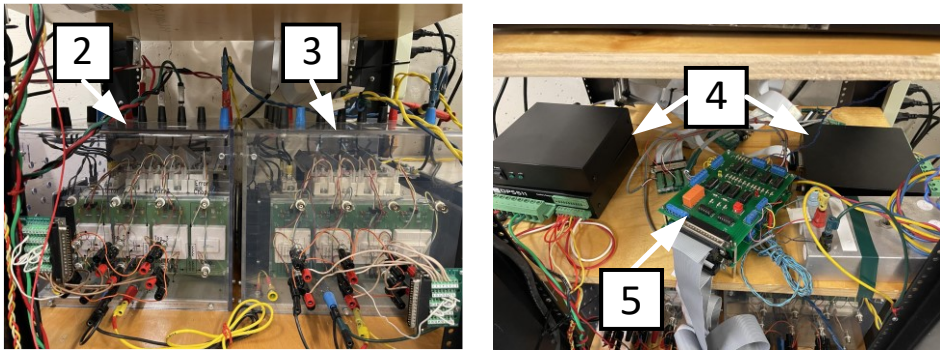

(b) (c)

Fig. 4-7 (a) Experimental setup of the emulator system (1) Auto transformer at the AFEC side (2) Active front-end converter (3) Emulator converter (4) Voltage and current sensors (5) Protection circuit (6) controller for the machine emulator (7) DC power supply for sensors and protection circuitry (8) Coupling inductors at the AFEC side (9) Coupling inductors at emulator converter side (10) Isolation transformer (11) Auto transformer on emulator side (12) PC for control (13) Data acquisition unit. (b) Zoom view of (2), (3). (c) Zoom view of (4), (5).

To investigate the proposed emulator and mathematical machine model, experimental tests are conducted on a three-phase, 250 W, 2-pole induction machine. As shown in Fig. 4-8, the machine has three extra terminals on the stator, which provides access to tapping within the winding. This allows for various portions of the phase winding to be short-circuited, behave as a stator inter-turn short circuit fault. Connecting top and bottom terminals will enable 5% of the turns to be shorted. Connecting the top terminal and middle terminal allows 10% of the turns to be shorted. The winding fault machine specifications are listed in Table 4-1. To measure the machine parameters, different experiments such as a DC test, no-load test, blocked-rotor test and run-down test have been conducted on this machine [83], the machine parameters calculated from those tests are shown in Table 4-2.

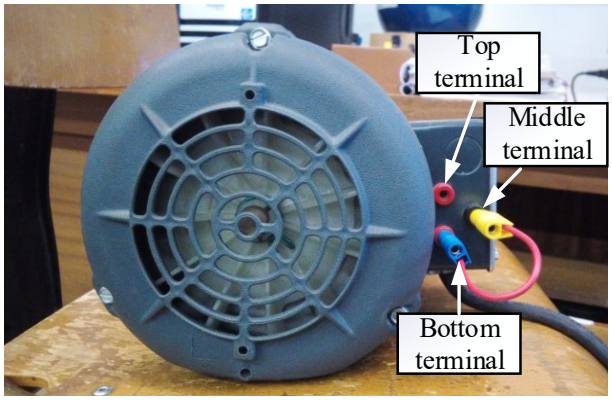

Fig. 4-8 Stator winding fault induction machine.

TABLE 4-1 Researched Induction Machine Specifications

Parameter	Value
Rated voltage	190V
Rated current	1.85A
Connection	Wye
Frequency	50Hz
Speed at rated power	2850rpm
Rated power	248.57W
Number of phases	3
VA Ratings	608.82VA
Slip at the rated power	5%
Rated torque	0.8329Nm

TABLE 4-2 Measured Machine Parameters under Healthy Conditions

Parameter	Value
Stator resistance Rs	4.24 Ω
Rotor resistance Rr	2.12 Ω
Magnetizing reactance Xm	76.27 Ω
Stator leakage reactance Xls	3.95 Ω
Rotor leakage reactance Xlr	3.95 Ω
Moment of inertia J	0.0016797 $kg.m^2$
Friction coefficient B	0.0010356 N.m.sec

4.4.1 Simulation Results

The mathematical model established in Chapter 4.2 is used to create a Matlab/Simulink model with the machine parameters shown above.

The transient and steady-state performance of the healthy machine and faulted machine with 5% and 10% shorted-turns, are investigated. The simulation results of the 5% short-turns fault are shown in Fig. 4-9. Fig. 4-9 (a) is the response of stator current from direct online start-up to steady-state. Fig. 4-9 (b) is the steady-state current, it can be observed that the stator current amplitude of one phase is much lower than the other two phases, when there is an inter-turn fault. This is because the shorted turns in the winding will draw a large circulating current and generate excessive heat.

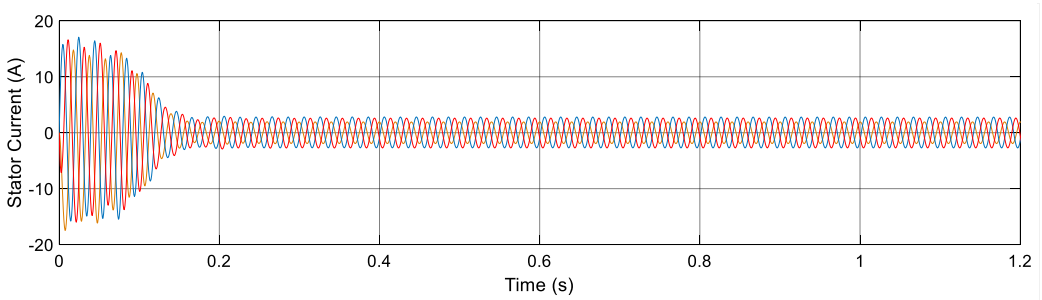

(a)

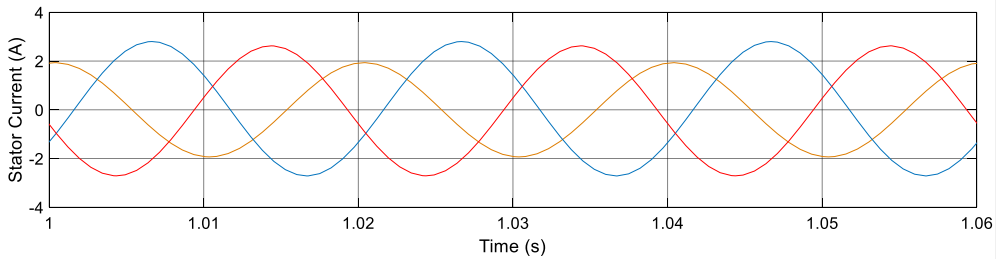

(b)

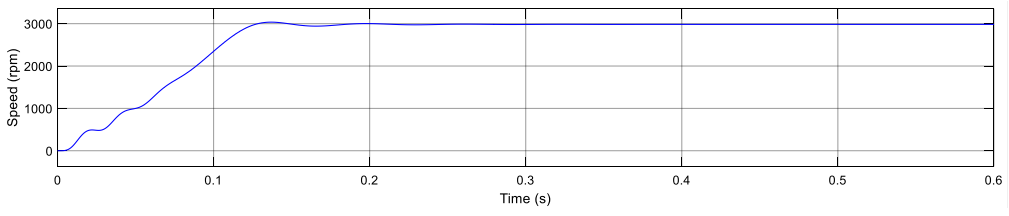

(c)

Fig. 4-9 Simulation results of 5% shorted turns: (a) stator current direct online startup, (b) zoomed view, (c) speed.

Fig. 4-10 shows the simulation results of 10% shorted turns. Fig. 4-10 (a) is the stator current response of direct online start-up to steady-state. Fig. 4-10 (b) zooms into the steady-state current and in comparison with Fig.4-9 (b), it can be seen that the stator current amplitude increases significantly than 5% shorted-turns.

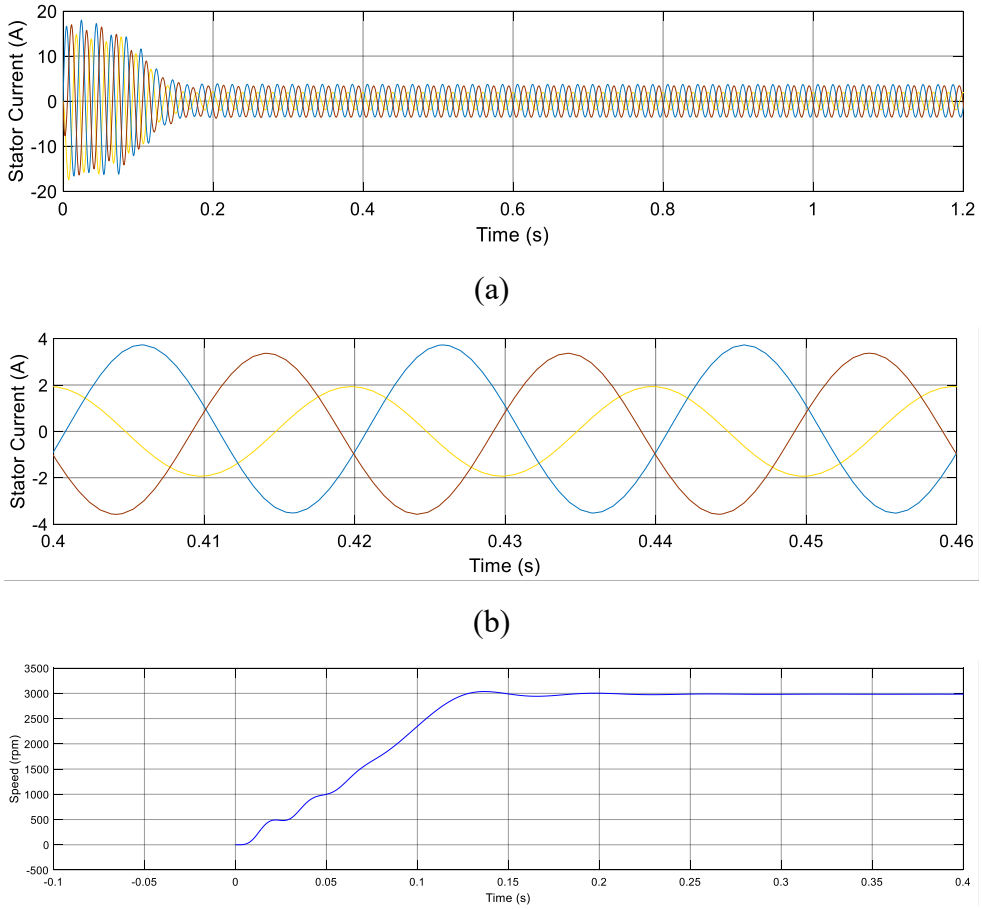

Fig. 4-10 Simulation results of 10% shorted turns: (a) stator current direct online startup, (b) zoomed view, (c) speed.

4.4.2 Experimental Results

Fig. 4-11 shows the experimental setup for testing the machine. The induction machine under test is coupled to an ECMA-C11010ES 1kW AC servo motor, which loads the induction machine. The rated torque of the servo motor is 3.18 N.m, thus, the setup is able to test load conditions.

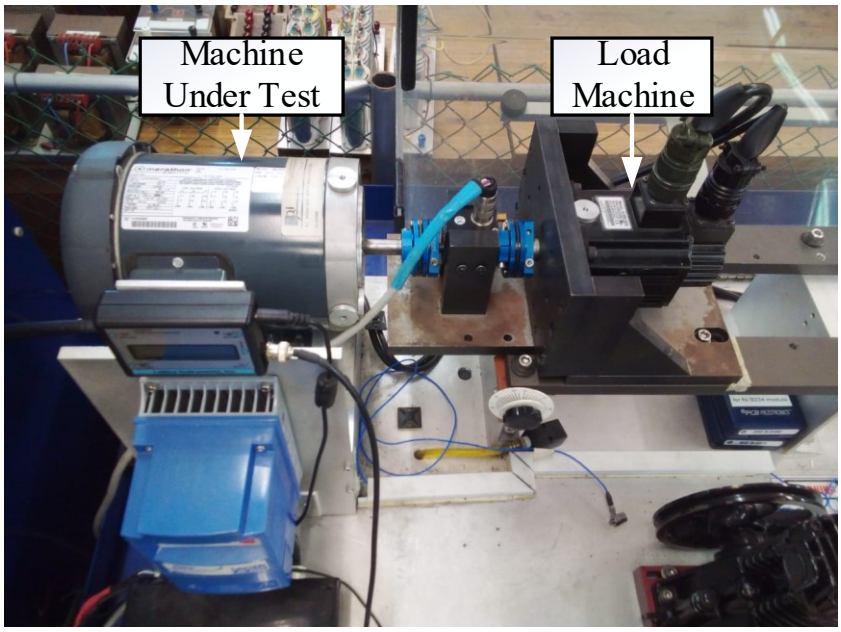

Fig. 4-11 Experimental set up for the actual machine.

Fig. 4-12 (a) shows experimental results of stator current when the actual machine operates from direct online startup to the steady-state with 5% shorted turns. Comparing with Fig. 4-12 (b), the emulation results of the transient direct online startup have a similar response and same time constant in reaching steady-state. Fig. 4-12 (c) shows the waveform of actual results and emulation results at steady-state. It can be seen that the emulation results match well with the actual machine under steady-state conditions. The speed of direct online startup with the 5% shorted turns is shown in Fig. 4-12 (d), where the speed from emulation is compared with the actual motor.

The full load torque of the faulted machine is 1.03 N.m. As shown in Fig. 4-11 the induction machine is coupled with a servo motor for mechanical input. Fig. 4-13 is the comparison of 5% shorted turns with loading condition, which is approximately 5% of servo motor rated torque. By comparison of the actual machine results with the emulation results, it can be observed that the built emulator works well with the loading condition. Fig. 4-14 shows the results with another load torque condition, which is 10% of servo motor rated torque. The emulation results of Fig. 4-14 (b) match with the actual machine results shown in Fig. 4-14 (a). Also, from the 5% loading, as shown in Fig. 4-13 and 10% loading in Fig. 4-14, it can be seen that the stator current with 10% load torque has a significant increase compared to 5% load torque.

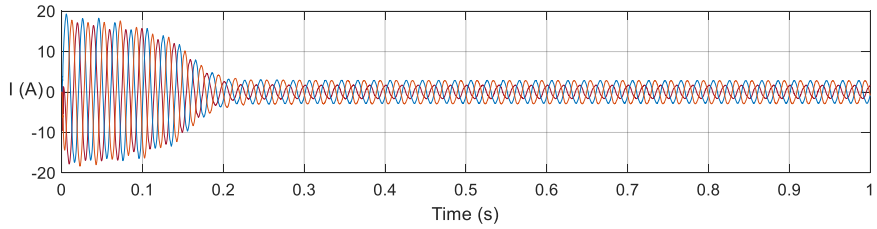

(a)

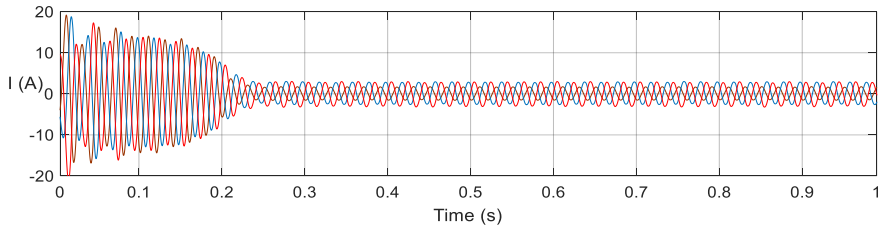

(b)

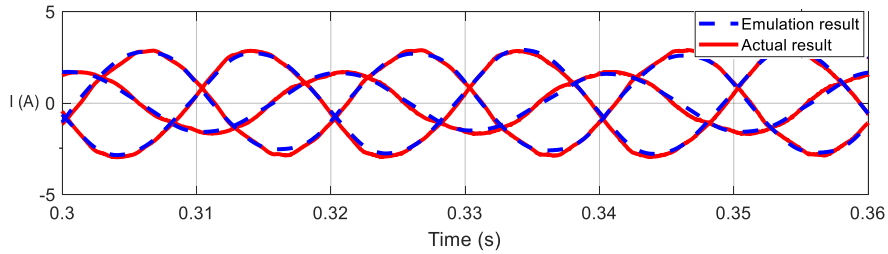

(c)

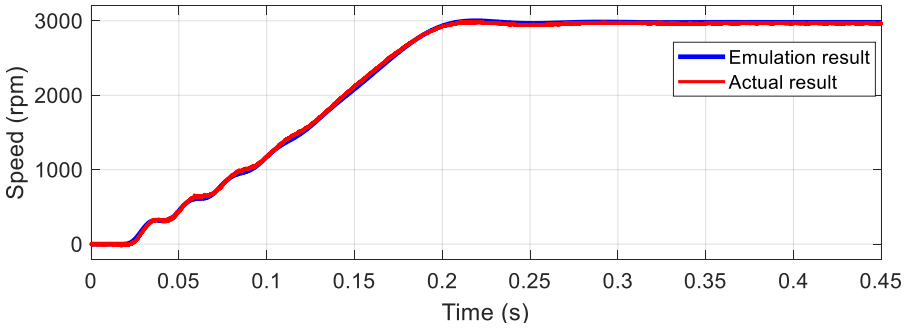

(d)

Fig. 4-12 Direct online startup with 5% shorted turns: (a) actual machine, (b) emulation, (c) overlap waveform at steady state, (d) speed during direct online start-up.

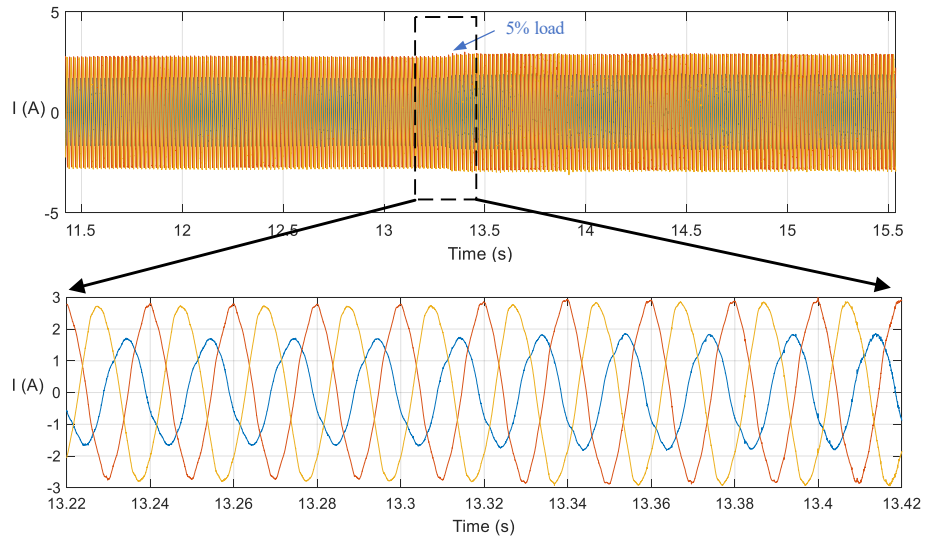

(a)

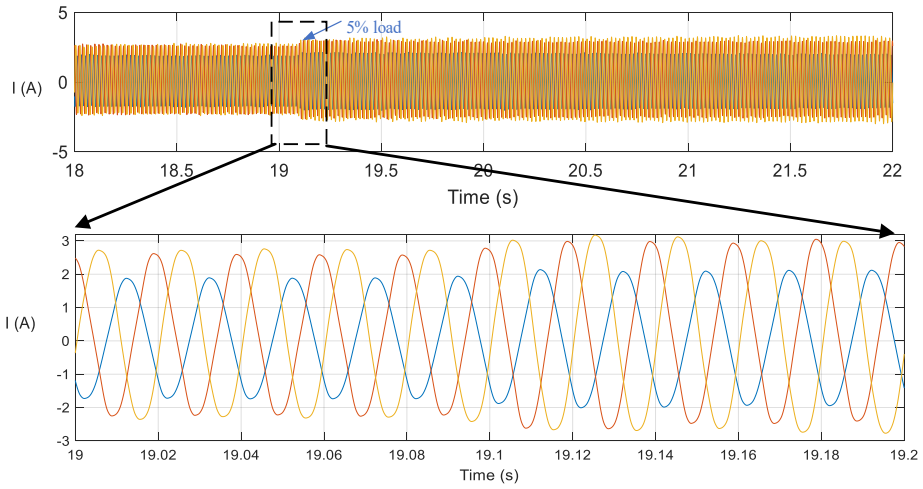

(b)

Fig. 4-13 Experiment results with 5% shorted turn and 5% loading: (a) actual machine, (b) emulation.

Fig. 4-15 shows the results with 10% shorted turns. Fig. 4-15 (a) shows the results of the actual machine with direct online startup to steady-state and Fig. 4-15 (b) is the corresponding emulation results. It can be seen that the emulation results track the actual results. They take similar times to reach steady state. Fig. 4-15 (c) shows the waveforms from the actual machine and emulator at steady state, which demonstrates a good agreement between them. Comparing the actual machine experimental results Fig. 4-15 (a) with Fig. 4-12 (a) 5% shorted turns, it can be concluded that 10% shorted turns lead to more severe conditions, the magnitude of stator current

increased significantly. The speed of direct online startup with the 10% shorted turns is shown in Fig. 4-15 (d), where the results of emulation are compared with the actual motor.

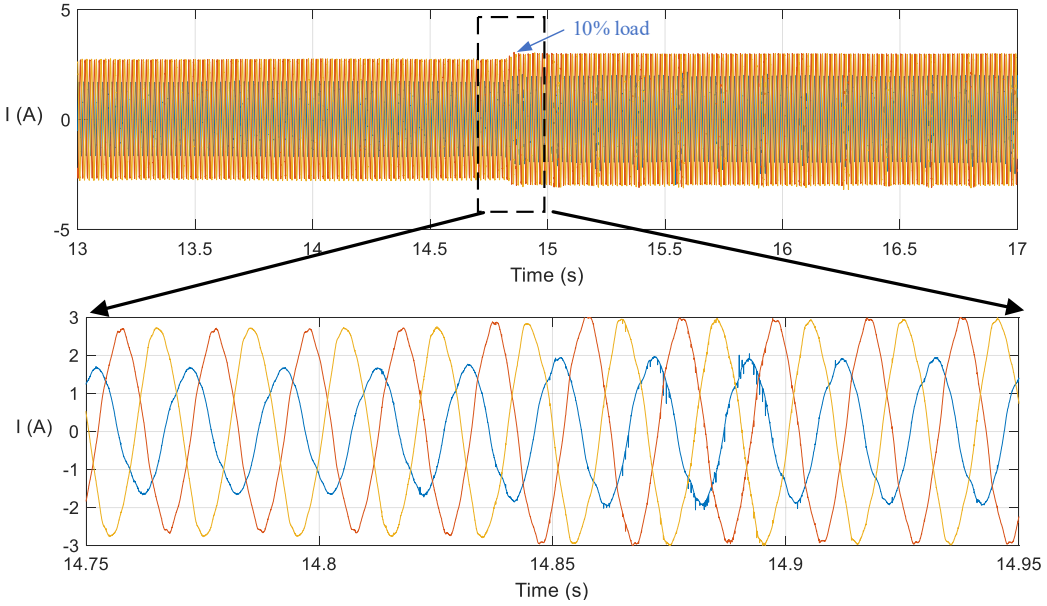

(a)

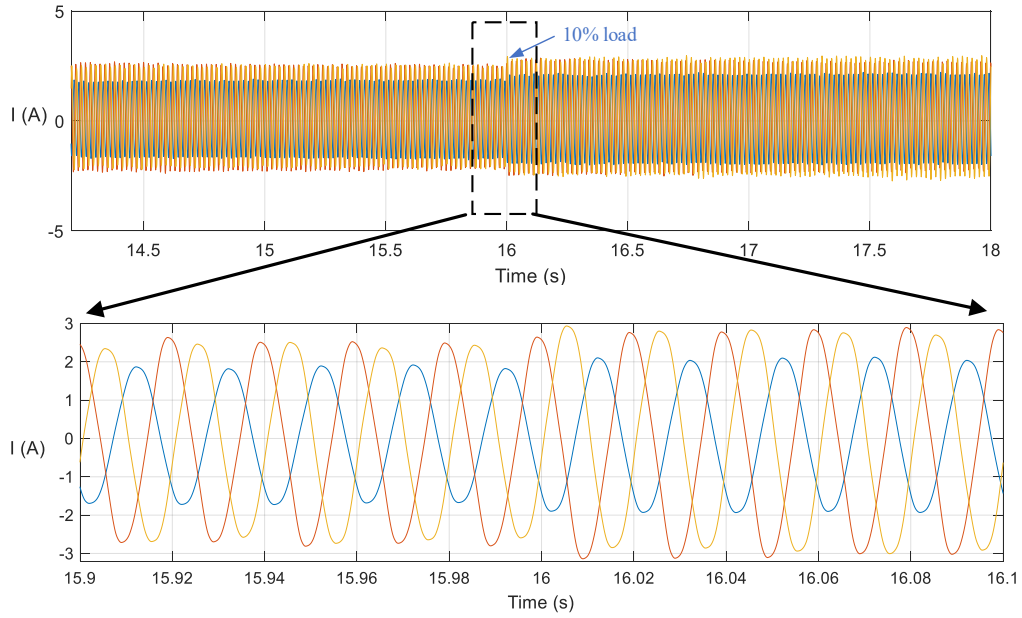

(b)

Fig. 4-14 Experiment results with 5% shorted turn and 10% loading: (a) actual machine, (b) emulation.

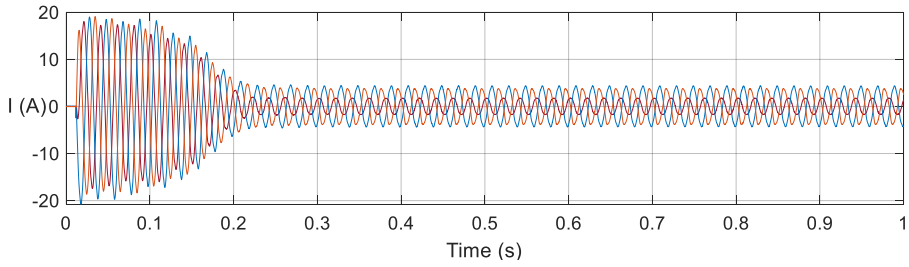

(a)

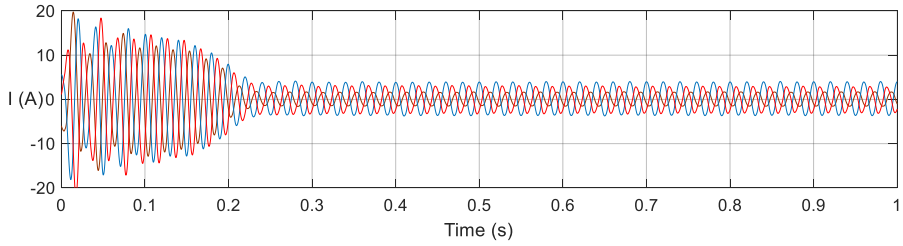

(b)

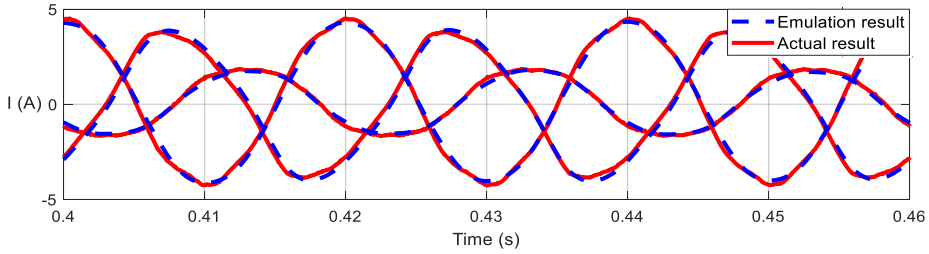

(c)

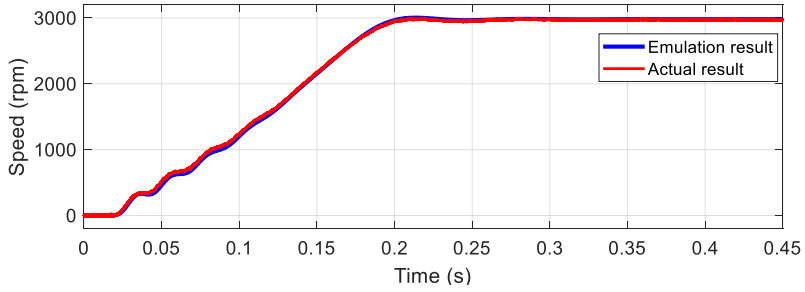

(d)

Fig. 4-15 Direct online startup with 10% shorted turns: (a) actual machine results, (b) emulation results, (c) overlap waveform at steady state, (d) speed during direct online start-up.

From the current waveforms in Figs. 4-12 and 4-15, it can be observed that during 5% and 10% short-turn faults, the current amplitudes of two phases are higher than the other phase, and the amplitude increase in two phases are higher at 10% than at 5% shorted turn. This is due to the line voltages remaining the same with $V_{ab} = V_{bc} = V_{ca}$. When the fault happens in phase a, the total

impedance Z_s will reduce, which will cause the line currents i_{as} and i_{cs} to increase in terms of $i_{as} = \frac{V_{ab}}{Z_s+(1-\beta)Z_s}$, and $i_{cs} = \frac{V_{ca}}{Z_s+(1-\beta)Z_s}$, whereas the current i_{bs} remains unchanged at $i_{bs} = \frac{V_{bc}}{2Z_s}$.

Fig. 4-16 compares the loading condition at 10% shorted turns with 5% load torque. The emulation results respond well compared with actual machine results. The results of 10% shorted turns with 10% load torque is not acquired due to the actual machine is not able to work normally in such condition, the machine starts to vibrate, the stator current start to surge.

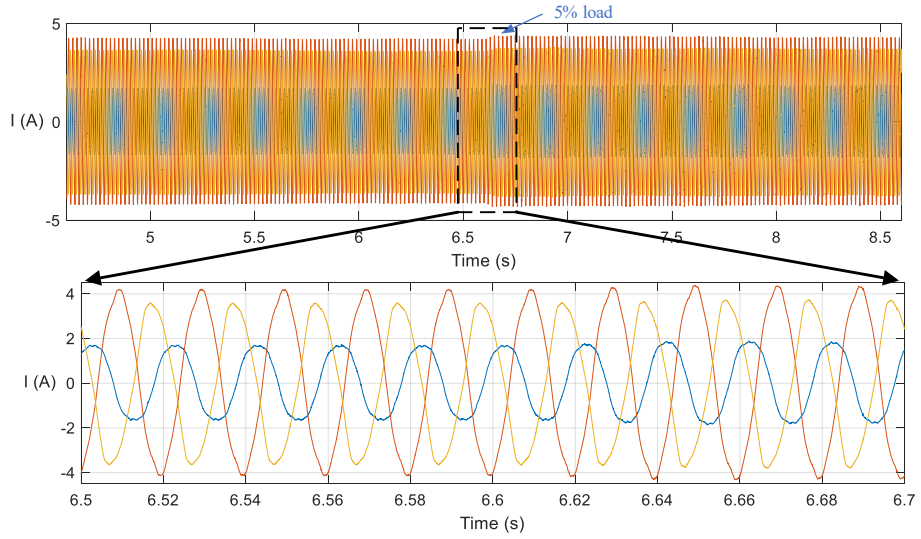

(a)

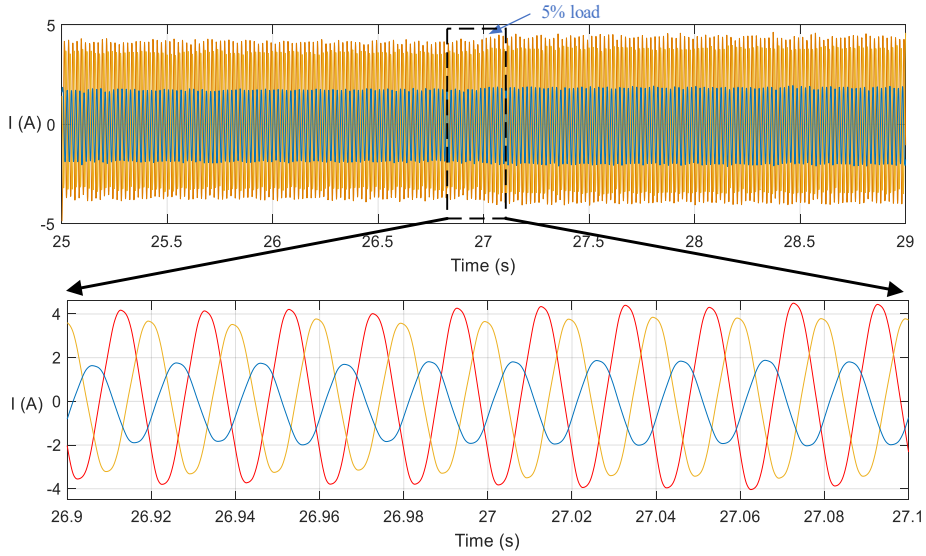

(b)

Fig. 4-16 Experiment results with 10% shorted turn and 5% loading: (a) actual machine, (b) emulation.

4.5 Summary

This Chapter proposed an IM emulator, which is able to emulate an IM with stator winding faults. The machine model of a healthy machine is introduced first. Then the machine model with stator winding faults was derived. The experiment to test the actual machine was introduced. The simulation results are shown to validate the ability of the built mathematical model. The experimental setup of the built emulator was also shown and the control methods were explained. The experiments were conducted on the actual machine with 5% and 10% shorted turns with two different load torques in each case. The emulation is also carried out for the same cases to validate the built IM emulator. The comparison of emulation machine results with actual machine results shows a good agreement, which proved the ability of the built emulator to be used to investigate faulted machines in the laboratory.

Chapter 5.
Induction Machine Emulation with Rotor Cage Faults

5.1 Introduction

The rotor of induction machine can have internal faults in motoring and generating modes. Some of the rotor faults include, broken rotor bars, end ring connectors, eccentricities, and are often a result of a poor working environment and installation. Since the induction machine is a high-order, nonlinear, and strongly coupled multivariable system, once a fault happens, the mathematical machine model will be significantly different from that under symmetrical normal operating conditions. Furthermore, the machine model during faults is significantly more complicated due to its asymmetrical nature. This chapter focuses on the investigation of mathematical models of induction machines with cage faults, specifically broken rotor bar fault.

The squirrel cage of an induction machine is shown in Figure 5-1. This squirrel cage rotor structure consists of rotor bars short circuited by end rings on both sides of the bars. Therefore, each squirrel cage rotor of each machine, consists of N_r bars and two end rings connecting the bars on either ends.

For such a structure, the most causes of fault conditions are:

i) Shrink holes and voids in the aluminum of the rotor bars or end rings,

ii) Unstable junctions between the bars and end rings,

iii) Heavy duty start-ups that are over the machine rated operating conditions,

iv) Thermal overloading,

v) Mechanical stresses,

The consequences of rotor faults due to the above reason, will lead to machine speed fluctuation, torque pulsation, multiple frequency components of the stator current, temperature increase, arcing in the rotor, and machine oscillations.

Many methods have focused on modeling squirrel cage induction machines with rotor asymmetries [84]-[86]. To build the mathematical model of induction machine, multiple coupled circuit models [87], [88] and dq frame models are commonly applied. There are also research on parameters estimation under faulty conditions through healthy machine model [89], [90] .

Fig. 5-1 Rotor cage of an induction machine.[25]

For a rotor cage fault modification can be made to the model of a healthy squirrel cage rotor as shown in Fig. 5-2. The rotor cage is described as n rotor circuit loops that are identical and equally spaced. The first loop include the 1st and $(k+1)^{th}$ rotor bars and a part of the end ring connecting them, where $k \in \{1,2,\ldots, n\}$. Similarly, the second loop consists of the 2nd and $(k+2)^{th}$ rotor bars and a part of the end ring connecting them, and so on.

If the cage has n bars, then there are $2n$ nodes and $3n$ branches. Therefore, the total current in the cage circuit can be expressed as $n+1$ independent rotor currents. Among those $n+1$ rotor currents, there are n rotor loop currents i_n^r, and one circulating current i_e, in one of the end rings. It is obvious

that i_e would be zero in a healthy machine. The remaining n rotor loop currents are coupled with each other and stator windings, through the mutual inductances. For the end ring loop current, it only couples with the rotor loop currents through the end ring leakage inductance and the end ring resistance.

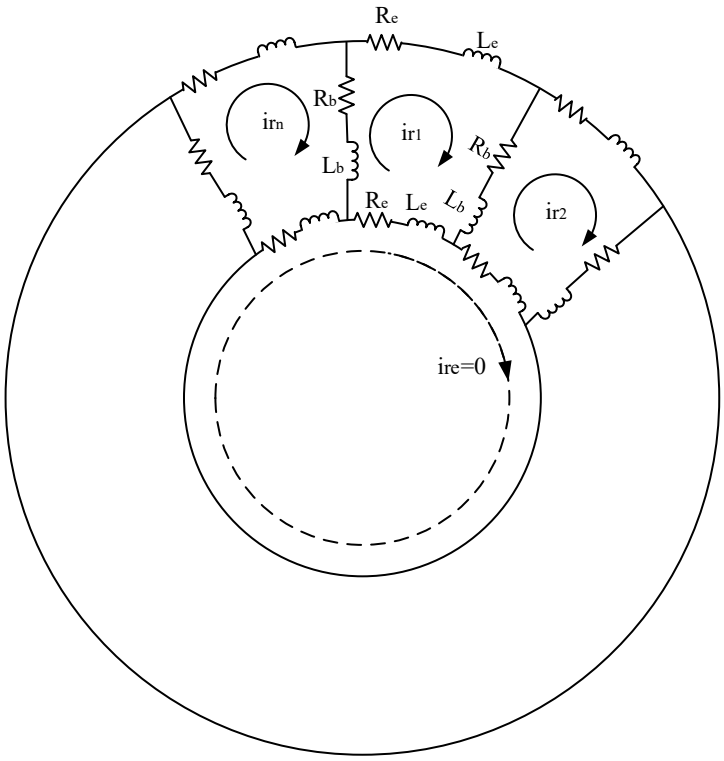

Fig. 5-2 Equivalent circuit of squirrel cage rotor.[31]

In Fig. 5-2, L_b is the rotor bar leakage inductance, $R_b$is the rotor bar resistance, L_e is the rotor end ring leakage inductance, R_e is the end ring segment resistance.

To analyze fault conditions, the rotor equivalent circuit can be opened and shown as in Fig. 5-3, where three different conditions of rotor cage are shown. When the cage is at a normal condition as shown in (a), the rotor resistance and the mutual inductance equations can be obtained from the equivalent circuit. Fig. 5-3 (b) and (c) is the circuit when the rotor bar broken and the end ring segment broken. It can be seen that if the rotor bar n or end ring segment n is broken, all parameters related to the loop n must change. Thus, the mathematical model under cage fault can be obtained accurately.

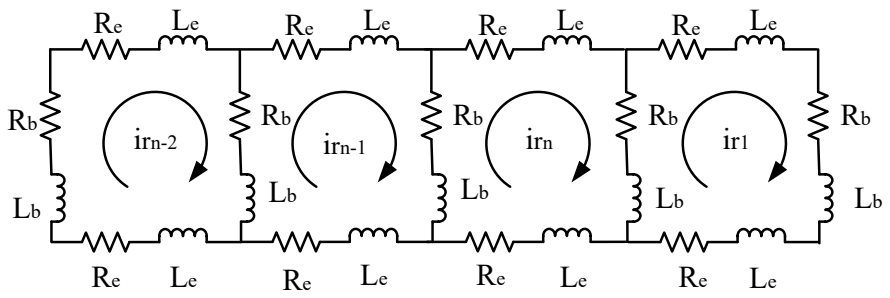

(a)

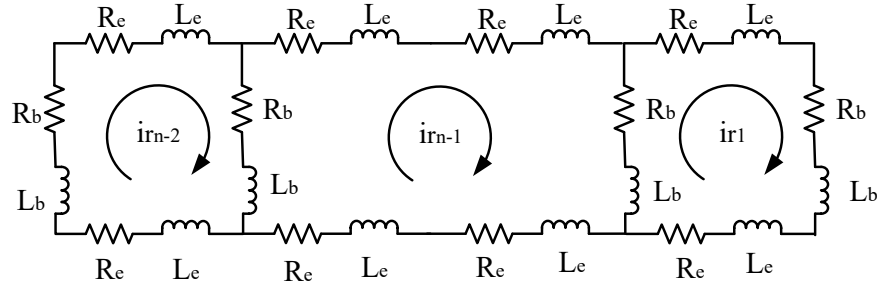

(b)

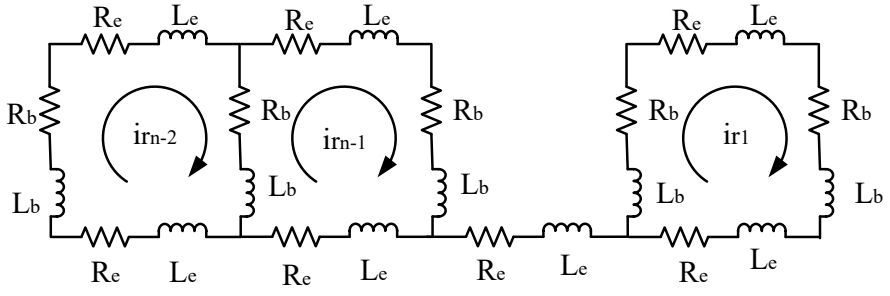

(c)

Fig. 5-3 Fault conditions of rotor. (a) Normal condition, (b) last bar broken, (c) last end ring segment broken. [30]

5.2 Cage Fault Machine Parameters Measurement

For a machine with broken rotor bars, some of the motor parameters are no longer constant. The broken rotor bars will cause an asymmetrical magnetic field, which will also cause parameters such as rotor resistance, rotor leakage inductance and the mutual inductance to change in a result

of asymmetry. Conventional measurement techniques are no longer usable in such conditions, since it only gives parameters for symmetrical conditions.

In this Chapter, a parameter extraction method for a machine with rotor cage fault is applied. Firstly, the terminals of the stator are connected as shown in Fig. 5-4. In such conditions, the stator is supplied with only a single-phase voltage, then the parameters related to the rotor can be measured at different rotor angles [91].

The no-load and blocked-rotor tests are distinguished by the different voltage frequencies. The no-load test is to achieve the zero slip between the rotor rotating speed and the synchronous speed of the magnetic field. In such cases, the slip s will be close to zero. Here, for faulted machine as connected in Fig. 5-4, if the supply voltage is a very low frequency with a standstill rotor, the rotor slip will approach zero. Thus, the no-load test is applied.

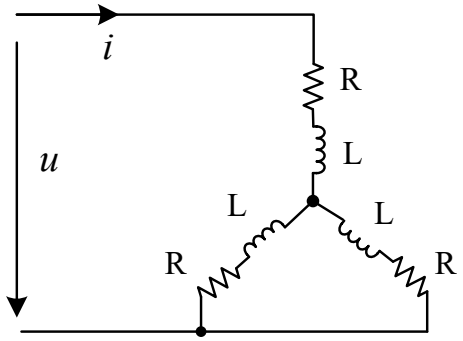

Fig. 5-4 Parameters measurement for cage fault machine

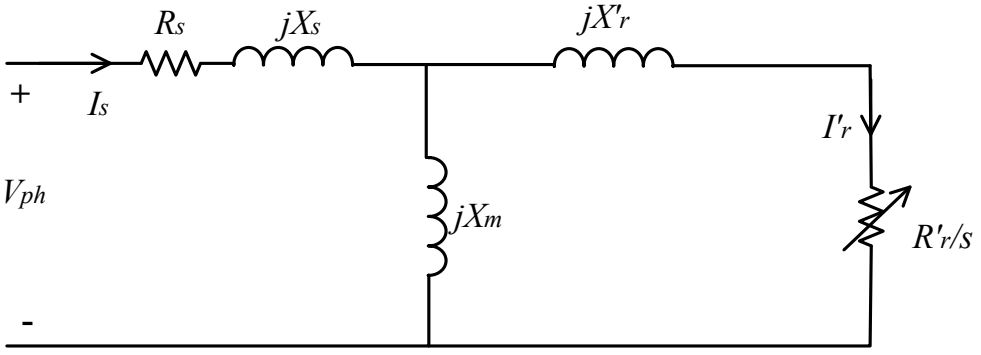

Fig. 5-5 Induction machine equivalent circuit.

The induction machine equivalent circuit is shown in Fig. 5-5. For the blocked-rotor test, since the rotor is already at standstill, then supplying the stator with a much higher voltage frequency, most of the current flows through the rotor circuit, due to the relative huge value of

mutual reactance *Xm*. Thus, the locked-rotor measurement is achieved. The no-load and blocked-rotor tests are taken with one-phase voltage at different supply frequencies.

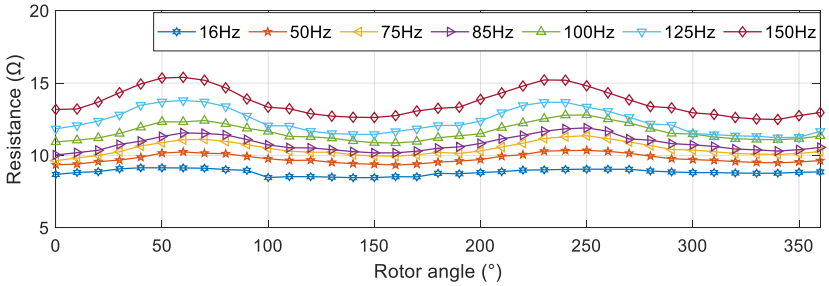

(a)

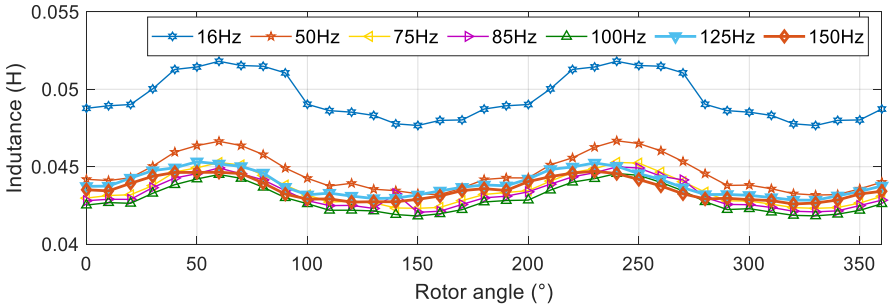

(b)

Fig. 5-6 Results of SCIM with broken rotor bars at different rotor angles: (a) Resistance response, (b) inductance response.

The measurement results of the squirrel cage induction machine (SCIM) with broken rotor bars are shown in Fig. 5-6, the measurement results are listed in Appendix - A. Fig. 5-6 (a) is the resistance response of the SCIM under different rotor angles. It can be seen that the resistance under low frequency is almost a straight line, which means the resistance is not affected by the broken rotor bars ($R=R_s$). Comparing the resistance at high frequencies, the value increases significantly and also starts to vibrate with different rotor angles, showing the effect from the broken rotor bars ($R=R_s+R_r$).

Similarly, it can be observed from Fig. 5-6 (b), the inductance magnitudes are significantly larger at low frequency, this is due to the mutual inductance ($L=L_{ls}+L_m$). The inductance at 125Hz and 150Hz are highlighted, it can be observed that the sinusoidal fluctuation reduces as frequency increases, but the sinusoidal variation can still be observed due to the rotor leakage inductance ($L=L_{ls}+L_{lr}$). From Figs. 5-6 (a) and (b), it can be concluded that

by using the method in Fig. 5-4, the low frequency measurement can be used to represent the no-load test and the high frequency measurement can be used to represent the blocked-rotor test.

5.3 Control of Emulation System

5.3.1 AFEC Converter

The control diagram for AFEC is shown as Fig. 5-7. The reference signal v_{dc}^* is compared with the measured DC link voltage v_{dc}, which obtains the d-axis reference current i_d^* through a proportional-integral (PI) regulator. The ac side currents are transformed into dq reference frame components as i_d and i_q. The references i_d^* and i_q^* are compared with the measured actual currents i_d and i_q, respectively. Then the PI regulator generates the voltage references, which are transferred from dq to abc reference frame, and then sent to the modulator to produce gate signals.

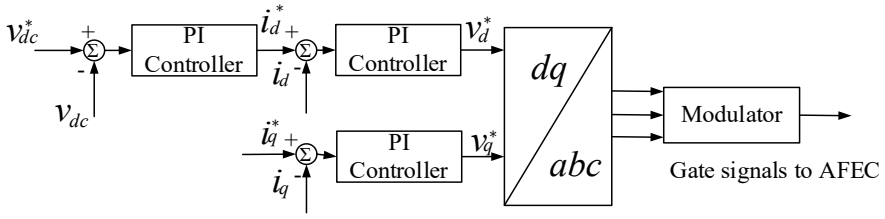

Fig. 5-7 Control diagram for AFEC

5.3.2 Emulator Converter

The control diagram for the emulator converter is shown in Fig. 5-8. A proportional-resonant (PR) current controller is used to control the emulator converter, the output of the controller is used by the modulator to generate gate signals. The PR controller is able to eliminate the steady-state error and its frequency is maintained constant, which is suitable for a high power rectifier.

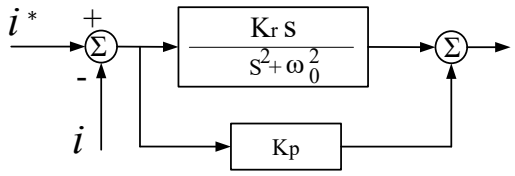

Fig. 5-8 Control diagram for emulator converter

5.4 Simulation and Experimental Results

The stator current spectral components can be used to detect and identify the rotor cage fault condition [92]. The cage fault will increase the frequency components in the stator current at $f_s(1 \pm 2s)$, where f_s is the stator current fundamental frequency and s is the slip between rotor and synchronous magnetic fields. The FFT analysis of a healthy machine stator current is shown in Fig. 5-9 (a) and cage fault machine in Fig. 5-9 (b). It can be observed that the amplitude of frequency components increases at around 48Hz and 52 Hz in Fig. 5-9 (b) comparing with Fig. 5-9 (a). Thus, the cage fault condition is identified.

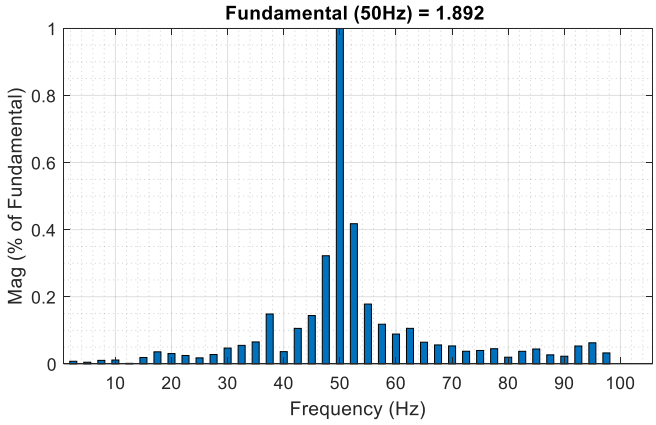

(a)

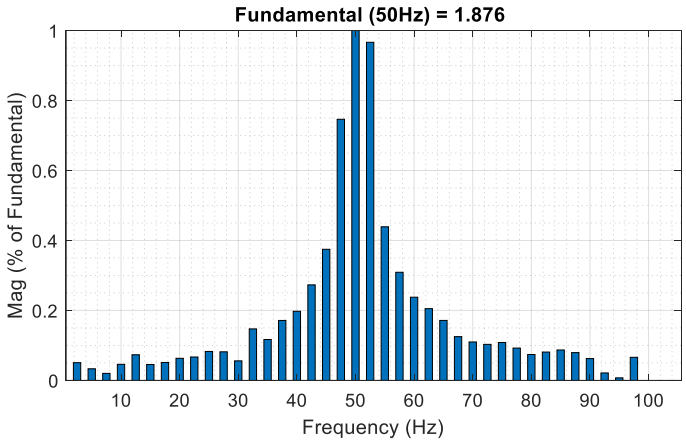

(b)

Fig. 5-9 Stator current FFT analysis of: (a) healthy machine, (b) cage fault machine.

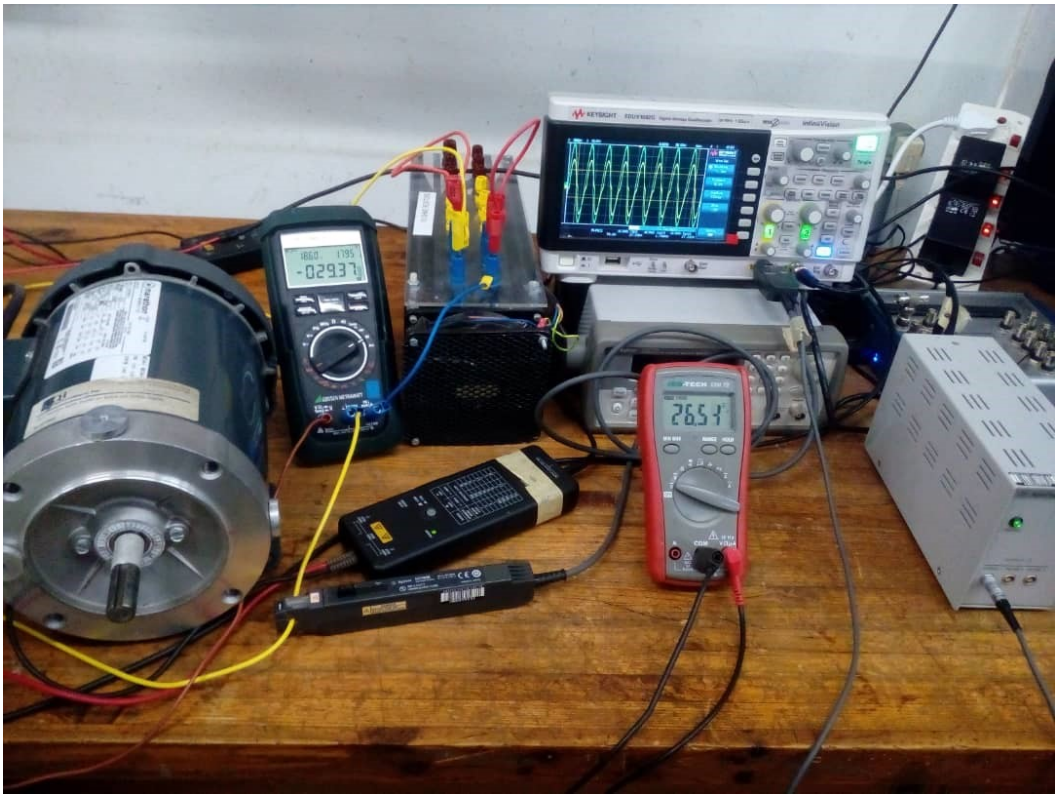

Fig. 5-10 Experimental setup for machine parameters measurement.

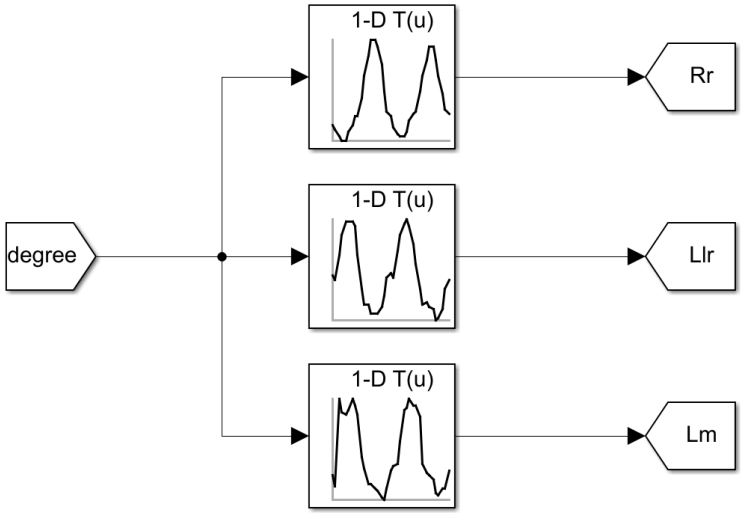

Fig. 5-11 1-D lookup table-based machine model.

The experimental setup for machine parameters measurement is shown in Fig. 5-10. The rotor cage fault machine is supplied with a single-phase voltage at different frequencies. The

single-phase voltage, current and actual power are measured at different rotor angles, such that the machine parameters can be separated by the different frequencies. Furthermore, the measured parameters vary with the rotor angle. Thus, to build the mathematical model of machine, three 1-D lookup tables have been used as shown in Fig. 5-11. From Fig. 5-11 it can be observed that the parameters, which are affected by broken rotor bar, such as rotor resistance, rotor leakage inductance, and mutual inductance are varied based on the different rotor angles.

Fig. 5-12 (a) is the actual machine stator current at steady-state with rotor cage fault, it can be observed that the stator current is asymmetrical due to the faulted condition. Fig. 5-12 (b) is the model based simulation results, where the machine parameters are extracted from same machine. Fig. 5-12(c) is the overlap waveform of actual results and emulation results. The comparison of loading condition is shown in Fig. 5-13, which 10% of rated load is applied. Fig.5-13 (a) is the results of actual machine and Fig. 5-13 (b) is the emulation results. The results show a good agreement between simulation, emulation with actual machine.

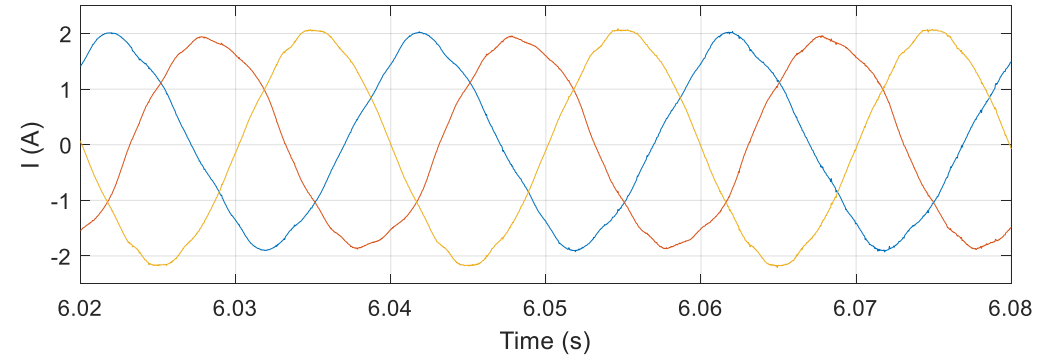

(a)

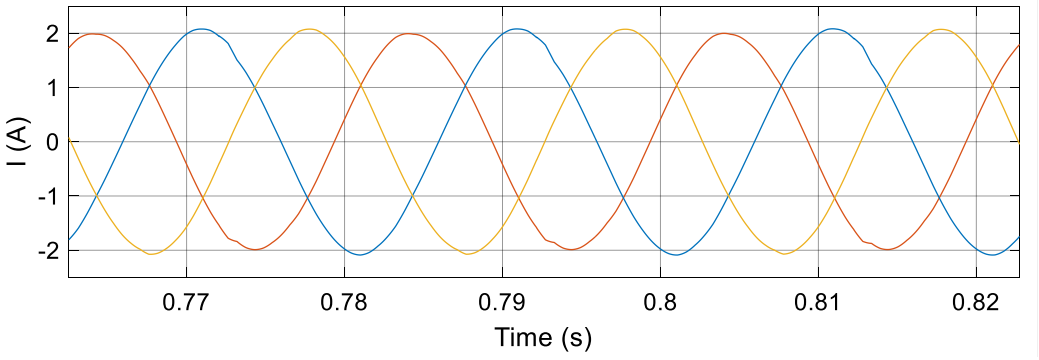

(b)

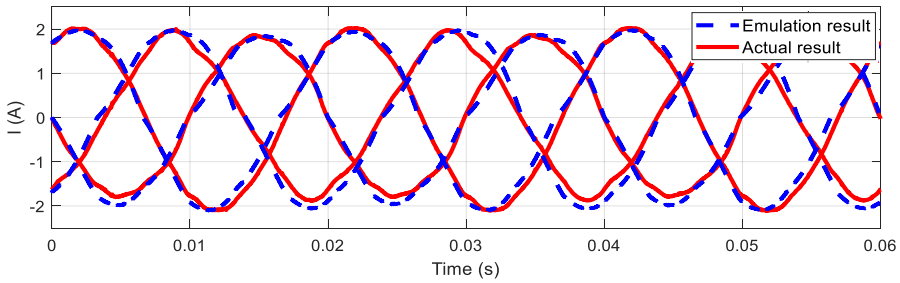

(c)

Fig. 5-12 Stator current at steady state: (a) actual rotor cage fault machine, (b) simulation result, (c) overlap waveform.

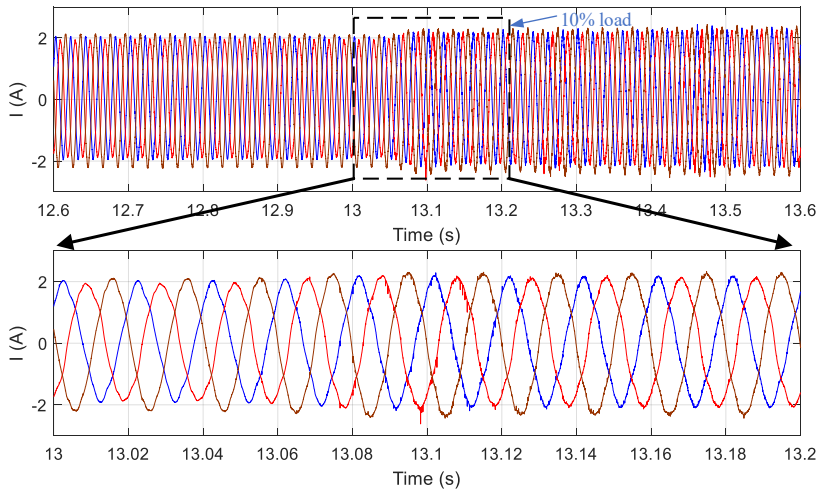

(a)

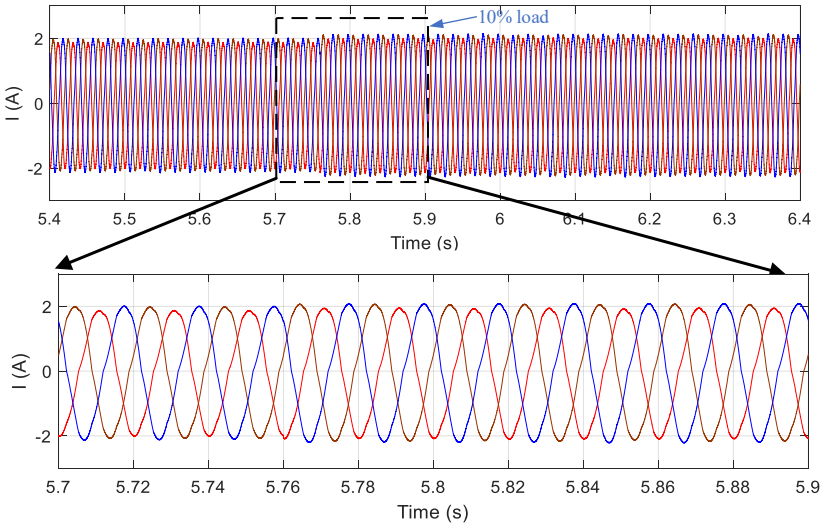

(b)

Fig. 5-13 Loading condition: (a) actual machine, (b) emulation result.

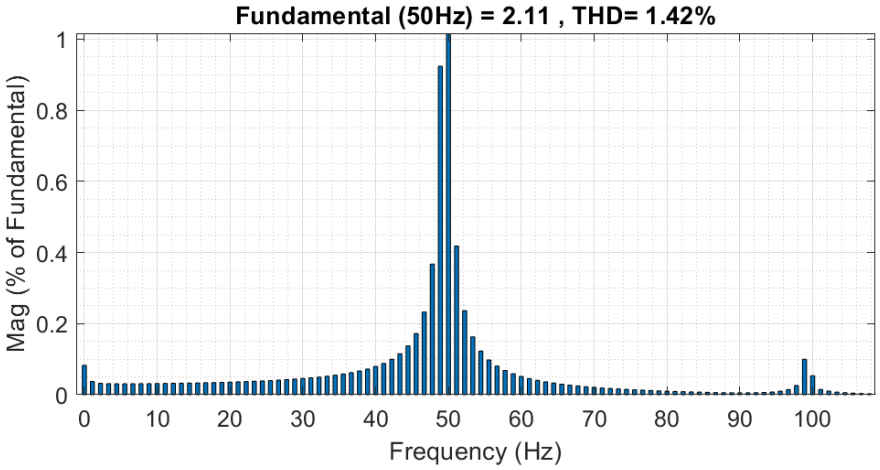

Fig. 5-14 FFT analysis of model-based phase A stator current.

Fig. 5-14 shows the FFT analysis of model-based phase A stator current. It can be observed that the two side-band harmonics of the fundamental component increase significantly, which is similar to the actual rotor cage fault machine as shown in Fig. 5-9.

5.4 Summary

This chapter has proposed an IM emulator, which is able to emulate an IM with rotor cage faults. The experimental methods to extract machine parameters was introduced. The simulation results are shown to validate the ability of the built mathematical model. A comparison of the experimental results with model-based simulation results and emulation results demonstrate the validity of the developed mathematical machine model for the IM emulator, providing an accurate solution for investigating IM fault conditions in the laboratory environment.

Chapter 6.
Conclusions and Future Work

This Ph.D. work is devoted to

- Investigating the asymmetrical conditions in the induction machine, developing the corresponding mathematical machine model and the applications of the faulted machine model for emulation. Due to the characteristics of high-order, nonlinear, asymmetrical conditions, and strongly coupled multivariable systems of induction machines, once the fault happens, the mathematical model of machine will be significantly different and become more complicated. The faulted condition is an abnormal operating condition. Continuing to drive the machine can damage it, with safety issues at high speed. In this Ph.D. research work, the induction generator with unbalanced loads, nonlinear loads and induction motor with stator winding faults, rotor cage faults were emulated.
- Secondly, developing a power electronic converter-based machine emulation setup. The built testbed is able to replace an actual faulted induction machine that works either with a stator winding fault or rotor cage fault conditions. Thus, it can be used to develop and test the corresponding machine drive technique without actual damage to the machine. Therefore the risk and cost associated with testing, and analysis of faulted machines are reduced.

6.1 Conclusion

Chapter 1 reviewed induction machines under asymmetrical conditions and machine emulation.

- According to research, the most common asymmetrical operation occurs due to the unbalanced loads for induction generators and failures in stator windings, and the rotor cage of induction motors. The asymmetrical operation of the induction machine can cause low efficiency and excessive heating, and lead to failure of the machine.
- The electrical machine emulator is proposed to replace expensive test benches and equipment as well as the risks associated with the development and testing of new drive systems. With the emulator, various types of electric machines with different power ratings or conventional and advanced control strategies can be tested. Especially for the research of asymmetrical conditions, the application of an emulator can prevent the consequence of failure due to the fault inside the machine and can be used to develop the corresponding control method.

Chapter 2 introduced the induction machine mathematical model in healthy conditions, which is the foundation to research the asymmetrical operating conditions.

- The mathematical model is first introduced in the *abc* reference frame, and then by applying Park's transformation, the machine model is transferred to *dq* reference frame so as to simplify the calculation during simulation.
- The machine parameter measurement method is also introduced, by DC test, the stator resistance is measured; from the blocked-rotor test and no-load test, the rotor resistance, mutual inductance, stator leakage inductance, rotor leakage inductance are verified.

In **Chapter 3,** the emulation of unbalanced and nonlinear loads in the induction generator was investigated.

- The mathematical model of an actual 5 hp induction machine was firstly established, then the mathematical model of excitation capacitor bank, loads as well as the inverter were established.
- The machine emulation testbed for the induction generator was built.
- The SEIG supplying balanced loads were firstly investigated, and the emulation results track the actual machine results, which verifies the accuracy of the built emulator. Then the unbalanced conditions were compared with the actual machine

and the performance of the emulator during transients was also shown. In the end, the emulated SEIG supplying nonlinear load conditions were presented.

Chapter 4 presented the emulation of an induction motor with stator winding fault conditions.

- The mathematical model of induction machine stator winding faults was firstly established in the *abc* reference frame, then the *dq* reference frame model was derived by applying Park's transformation.
- The induction motor emulation system was introduced, including hardware setup and controller design.
- The experimental results with an actual induction machine with two different levels of stator winding faults were shown and compared with simulation results first.
- The emulation results were compared with the actual machine in two different stator winding faults.
- The loading conditions were also considered. The emulation and actual machine with loading conditions were compared.

Chapter 5 presented the emulation of induction motor with rotor cage fault conditions.

- After the rotor cage fault occurred, the machine parameters related to the rotor cage will change according to the angle with three-phase stator windings. The cage fault machine parameters measurement method was introduced.
- The rotor cage fault condition was firstly identified by FFT analysis.
- The machine parameters of an actual induction motor with rotor cage faults were measured at different rotor angles.
- The simulation and emulation results were compared with the actual rotor cage fault induction motor.
- The loading conditions were also considered and emulation results were compared with the actual machine results.

6.2 Future Work

This thesis has shown the accuracy of emulation compared to the actual machines. The improvement and prospective research works are addressed as follows:

- For emulation of induction generator, the SEIG with nonlinear loads has only investigated the diode converter with DC loads. More research could be done with complicated loads to expand the application of the SEIG emulator, such as to research the power flow between the SEIG emulator with an actual battery, which will be useful to investigate the microgrid with generator, loads, and batteries.
- The emulation of induction motor with faults conditions, was only done with a grid supply. More research work could be done by applying drives to the emulation machine, which can be used to develop novel drive techniques for faulted machines.
- The development of an induction motor emulator can be tested with a machine with integrated faults, for example during the emulation, the emulated machine can switch between healthy, stator winding faults or rotor cage fault conditions, thus to test the performance of the drive inverter under severe conditions.

References

[1] S. -. Kuo and L. Wang, "Analysis of isolated self-excited induction generator feeding a rectifier load," in *IEE Proceedings - Generation, Transmission and Distribution*, vol. 149, no. 1, pp. 90-97, Jan. 2002.

[2] M. G. Simões and F. A. Farret, *Modeling and Analysis with Induction Generators.* 2014.

[3] K. R. R, K. Gopakumar, M. Boby, A. K. Yadav, L. G. Franquelo and S. S. Williamson, "Multilevel 24-Sided Polygonal Voltage-Space-Vector Structure Generation for an IM Drive Using a Single DC Source," in *IEEE Transactions on Industrial Electronics*, vol. 66, no. 2, pp. 1023-1031, Feb. 2019.

[4] M. Z. Lu, V. K. Ganisetti and C. M. Liaw, "Establishment and Dynamic Control of Wind Induction Generator," *2018 International Power Electronics Conference (IPEC-Niigata 2018 -ECCE Asia)*, Niigata, 2018, pp. 2907-2913.

[5] Y. Wang and N. Bianchi, "Modeling and Investigation of Self-Excited Reluctance Generators for Wind Applications," *2018 IEEE Energy Conversion Congress and Exposition (ECCE)*, Portland, OR, 2018, pp. 3331-3338.

[6] M. Ibrahim and P. Pillay, "The loss of self-excitation capability in stand-alone synchronous reluctance generators," *2017 IEEE Energy Conversion Congress and Exposition (ECCE)*, Cincinnati, OH, 2017, pp. 1857-1863.

[7] Z. Din, J. Zhang, J. Zhao and Y. Jiang, "Doubly Fed Induction Generator with Cascade Converter for Improving Dynamic Performances," *2018 IEEE Energy Conversion Congress and Exposition (ECCE)*, Portland, OR, 2018, pp. 2568-2575.

[8] J. Radosavljević, D. Klimenta and M. Jevtić, "Steady-state analysis of parallel-operated self-excited induction generators supplying an unbalanced load," *Journal of Electrical Engineering,* vol. 63, *(4),* pp. 213-223, 2012.

[9] O. Mohammed Elbabo Mohammed, W. Xu and Y. Liu, "Control Design of Standalone Brushless Doubly-Fed Induction Generator for Supplying Unbalanced Loads," *2018 IEEE Energy Conversion Congress and Exposition (ECCE)*, Portland, OR, 2018, pp. 7369-7374.

[10] M. Jannati *et al*, "Modeling of Balanced and Unbalanced Three-Phase Induction Motor under Balanced and Unbalanced Supply Based on Winding Function Method." *International Journal of Electrical & Computer Engineering (2088-8708),* vol. 5, *(4),* 2015.

[11] K. Idjdarene *et al*, "Performance of an isolated induction generator under unbalanced loads," *IEEE Trans. Energy Convers.,* vol. 25, no. 2, pp. 303-311, June 2010.

[12] X. Luo, Y. Liao, H. Toliyat, A. El-Antably and T. A. Lipo, "Multiple coupled circuit modeling of induction machines," *Conference Record of the 1993 IEEE Industry Applications Conference Twenty-Eighth IAS Annual Meeting*, Toronto, Ontario, Canada, 1993, pp. 203-210 vol.1.

[13] H. A. Toliyat and T. A. Lipo, "Transient analysis of cage induction machines under stator, rotor bar and end ring faults," in *IEEE Transactions on Energy Conversion*, vol. 10, no. 2, pp. 241-247, June 1995.

[14] S. Chen and R. Živanović, "Modelling and simulation of stator and rotor fault conditions in induction machines for testing fault diagnostic techniques," *European Transactions on Electrical Power,* vol. 20, *(5),* pp. 611-629, 2010.

[15] K. S. Amitkumar, R. Thike and P. Pillay, "Power-Hardware-in-the-Loop Based Emulation of a Variable Flux Machine," *2018 IEEE Energy Conversion Congress and Exposition (ECCE)*, Portland, OR, 2018, pp. 6454-6460.

[16] M. A. Masadeh, K. S. Amitkumar and P. Pillay, "Power Electronic Converter-Based Induction Motor Emulator Including Main and Leakage Flux Saturation," in *IEEE Transactions on Transportation Electrification*, vol. 4, no. 2, pp. 483-493, June 2018.

[17] M. A. Masadeh and P. Pillay, "Power electronic converter-based three-phase induction motor emulator," *2016 IEEE International Conference on Power Electronics, Drives and Energy Systems (PEDES)*, Trivandrum, 2016, pp. 1-5.

[18] K. S. Amitkumar and P. Pillay, "Power Hardware-in-the-Loop based Emulation of an Open-Winding Permanent Magnet Machine," *2020 IEEE Energy Conversion Congress and Exposition (ECCE)*, Detroit, MI, USA, 2020, pp. 6118-6124.

[19] J. Wang, Y. Ma, L. Yang, L. M. Tolbert and F. Wang, "Power converter-based three-phase induction motor load emulator," *2013 Twenty-Eighth Annual IEEE Applied Power Electronics Conference and Exposition (APEC)*, Long Beach, CA, 2013, pp. 3270-3274.

[20] H. J. Slater, D. J. Atkinson, and A. G. Jack, "Real-time emulation for power equipment development. ii. the virtual machine," *IEE Proceedings – Electric Power Applications*, vol. 145, no. 3, pp. 153–158, May 1998.

[21] A. Schmitt, J. Richter, M. Gommeringer, T. Wersal, and M. Braun, "A novel 100 kw power hardware-in-the-loop emulation test bench for permanent magnet synchronous machines with nonlinear magnetics," in *8th IET International Conference on Power Electronics, Machines and Drives (PEMD 2016)*, April 2016, pp. 1–6.

[22] O. Vodyakho, M. Steurer, C. S. Edrington, and F. Fleming, "An induction machine emulator for high-power applications utilizing advanced simulation tools with graphical user interfaces," *IEEE Transactions on Energy Conversion*, vol. 27, no. 1, pp. 160–172, March 2012.

[23] R. M. Kennel, T. Boller, and J. Holtz, "Replacement of electrical (load) drives by a hardware-in-the-loop system," in *International Aegean Conference on Electrical Machines and Power Electronics and Electromotion, Joint Conference*, Sept 2011, pp. 17–25.

[24] F. Alvarez-Gonzalez, A. Griffo, B. Sen and J. Wang, "Real-Time Hardware-in-the-Loop Simulation of Permanent-Magnet Synchronous Motor Drives Under Stator Faults," in *IEEE Transactions on Industrial Electronics*, vol. 64, no. 9, pp. 6960-6969, Sept. 2017.

[25] S. Xiumei, Z. Shifu, Z. Shengqiang and P. Xueming, "The Emulation of Flow Field in Nozzles based on FEM," *2008 International Conference on Apperceiving Computing and Intelligence Analysis*, Chengdu, China, 2008, pp. 114-116.

[26] G. Tanuku and P. Pillay, "Emulation of an Induction Machine for Unbalanced Grid Faults," in *IEEE Transactions on Industry Applications*, vol. 57, no. 5, pp. 4625-4635, Sept.-Oct. 2021.

[27] K. S. Amitkumar, R. Thike and P. Pillay, "Linear Amplifier-Based Power-Hardware-in-the-Loop Emulation of a Variable Flux Machine," in *IEEE Transactions on Industry Applications*, vol. 55, no. 5, pp. 4624-4632, Sept.-Oct. 2019.

[28] H. A. Toliyat, T. A. Lipo and J. C. White, "Analysis of a concentrated winding induction machine for adjustable speed drive applications. I. Motor analysis," in *IEEE Transactions on Energy Conversion*, vol. 6, no. 4, pp. 679-683, Dec. 1991.

[29] F. Pedrayes, C. H. Rojas, M. F. Cabanas, M. G. Melero, G. A. Orcajo and J. M. Cano, "Application of a Dynamic Model based on a Network of Magnetically Coupled Reluctances to Rotor Fault Diagnosis in Induction Motors," *2007 IEEE International Symposium on Diagnostics for Electric Machines, Power Electronics and Drives*, Cracow, Poland, 2007, pp. 241-246.

[30] T. Omar, N. Lahcene, I. Rachild and F. Maurice, "Modeling of the induction machine for the diagnosis of rotor defects. Part I. An approach of magnetically coupled multiple circuits," *31st Annual Conference of IEEE Industrial Electronics Society, 2005. IECON 2005.*, Raleigh, NC, USA, 2005, pp. 8 pp.-.

[31] O. Touhami, L. Noureddine, R. Ibtiouen and M. Fadel, "Modeling of the induction machine for the diagnosis of rotor defects. Part. II. Simulation and experimental results," *31st Annual Conference of IEEE Industrial Electronics Society, 2005. IECON 2005.*, Raleigh, NC, USA, 2005, pp. 6 pp.-.

[32] G. Houdouin, G. Barakat, B. Dakyo and E. Destobbeleer, "A winding function theory based global method for the simulation of faulty induction machines," *IEEE International Electric Machines and Drives Conference, 2003. IEMDC'03.*, Madison, WI, USA, 2003, pp. 297-303 vol.1.

[33] J. Milimonfared, H. Meshgin Kelk, A. Der Minassians, S. Nandi and H. A. Toliyat, "A novel approach for broken rotor bar detection in cage induction motors," *Conference Record of 1998 IEEE Industry Applications Conference. Thirty-Third IAS Annual Meeting (Cat. No.98CH36242)*, St. Louis, MO, USA, 1998, pp. 286-290 vol.1.

[34] M. Seera, C. P. Lim, D. Ishak and H. Singh, "Fault Detection and Diagnosis of Induction Motors Using Motor Current Signature Analysis and a Hybrid FMM–CART Model," in *IEEE Transactions on Neural Networks and Learning Systems*, vol. 23, no. 1, pp. 97-108, Jan. 2012.

[35] V. Devanneaux, H. Kabbaj, B. Dagues and J. Faucher, "An accurate model of squirrel cage induction machines under rotor faults," *ICEMS'2001. Proceedings of the Fifth International Conference on Electrical Machines and Systems (IEEE Cat. No.01EX501)*, Shenyang, China, 2001, pp. 384-387 vol.1.

[36] G. Joksimovic and J. Penman, "The detection of interturn short circuits in the stator windings of operating motors," *IECON '98. Proceedings of the 24th Annual Conference of the IEEE*

Industrial Electronics Society (Cat. No.98CH36200), Aachen, Germany, 1998, pp. 1974-1979 vol.4.

[37] R. J. Lee, P. Pillay and R.G. Harley, "D,q reference frames for simulation of induction motors," *Electric Power System Research*, vol. 8. Pp. 15-26, 1984/85.

[38] P. C. Krause, O. Wasynczuk and S. D. Sudhoff, "Theory of Symmetrical Induction Machines," *Analysis of Electric Machinery.* 1986, *564*.

[39] P. C. Krause and C. Thomas, "Simulation of symmetrical induction machinery," *IEEE Transactions on Power Apparatus and Systems,* vol. 84, *(11),* pp. 1038-1053, 1965.

[40] C. A. Hernández-Jacobo, R. Loera-Palomo, F. S. Sellschopp-Sánchez and C. Álvarez-Macías, "Stability Analysis of a PI Controller for a Three-Phase Two-Level Inverter," *2021 IEEE International Autumn Meeting on Power, Electronics and Computing (ROPEC)*, 2021, pp. 1-6.

[41] Y. Liu, M. A. Masadeh and P. Pillay, "Power-Hardware-In-The-Loop-Based Emulation of a Self-Excited Induction Generator Under Unbalanced Conditions," in *IEEE Transactions on Industry Applications*, vol. 58, no. 1, pp. 588-598, Jan.-Feb. 2022.

[42] K. Idjdarene, D. Rekioua, T. Rekioua and A. Tounzi, "Performance of an Isolated Induction Generator Under Unbalanced Loads," in *IEEE Transactions on Energy Conversion*, vol. 25, no. 2, pp. 303-311, June 2010.

[43] IEEE Standard Test Procedure for Polyphase Induction Motors and Generators," in *IEEE Std 112-2017 (Revision of IEEE Std 112-2004)* , vol., no., pp.1-115, 14 Feb. 2018.

[44] B. Palle, M. G. Simoes and F. A. Farret, "Dynamic simulation and analysis of parallel self-excited induction generators for islanded wind farm systems," in *IEEE Transactions on Industry Applications*, vol. 41, no. 4, pp. 1099-1106, July-Aug. 2005

[45] Y. Wang and N. Bianchi, "Investigation of Self-Excited Synchronous Reluctance Generators," in *IEEE Transactions on Industry Applications*, vol. 54, no. 2, pp. 1360-1369, March-April 2018.

[46] Y. Wang and N. Bianchi, "Modeling and Investigation of Self-Excited Reluctance Generators for Wind Applications," in *IEEE Transactions on Industry Applications*, vol. 55, no. 6, pp. 5809-5817, Nov.-Dec. 2019.

[47] S. S. Maroufian and P. Pillay, "Self-Excitation Criteria of the Synchronous Reluctance Generator in Stand-Alone Mode of Operation," in *IEEE Transactions on Industry Applications*, vol. 54, no. 2, pp. 1245-1253, March-April 2018.

[48] Z. Din, J. Zhang, J. Zhao and Y. Jiang, "Doubly Fed Induction Generator with Cascade Converter for Improving Dynamic Performances," *2018 IEEE Energy Conversion Congress and Exposition (ECCE)*, Portland, OR, 2018, pp. 2568-2575.

[49] F. Bizzarri, A. Brambilla and F. Milano, "Simplified Model to Study the Induction Generator Effect of the Subsynchronous Resonance Phenomenon," in *IEEE Transactions on Energy Conversion*, vol. 33, no. 2, pp. 889-892, June 2018.

[50] F. Bizzarri, A. Brambilla and F. Milano, "Simplified Model to Study the Induction Generator Effect of the Subsynchronous Resonance Phenomenon," in *IEEE Transactions on Energy Conversion*, vol. 33, no. 2, pp. 889-892, June 2018.

[51] Y. Zhang, J. Jiao, D. Xu, D. Jiang, Z. Wang and C. Tong, "Model Predictive Direct Power Control of Doubly Fed Induction Generators Under Balanced and Unbalanced Network Conditions," in *IEEE Transactions on Industry Applications*, vol. 56, no. 1, pp. 771-786, Jan.-Feb. 2020.

[52] X. Wang, D. Sun and Z. Q. Zhu, "Resonant-Based Backstepping Direct Power Control Strategy for DFIG Under Both Balanced and Unbalanced Grid Conditions," in *IEEE Transactions on Industry Applications*, vol. 53, no. 5, pp. 4821-4830, Sept.-Oct. 2017.

[53] J. Radosavljević, D. Klimenta and M. Jevtić, "Steady-state analysis of parallel-operated self-excited induction generators supplying an unbalanced load," *Journal of Electrical Engineering,* vol. 63, *(4),* pp. 213-223, 2012.

[54] B. Singh, S. S. Murthy and S. Gupta, "A Stand-Alone Generating System Using Self-Excited Induction Generators in the Extraction of Petroleum Products," in *IEEE Transactions on Industry Applications*, vol. 46, no. 1, pp. 94-101, Jan.-feb. 2010.

[55] A. Verma and B. Singh, "Control and Implementation of Renewable Energy Based Smart Charging Station Beneficial for EVs, Home and Grid," *2019 IEEE Energy Conversion Congress and Exposition (ECCE)*, Baltimore, MD, USA, 2019, pp. 5443-5449.

[56] L. G. Scherer, C. B. Tischer and R. F. de Camargo, "Voltage regulation of stand-alone micro-generation SEIG based system under nonlinear and unbalanced load," *2015 IEEE 24th International Symposium on Industrial Electronics (ISIE)*, Buzios, 2015, pp. 428-433.

[57] P. Nakorn, P. Machot, V. Kinnares and C. Manop, "Study of Three-phase Self-excited Induction Generator Operating as Single-phase Induction Generator Supplying Non-linear Load," *2021 18th International Conference on Electrical Engineering/Electronics, Computer, Telecommunications and Information Technology (ECTI-CON)*, Chiang Mai, Thailand, 2021, pp. 806-809.

[58] V. -T. Phan, D. -T. Nguyen, Q. -N. Trinh, C. -L. Nguyen and T. Logenthiran, "Harmonics Rejection in Stand-Alone Doubly-Fed Induction Generators With Nonlinear Loads," in *IEEE Transactions on Energy Conversion*, vol. 31, no. 2, pp. 815-817, June 2016.

[59] M. Pattnaik and D. Kastha, "Adaptive speed observer for a stand-alone doubly fed induction generator feeding nonlinear and unbalanced loads," *2013 IEEE Power & Energy Society General Meeting*, Vancouver, BC, Canada, 2013, pp. 1-1.

[60] O. M. Elbabo Mohammed, W. Xu, Y. Liu and K. Yu, "Control Design of Stand-Alone Brushless Doubly-Fed Induction Generator for Supplying Nonlinear Loads," *2018 21st International Conference on Electrical Machines and Systems (ICEMS)*, Jeju, Korea (South), 2018, pp. 1279-1284.

[61] N. Patin, E. Monmasson and J. -. Louis, "Active filtering applied to a doubly-fed induction generator supplying nonlinear loads on isolated grid," *2005 European Conference on Power Electronics and Applications*, Dresden, Germany, 2005, pp. 10 pp.-P.10.

[62] G. Girish, C. Nagamani and A. Karthikeyan, "A simple and effective control scheme for improved power quality in a stand alone Wound Rotor Induction Generator feeding non-linear and unbalanced loads," *2012 11th International Conference on Environment and Electrical Engineering*, Venice, Italy, 2012, pp. 814-818.

[63] M. Pattnaik and D. Kastha, "Adaptive Speed Observer for a Stand-Alone Doubly Fed Induction Generator Feeding Nonlinear and Unbalanced Loads," in *IEEE Transactions on Energy Conversion*, vol. 27, no. 4, pp. 1018-1026, Dec. 2012.

[64] B. Singh, S. S. Murthy and S. Gupta, "STATCOM-Based Voltage Regulator for Self-Excited Induction Generator Feeding Nonlinear Loads," in *IEEE Transactions on Industrial Electronics*, vol. 53, no. 5, pp. 1437-1452, Oct. 2006.

[65] M. A. Masadeh and P. Pillay, "Induction Machine Parameters Determination and the Impact of Stator/Rotor Leakage Split Ratio on Its Performance," in *IEEE Transactions on Industrial Electronics*, vol. 67, no. 7, pp. 5291-5301, July 2020.

[66] F. E. Fleming and C. S. Edrington, "Real-Time Emulation of Switched Reluctance Machines via Magnetic Equivalent Circuits," in *IEEE Transactions on Industrial Electronics*, vol. 63, no. 6, pp. 3366-3376, June 2016.

[67] Y. Liu, M. A. Masadeh and P. Pillay, "Emulation of an Isolated Induction Generator Under Unbalanced Conditions," *2020 IEEE Energy Conversion Congress and Exposition (ECCE)*, Detroit, MI, USA, 2020, pp. 1794-1799.

[68] F. Duan and R. Zivanovic, "A model for induction motor with stator faults," *2012 22nd Australasian Universities Power Engineering Conference (AUPEC)*, Bali, Indonesia, 2012, pp. 1-5.

[69] R. M. Tallam *et al*., "A survey of methods for detection of stator related faults in induction machines," *4th IEEE International Symposium on Diagnostics for Electric Machines, Power Electronics and Drives, 2003. SDEMPED 2003.*, Atlanta, GA,USA, 2003, pp. 35-46.

[70] A. Siddique, G. S. Yadava and B. Singh, "A review of stator fault monitoring techniques of induction motors," in *IEEE Transactions on Energy Conversion*, vol. 20, no. 1, pp. 106-114, March 2005.

[71] M. Sahraoui *et al*, "Modelling and detection of inter-turn short circuits in stator windings of induction motor," in *IECON 2006-32nd Annual Conference on IEEE Industrial Electronics,* 2006.

[72] A. M. da Silva, R. J. Povinelli and N. A. O. Demerdash, "Induction Machine Broken Bar and Stator Short-Circuit Fault Diagnostics Based on Three-Phase Stator Current Envelopes," in *IEEE Transactions on Industrial Electronics*, vol. 55, no. 3, pp. 1310-1318, March 2008.

[73] O. Imoru, A. M. Bhaskar, A. A. Jimoh and Y. Hamam, "Electrical machine winding faults diagnosis using periodogram," *2017 IEEE AFRICON*, Cape Town, South Africa, 2017, pp. 1397-1401.

[74] A. Sapena-Baño *et al*., "Harmonic Order Tracking Analysis: A Novel Method for Fault Diagnosis in Induction Machines," in *IEEE Transactions on Energy Conversion*, vol. 30, no. 3, pp. 833-841, Sept. 2015.

[75] K. Saad, T. B. Ali and K. Abdellah, "Detection and diagnosis of rotor and stator faults in open end winding induction motor," *2019 1st International Conference on Sustainable Renewable Energy Systems and Applications (ICSRESA)*, Tebessa, Algeria, 2019, pp. 1-5.

[76] Baccarini, L.M.R., de Menezes, B.R. and Caminhas, W.M., 2010. Fault induction dynamic model, suitable for computer simulation: Simulation results and experimental validation. *Mechanical Systems and Signal Processing*, *24*(1), pp.300-311.

[77] G. M. Joksimovic and J. Penman, "The detection of inter-turn short circuits in the stator windings of operating motors," in *IEEE Transactions on Industrial Electronics*, vol. 47, no. 5, pp. 1078-1084, Oct. 2000.

[78] D. C. Patel and M. C. Chandorkar, "Transient modeling and analysis of induction motors with position effects in stator turn faults," *2010 IEEE International Conference on Industrial Technology*, Vina del Mar, 2010, pp. 1251-1256.

[79] R. M. Tallam, T. G. Habetler and R. G. Harley, "Transient model for induction machines with stator winding turn faults," in *IEEE Transactions on Industry Applications*, vol. 38, no. 3, pp. 632-637, May-June 2002.

[80] Baccarini, L.M.R., de Menezes, B.R. and Caminhas, W.M. "Fault induction dynamic model, suitable for computer simulation: Simulation results and experimental validation." *Mechanical Systems and Signal Processing* 24, no. 1 (2010): 300-311.

[81] J. S. S. Prasad, T. Bhavsar, R. Ghosh, and G. Narayanan, "Vector control of three-phase ac/dc front-end converter," *Sadhana*, vol. 33, no. 5, pp. 591-613, 2008.

[82] A. Varais, X. Roboam, F. Lacressonnière, E. Bru and N. Roux, "Reduced Scale PHIL Emulation Concepts Applied to Power Conversion Systems With Battery Storage," in *IEEE Transactions on Industrial Electronics*, vol. 68, no. 5, pp. 3973-3981, May 2021.

[83] A. P. Yadav, R. Madani, N. Amiri, J. Jatskevich and A. Davoudi, "Induction Machine Parameterization From Limited Transient Data Using Convex Optimization," in *IEEE Transactions on Industrial Electronics*, vol. 69, no. 2, pp. 1254-1265, Feb. 2022.

[84] P. M. Santos *et al*., "A simplified induction machine model to study rotor broken bar effects and for detection," *2006 37th IEEE Power Electronics Specialists Conference*, Jeju, 2006, pp. 1-7.

[85] P. Alemi and J. Nazarzadeh, "Asymmetric Modeling of Induction Machines Using Bars and Rings Current in Interior Fault," *2007 IEEE International Electric Machines & Drives Conference*, Antalya, 2007, pp. 841-846.

[86] R. Fiser and Ferkolj, "Study of operational behaviour of induction motor with rotor asymmetry," *MELECON '98. 9th Mediterranean Electrotechnical Conference. Proceedings (Cat. No.98CH36056)*, Tel-Aviv, Israel, 1998, pp. 1185-1188 vol.2.

[87] M. Nemec, D. Makuc, V. Ambrožič and R. Fišer, "Simplified model of induction machine with electrical rotor asymmetry," *The XIX International Conference on Electrical Machines - ICEM 2010*, Rome, 2010, pp. 1-6.

[88] C. C. M. Cunha, R. O. C. Lyra and B. C. Filho, "Simulation and analysis of induction machines with rotor asymmetries," in *IEEE Transactions on Industry Applications*, vol. 41, no. 1, pp. 18-24, Jan.-Feb. 2005.

[89] M. Nemec *et al*, "Parameters estimation using single phase measurement of three phase induction machine," *Przegląd Elektrotechniczny (Electrical Review), (3),* pp. 129-132, 2011.

[90] D. Makuc *et al*, "Parameters estimation of induction motor with faulty rotor," *Przeglad Elektrotechniczny,* vol. 88, *(1a),* pp. 41-46, 2012.

[91] K. Drobnič, M. Nemec, D. Makuc, R. Fišer and V. Ambrožič, "Pseudo-salient model of induction machine with broken rotor bars," *8th IEEE Symposium on Diagnostics for Electrical Machines, Power Electronics & Drives*, Bologna, Italy, 2011, pp. 213-220.

[92] H. Douglas, P. Pillay and A. K. Ziarani, "Broken rotor bar detection in induction machines with transient operating speeds," in *IEEE Transactions on Energy Conversion*, vol. 20, no. 1, pp. 135-141, March 2005.

Appendix - A

Measurement Results of Induction Machine with Broken Rotor Bars

1. Data acquired at 16.01Hz

Rotor angle (°)	Line current (A_{rms})	Line voltage (V_{rms})	Real Power (W)
0	1.79	17.86	27.84
10	1.79	18.03	28.27
20	1.79	18.46	28.46
30	1.79	18.7	29.07
40	1.79	18.81	29.31
50	1.79	18.82	29.3
60	1.79	18.85	29.27
70	1.8	18.9	29.54
80	1.804	18.77	29.38
90	1.805	18.52	29.22
100	1.803	17.68	27.55
110	1.79	17.59	27.35
120	1.79	17.59	27.34
130	1.802	17.64	27.61
140	1.8	17.55	27.43
150	1.801	17.54	27.47
160	1.801	17.63	27.67
170	1.8	17.65	27.61
180	1.79	18	28.08
190	1.799	18.06	28.27
200	1.796	18.17	28.45
210	1.799	18.39	28.75
220	1.796	18.63	28.98
230	1.8	18.72	29.18
240	1.802	18.82	29.34
250	1.801	18.81	29.36
260	1.802	18.81	29.38
270	1.798	18.72	29.23
280	1.798	18.36	28.86
290	1.8	18.24	28.71
300	1.798	18.14	28.5
310	1.8	18.14	28.56
320	1.798	18.03	28.41
330	1.8	18.01	28.41
340	1.798	18.03	28.37
350	1.798	18.13	28.57
360	1.799	18.24	28.68

2. Data acquired at 50Hz

Rotor angle (°)	Line current (A_{rms})	Line voltage (V_{rms})	Real Power (W)
0	1.78	29.79	29.65
10	1.8	30.13	30.46
20	1.79	30.22	30.67
30	1.8	30.84	31.35
40	1.801	31.49	32.04
50	1.79	31.78	32.56
60	1.79	31.99	32.82
70	1.8	31.95	32.9
80	1.803	31.7	32.9
90	1.801	31.07	32.23
100	1.803	30.63	31.77
110	1.801	30.24	31.31
120	1.79	30.16	31
130	1.802	30.03	30.93
140	1.79	29.69	30.22
150	1.79	29.56	30.1
160	1.801	29.66	30.29
170	1.799	29.89	30.43
180	1.8	30.3	30.9
190	1.799	30.41	31.11
200	1.803	30.58	31.58
210	1.799	31.14	32.18
220	1.802	31.52	32.66
230	1.799	32.03	33.32
240	1.799	32.26	33.44
250	1.801	32.23	33.57
260	1.799	31.91	33.28
270	1.801	31.49	32.93
280	1.798	30.87	32.18
290	1.803	30.42	31.78
300	1.798	30.28	31.4
310	1.8	30.15	31.3
320	1.796	29.85	30.89
330	1.801	29.83	30.87
340	1.802	29.83	30.81
350	1.797	29.98	30.83
360	1.803	30.38	31.35

3. Data acquired at 75Hz

Rotor angle (°)	Line current (A_{rms})	Line voltage (V_{rms})	Real Power (W)
0	1.797	40.29	31.14
10	1.802	40.67	31.89
20	1.801	40.83	32.46
30	1.801	41.48	33.27
40	1.798	42.4	34.45
50	1.798	42.79	35.2
60	1.804	43.35	36.07
70	1.799	43.14	35.97
80	1.802	42.59	35.64
90	1.8	41.89	34.85
100	1.799	41.17	33.96
110	1.803	40.75	33.47
120	1.801	40.69	33.16
130	1.8	40.59	33.13
140	1.804	40.28	32.69
150	1.799	40.09	32.26
160	1.803	40.2	32.31
170	1.799	40.53	32.52
180	1.802	41.03	33.15
190	1.798	40.98	32.79
200	1.8	41.25	33.39
210	1.8	41.94	34.29
220	1.799	42.55	35.11
230	1.802	43.08	36.27
240	1.803	43.51	36.71
250	1.801	43.49	36.87
260	1.801	42.88	36.21
270	1.802	42.25	35.5
280	1.798	41.44	34.54
290	1.8	40.84	33.74
300	1.802	40.84	33.68
310	1.8	40.55	33.24
320	1.8	40.28	32.83
330	1.799	40.19	32.67
340	1.802	40.28	32.71
350	1.8	40.5	32.82
360	1.799	40.92	33.23

4. Data acquired at 85Hz

Rotor angle (°)	Line current (A_{rms})	Line voltage (V_{rms})	Real Power (W)
0	1.8	44.92	32.5
10	1.803	45.19	33.13
20	1.801	45.26	33.6
30	1.802	46.25	34.94
40	1.8	46.91	35.6
50	1.803	47.48	36.76
60	1.802	47.97	37.54
70	1.803	47.64	37.46
80	1.803	47.22	37.13
90	1.801	46.32	36.01
100	1.803	45.52	34.89
110	1.801	45.04	34.17
120	1.801	45.04	34.12
130	1.803	44.83	33.81
140	1.802	45.54	33.33
150	1.8	44.37	32.98
160	1.802	44.48	33.05
170	1.8	44.9	33.35
180	1.799	45.4	33.98
190	1.8	45.59	34.32
200	1.799	45.99	35.05
210	1.799	46.66	36.07
220	1.799	47.26	36.86
230	1.8	47.74	37.82
240	1.802	48.25	38.45
250	1.798	48.13	38.48
260	1.799	47.52	37.79
270	1.803	47	36.22
280	1.801	45.9	35.86
290	1.8	45.3	35.05
300	1.8	45.22	34.79
310	1.798	44.93	34.34
320	1.8	44.63	33.84
330	1.8	44.55	33.65
340	1.801	44.57	33.42
350	1.799	44.89	33.65
360	1.802	45.39	34.28

5. Data acquired at 100Hz

Rotor angle (°)	Line current (A_{rms})	Line voltage (V_{rms})	Real Power (W)
0	1.803	52.03	35.55
10	1.801	52.22	35.85
20	1.802	52.31	36.4
30	1.8	53.14	37.31
40	1.803	54.11	38.82
50	1.803	54.77	40.07
60	1.799	54.94	39.87
70	1.798	54.72	40.12
80	1.802	54.08	39.55
90	1.804	53.22	38.64
100	1.801	52.57	37.82
110	1.801	51.89	36.71
120	1.801	51.87	36.61
130	1.799	51.7	36.23
140	1.802	51.41	35.73
150	1.799	51.14	35.22
160	1.798	51.25	35.11
170	1.803	51.74	35.63
180	1.8	52.35	36.36
190	1.8	52.54	36.79
200	1.802	52.73	37.34
210	1.802	53.7	38.71
220	1.8	54.4	39.64
230	1.8	54.86	40.63
240	1.803	55.47	41.55
250	1.799	55.24	41.42
260	1.802	54.65	40.63
270	1.803	53.92	39.82
280	1.803	52.91	38.55
290	1.803	52.14	37.46
300	1.8	52.08	37.19
310	1.799	51.68	36.51
320	1.803	51.49	36.26
330	1.802	51.39	36.06
340	1.803	51.52	36.04
350	1.803	51.83	36.27
360	1.804	52.44	36.94

6. Data acquired at 125Hz

Rotor angle (°)	Line current (A_{rms})	Line voltage (V_{rms})	Real Power (W)
0	1.8	64.4	37.3
10	1.801	64.2	37.1
20	1.8	63.9	36.8
30	1.798	63.8	36.6
40	1.803	64.3	36.5
50	1.803	64.7	36.6
60	1.8	65.3	37.8
70	1.801	65.4	38.4
80	1.802	65.6	39.2
90	1.8	66.4	40.1
100	1.8	67.3	41.5
110	1.801	68	43.7
120	1.802	68.7	44.5
130	1.8	68.5	44.7
140	1.802	68.3	44.5
150	1.801	67.5	43.4
160	1.799	65.8	41.2
170	1.801	64.8	39.1
180	1.8	64.9	39
190	1.802	64.5	37.9
200	1.802	64.2	37.4
210	1.802	64.2	37.2
220	1.8	64.4	37.1
230	1.801	64.9	37.8
240	1.803	65.4	38.5
250	1.802	65.7	39.2
260	1.804	65.7	39.3
270	1.802	66.4	40.2
280	1.8	67.5	42
290	1.802	68.1	43.7
300	1.8	68.5	44.3
310	1.802	68.3	44.4
320	1.803	67.5	43.4
330	1.8	66.7	42.3
340	1.799	65.7	40.9
350	1.801	64.9	39.5
360	1.802	64.9	39.3

7. Data acquired at 150Hz

Rotor angle (°)	Line current (A_{rms})	Line voltage (V_{rms})	Real Power (W)
0	1.799	76.3	41.9
10	1.798	76.1	41.5
20	1.802	75.8	41
30	1.801	75.8	40.6
40	1.801	76.1	40.5
50	1.804	77	41.5
60	1.804	77.4	42.2
70	1.8	77.5	42.7
80	1.8	77.4	42.8
90	1.801	78.5	44.4
100	1.801	79.6	46.5
110	1.802	80.4	48.5
120	1.803	80.7	49.9
130	1.802	80.7	50
140	1.801	80.4	49.3
150	1.803	79.2	47.7
160	1.801	77.5	45.1
170	1.802	76.7	43.3
180	1.803	76.7	43
190	1.801	76.1	41.8
200	1.8	76	41.2
210	1.801	76	41
220	1.8	76.2	40.9
230	1.802	76.7	41.4
240	1.801	77.4	42.4
250	1.801	77.7	43
260	1.802	77.6	43.3
270	1.799	78.7	44.9
280	1.802	79.6	46.5
290	1.803	80.3	48.1
300	1.8	80.6	49.3
310	1.801	80.4	49.3
320	1.802	79.6	48.1
330	1.801	78.6	46.5
340	1.801	77.5	44.9
350	1.801	76.7	43.4
360	1.803	76.8	43.2